Semileptonic and radiative meson decays from lattice QCD with improved staggered fermions

Gordon Donald

Thesis submitted to the University of Glasgow
for the degree of Doctor of Philosophy

School of Physics and Astronomy
College of Science and Engineering
University of Glasgow

March 2013

Abstract

Improved staggered fermions are a numerically efficient formulation of the fermion action in lattice QCD. They are used for nonperturbative theoretical calculations of the QCD form factors appearing in the decay rates for radiative and semileptonic meson transitions. The constituent quarks are bound inside hadrons by the strong interaction, so the decay rate depends on the interactions between the quarks, which are described by QCD. The fermion action used in these calculations is the Highly Improved Staggered Quark (HISQ) action.

The HISQ Dirac operator, $\not{D}_{HISQ}$, contains four tastes of quark equivalent to one continuum quark, which is a consequence of the discretisation. In gauge configurations including staggered sea quarks, the extra tastes are accounted for by taking the fourth root of the fermion determinant. The validity of this step relies on the taste structure of $\not{D}_{HISQ}$. To look into this, the interactions of the eigenvectors of $\not{D}_{HISQ}$ with the topology of the gauge field is studied. The results show that the eigenvectors corresponding to the different tastes decouple in the continuum limit in such a way that $\not{D}_{HISQ}$ resembles the continuum Dirac operator.

Using the HISQ action for the charm quark, the form factor $V(q^2)$ appearing in the radiative decay rate for $J/\psi \to \eta_c\gamma$ is calculated. The form factor on the lattice is calculated by computing 3-point correlation functions, which are fitted simultaneously with 2-point correlation functions to obtain the meson transition matrix element. Only the form factor at $q^2 = 0$ enters the decay rate for a physical photon, so the kinematics of the decay are tuned to calculate $V(0)$. The lattice operator used for the electromagnetic vector current is nonperturbatively normalised.

Lattice QCD can also be used to calculate matrix elements for the decays of mesons to 2 photons. The form factor for the radiative decay $\eta_c \to 2\gamma$ is calculated at the physical kinematics using nonperturbatively normalised lattice operators for the currents. The form factor is the same when calculated on gauge configurations containing $N_f = 2 + 1$ flavours of asqtad sea quarks and $N_f = 2 + 1 + 1$ flavours of HISQ sea quarks.

Lattice 3-point correlators are used to calculate the form factors for the semileptonic decay $D_s \to \phi\ell\nu$. This interaction is mediated by a weak W boson, so contains vector and axial vector form factors. Each of these is calculated on the lattice with a nonperturbatively normalised current. The decay includes a $c \to s$ quark decay, so the experimentally measured decay rate depends on the CKM matrix element V_{cs}. By comparing the theoretical calculation of the decay rate to the measurements, a value of $V_{cs} = 0.975(48)$ is obtained.

Acknowledgements

I would like to acknowledge the help and advice of my supervisor Christine Davies throughout my research and whilst writing my thesis. I also would like to thank my collaborators for their assistance, particularly Eduardo Follana and Jonna Koponen. I would also like to thank Jonna for sharing an office with me and never pouring juice on the floor.

I would like to thank all the staff and students in the Glasgow PPT group for making it such an enjoyable place to work. In particular, I would like to thank my fellow students who I spent the most time with, Dan Coumbe, António Morais, Brian Colquhoun and Kate Elliott, for their humour and for wearing silly hats.

I thank my family for their support and my brother Andrew for attempting to explain topology to me.

My studentship was funded by STFC and I used gauge configurations generated by the MILC Collaboration. Computing was done on the Darwin supercomputer at the University of Cambridge.

Declaration

With the exception of chapters 1,2 and 4, which contain introductory material, all the work described in this thesis was carried out by the author unless otherwise stated.

Contents

List of Tables

List of Figures

Chapter 1

Introduction

1.1 The Standard Model

The aim of particle physics is to understand the fundamental constituents of the universe and how they interact with one another. The Standard Model describes our present understanding of fundamental forces and particles [1, 2, 3, 4]. It contains three generations of spin-1/2 fermions, which can interact through the strong, weak and electromagnetic forces by the exchange of spin-1 bosons. In each generation of fermions, there are two quarks with different electric charges and two leptons, one of which is uncharged. The particles of the Standard Model are tabulated in Table 1.1, with their charge, spin and approximate mass [5]. The charges are in units of the (positive) electron charge. The successive generations of fermions have the same charge, but increasing mass.

The gauge bosons mediate the forces of the Standard Model; the photon, γ, mediates the electromagnetic interaction, the gluon, g, mediates the strong force and the weak Z and $W^{\pm}$ bosons mediate the weak force. Each charged particle in the Standard Model has a corresponding antiparticle with opposite electric charge. The uncharged

Particle	Charge	Spin	Masses (GeV)
u,c,t	+2/3e	1/2	$m_u \simeq 0.005$, $m_c \simeq 1.5$, $m_t \simeq 170$
d,s,b	-1/3e	1/2	$m_d \simeq 0.01$, $m_s \simeq 0.2$, $m_b \simeq 4.7$
e^-,μ^-,τ^-	-1e	1/2	$m_e \simeq 0.0005$, $m_\mu \simeq 0.1$, $m_\tau \simeq 1.7$
ν_e,ν_μ,ν_τ	0	1/2	$m_\nu < 0.01$
γ	0	1	0
g	0	1	0
Z	0	1	90
W^+	+1e	1	80

Table 1.1: Particles of the Standard Model. The fermions are in the top half and the bosons in the bottom half. The charges are in units of the electron charge and antiparticles have opposite charge.

γ, g and Z bosons are their own antiparticle.

Fermions' coupling to the photon is proportional to their electric charge. All the quarks, as well as the charged leptons, feel this force. As the coupling is small, the interaction can be expanded perturbatively in powers of e.

Flavour-changing interactions amongst quarks are mediated by the weak force. In a weak quark decay, a quark of one flavour emits a $W^{\pm}$ boson and decays to a quark of a different flavour. The decay conserves electric charge so weak decays are from an up-type to a down-type quark or vice versa.

Decay rates for processes in which there is a charged flavour-changing current depend on the CKM matrix [6, 7], which describes the strength of the weak interaction between the quark flavours. It is written as

$$V_{CKM} = \begin{pmatrix} V_{ud} & V_{us} & V_{ub} \\ V_{cd} & V_{cs} & V_{cb} \\ V_{td} & V_{ts} & V_{tb} \end{pmatrix}. \tag{1.1}$$

In the Standard Model, the CKM matrix is unitary. The CKM elements can be determined experimentally by measuring flavour changing processes and comparing the measurements to the expectations from the Standard Model. Deviations from unitarity would be an indication of physics beyond the Standard Model. To detect non-unitarity of the CKM matrix requires precise flavour physics measurements and accurate theoretical calculations of the Standard Model predictions.

Unlike leptons, quarks interact with the strong force, which hinders measurements of flavour-changing interactions by binding quarks inside hadrons. Quarks carry an $SU(3)$ 'colour' charge, but experiments only ever detect colourless bound states. At low energies, the coupling of the strong force is large and it cannot be accurately determined perturbatively. Mesons are hadrons containing one quark and one antiquark, whilst hadrons containing three quarks are called baryons. The constituent quarks which are contained inside hadrons are called the valence quarks.

Table 1.1 shows a list a mesonic bound states of quarks with their usual assigned quark content, spin and approximate mass [5]. This list is certainly not complete and predominantly features mesons that are mentioned again in this thesis (which is not a coincidence). No distinction is made between the lightest u and d quarks; both are labelled as light quarks l because the difference in the u and d masses is not significant in lattice calculations. The neutral π^0 meson has flavour nonsinglet $u\bar{u} - d\bar{d}$ quark content and the η' meson is the flavour-singlet meson containing u, d and s quarks.

Relating the properties of the constituent quarks to observed hadrons requires a theoretical understanding of the strong force.

Particle	Quark Content	Spin	Mass (MeV)
π	$l\bar{l}$	0	135
K	$l\bar{s}$	0	497
η	$l\bar{l} - s\bar{s}$	0	547
η'	$l\bar{l} + s\bar{s}$	0	957
ϕ	$s\bar{s}$	1	1020
D_s	$c\bar{s}$	0	1968
η_c	$c\bar{c}$	0	2980
J/ψ	$c\bar{c}$	1	3096

Table 1.2: Examples of bound meson states, tabulated with their valence quark content, spin and (approximate) mass [5]. The up and down quarks are taken to have degenerate mass in lattice QCD and are both labelled as light, l. Both the π and η are flavour-nonsinglet mesons containing up, down and strange valence quarks. The η' is the light unflavoured flavour-singlet meson. The unflavoured ϕ is predominantly $s\bar{s}$.

1.1.1 QCD

The strong force is described by quantum-chromodynamics (QCD) [8, 9]. The QCD Lagrangian is [10, 11, 12]

$$\mathcal{L}_{QCD} = \sum_f \bar{\psi}_f (iD_\mu \gamma_\mu + m_f)\psi_f - \frac{1}{4} F^a_{\mu\nu} F^{\mu\nu a}, \tag{1.2}$$

in which the sum f is over quark flavour, ψ is the quark field and $F^a_{\mu\nu}$ the gluon field strength tensor. The γ_μ are anticommuting Dirac γ matrices. The gluon field strength is

$$F^a_{\mu\nu} = \partial_\mu A^a_\nu - \partial_\nu A^a_\mu - g f^{abc} A^b_\mu A^c_\nu \tag{1.3}$$

where f^{abc} are the structure constants of SU(3) and A_μ the gluon field. The covariant derivative contains the quark-gluon interaction

$$D_\mu = \partial_\mu + igA^a_\mu \frac{\lambda_a}{2}, \tag{1.4}$$

where g is the QCD coupling constant and λ_a is a Gell-mann matrix. The gluon self-interaction term and the quark-gluon coupling are both proportional to g. The vacuum state of QCD contains no valence quarks, but consists of a strongly-interacting gluonic background. Due to the strong coupling, it also contains virtual quark loops. These are the sea quarks which also appear as virtual loops in hadronic states.

1.2 Path integral approach to quantum field theory

The path integral approach to quantum field theories considers all possible configurations of the fields in the action [13]. A configuration of fields is a set of possible values for each field to have at every point where the field is defined. In continuum QCD, the

quark, antiquark and gluon fields, ψ, $\bar{\psi}$ and A, take on values at all points in spacetime.

The transition probability from an initial state, $|i\rangle$, to a final state, $|f\rangle$, is related to the matrix element $\langle i|\mathcal{S}|f\rangle$ and is given by a quantum superposition of all possible paths between the two states. The contribution of each path is weighted by the action, S, of the theory.

The action for a quantum field theory is given by the integral of the Lagrangian:

$$\mathcal{S}_{QCD} = \int d^3x dt \mathcal{L}_{QCD}. \tag{1.5}$$

The path integral approach gives the matrix element $\langle i|\mathbf{S}|f\rangle$ as

$$\frac{\int [d\psi][d\bar{\psi}][dA_\mu]\langle i|\mathbf{S}|f\rangle e^{iS_{QCD}}}{\int [d\psi][d\bar{\psi}][dA_\mu] e^{iS_{QCD}}}, \tag{1.6}$$

where the denominator is for normalisation and $\mathbf{S}$ is the S-matrix. The integral over all paths contains $[d\psi]$ in the measure and this means $\prod_y d\psi(y)$, which is an integration over the field ψ at all points in spacetime.

1.2.1 Euclidean space

The contribution of each path to the action is simpler in Euclidean space. It is also numerically convenient because the oscillating complex exponential in the path integral is replaced by a decaying exponential.

The transformation to Euclidean space is made by a Wick rotation in the time direction $t \to it$. This changes the time integration, so that $\mathcal{S}_{QCD} \to i\mathcal{S}_{QCD}$ and hence changes the appearance of the action in the path integral, $e^{iS_{QCD}} \to e^{-S_{QCD}}$.

1.3 Lattice discretisation of QCD

The path integral formulation requires an infinite number of integrations over the infinite number of points in continuous spacetime. To reduce this so that it can be simulated numerically, the theory is discretised onto a 4-dimensional cubic lattice [14]. On the lattice, the quark fields are only defined on a finite number of lattice sites, separated by a discrete lattice spacing, a. Simulations are performed in a finite spacetime volume, typically with periodic boundary conditions.

There are a finite number of lattice sites, i, which can be identified by the coordinates of the site, (i_x, i_y, i_x, i_t). Gluon fields are represented by gauge links connecting a lattice site to its neighbours, as shown in Figure 1.1. A gauge link connecting a site i to its neighbour in the forward μ direction, $i + \mu$ is written as

$$U_\mu(i) = e^{igA_\mu(i)}, \tag{1.7}$$

where $A_\mu(i)$ is the gluon field. The gauge links are unitary, so the reverse link from

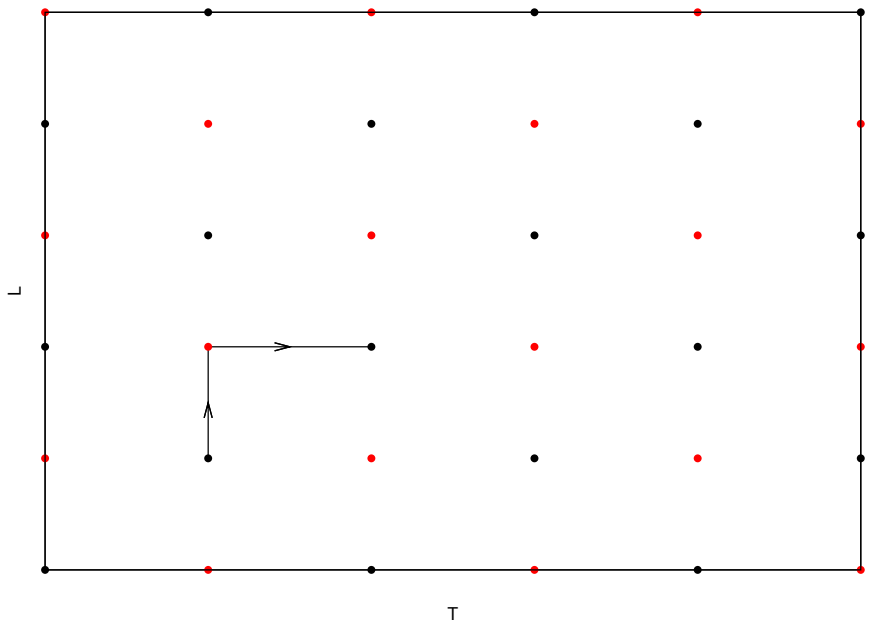

Figure 1.1: A diagram showing spacetime discretised onto a lattice. The quark fields are defined on the red and black lattice sites and gauge links (shown with arrows) join each site to its neighbours. In the naive one-link and staggered actions, the gauge fields join sites separated by an odd number of links, so connect the red sites to black ones.

$i + \mu$ to i is $U^{\dagger}_{\mu}(i)$.

Rather than integrating the path integral over the (still prohibitively large) number of sites and links, it is calculated using a representative sample of gauge configurations. An ensemble of lattice configurations is generated where the probability of any possible configuration being present in the ensemble is proportional to $e^{-S_{QCD}}$. In this way, the quantities can be calculated on the ensemble simply by averaging over the result obtained for each individual configuration. A gauge ensemble satisfying these properties is generated with an updating algorithm that performs accept/reject steps based on the variation of the action. Modern algorithms include the effects of sea quarks [15, 16, 17].

Hadronic quantities can be calculated by averaging correlation functions over the ensemble of gauge configurations. A meson with quantum numbers J^{PC} can be created with a Dirac bilinear with the same J^{PC} and allowed to propagate, resulting in a 2-point correlator. For a meson with J^{PC} given by Γ which is created at lattice site i and destroyed at site j, the correlation function is

$$\langle \bar{\psi}(i)\Gamma\psi(i)\ \bar{\psi}(j)\Gamma\psi(j)\rangle. \tag{1.8}$$

The correlation function is calculated on the lattice by computing quark propagators between the sites i and j, $G(i,j)$,

$$\mathrm{Tr}\left[\Gamma G(i,j)\Gamma G(j,i)\right], \tag{1.9}$$

where the trace is over the quark colour and spin indices. The quark propagator $G(i,j)$ is found by inverting the Dirac operator $\not{D} + m_q$, where $\not{D}$ is the discretised version of the Dirac operator and m_q the quark mass. Properties of the meson on the lattice can be extracted from the correlator data by fitting to the known form. For a 2-point correlator, the form is [18]

$$\sum_A a_A e^{-m_A t} \tag{1.10}$$

where the sum is over QCD states A with the correct quantum numbers and t is the time separation between the sites i and j. As it is the time separation that is important in the 2-point correlator, there is often a sum over all the lattice sites on the same timeslice – that is all the sites i with the same time coordinate i_t. In practice, the fit form is more complicated than Equation 1.10 because periodic boundary conditions are imposed on the lattice and oscillating contributions appear for fermions simulated with staggered actions. The details of both of these are discussed in Chapter 4.

1.3.1 Lattice gauge action

In lattice QCD, the gluon fields are contained in the gauge links that connect lattice sites together as $U_\mu(i) = e^{igA_\mu(i)}$ [19]. The lattice gluon action is composed of closed loops of gauge links. The simplest Wilson action is

$$\mathcal{S} = \beta \sum_p \left(1 - \mathrm{Re}(\mathrm{Tr} U_p)\right), \tag{1.11}$$

where the sum is over 1×1 loops of gauge links called plaquettes and $\beta = 6/g^2$.

The continuum limit of Equation 1.11 is the continuum gluon action. At finite lattice spacing, there are discretisation errors which vanish as $a \to 0$,

$$\mathcal{S}_{lattice} = \mathcal{S}_{continuum} + \mathcal{O}(a^2) + ..., \tag{1.12}$$

and any lattice action with the correct continuum limit can be used in a simulation. For the Wilson gluon action, the leading discretisation errors are $\mathcal{O}(a^2)$.

Adding extra terms that vanish in the continuum limit can improve the Wilson gluon action [20]. More complicated loops than 1×1 plaquettes such as 2×1 loops of gauge links can be used to cancel the $\mathcal{O}(a^2)$ errors in the gluon action by including them in the action with the right coefficients.

1.3.2 Lattice fermions

The naive discretised quark action is

$$\mathcal{S}_q = \sum_i \bar{\psi}(i)(\gamma_\mu \Delta_\mu + m)\psi(i), \tag{1.13}$$

where Δ_μ is a finite difference replacement for the derivative. For the present purpose, it is sufficient to consider the simplest, one-link finite difference operator for the derivative:

$$\Delta_\mu \psi(i) = \frac{1}{2}\left(U_\mu(i)\psi(i+\hat{\mu}) - U_\mu^\dagger(i-\hat{\mu})\psi(i-\hat{\mu})\right). \tag{1.14}$$

The representation of the Dirac γ matrices used is

$$\gamma_t = \begin{pmatrix} 1 & 0 \\ 0 & -1 \end{pmatrix}, \ \vec{\gamma} = \begin{pmatrix} 0 & \vec{\sigma} \\ \vec{\sigma} & 0 \end{pmatrix}, \tag{1.15}$$

where $\vec{\sigma}$ are the Pauli matrices. The γ matrices are traceless and have the useful properties

$$\gamma_\mu^\dagger = \gamma_\mu, \ \gamma_\mu^2 = 1 \text{ and } \{\gamma_\mu, \gamma_\nu\} = 2\delta_{\mu\nu}. \tag{1.16}$$

γ_5 is defined as $\gamma_5 = \gamma_x\gamma_y\gamma_z\gamma_t$ and $\gamma_5^2 = 1$.

The lattice fermion action suffers from what is known as the doubling problem, which means it describes 16 low-energy fermions instead of just one. This can be seen by looking at the fermion propagator in momentum space. The fermion fields in momentum space, $\Psi(p)$, are related to those in position space, $\psi(x)$, by a Fourier transform

$$\Psi(p) = \int d^4x e^{-ipx}\psi(x) \text{ and } \psi(x) = \frac{1}{(2\pi)^4}\int d^4p e^{ipx}\Psi(p). \tag{1.17}$$

On the lattice, the integral over spacetime can be replaced with a sum over the sites and the momentum integral is restricted to the values of p that can be simulated on the lattice. Due to the finite lattice spacing, the lattice momentum must be between $p = \pm\frac{\pi}{a}$.

The continuum fermion action in momentum space is

$$\frac{1}{(2\pi)^4}\int dp\bar{\Psi}(p)(i\gamma^\mu p_\mu + m)\Psi(p). \tag{1.18}$$

The propagator in momentum space is the inverse of $(i\gamma^\mu p_\mu + m)$.

The lattice action in momentum space differs from the continuum because the derivative operator has been replaced by a finite difference. It is

$$\frac{1}{(2\pi)^4}\int_{-\frac{\pi}{a}}^{\frac{\pi}{a}} dp\bar{\Psi}(p)(i\gamma^\mu \frac{\sin p_\mu a}{a} + m)\Psi(p). \tag{1.19}$$

Now the inverse propagator is $(i\gamma^\mu \frac{\sin p_\mu a}{a} + m)$ and displays continuum like behaviour for $\sin p_\mu a \simeq 0$, which happens at $p_\mu \simeq 0$ and $p_\mu \simeq \frac{\pi}{a}$. It follows that fermions with momenta close to the maximum allowed momentum on the lattice behave like low-energy ($p_\mu \simeq 0$) fermions. There are 15 of the doublers as they can have $p_\mu \simeq \frac{\pi}{a}$ in any of the 4 directions.

There are several different methods for implementing fermions on the lattice which try to avoid the doubling problem.

Wilson fermions

The Wilson fermion formulation deals with the doublers by adding a two-link term to the fermion action to give them a mass in the continuum limit [19]:

$$\bar{\psi}(i)\frac{ra}{2}\Delta_\mu^2\psi(i), \tag{1.20}$$

where Δ_μ^2 is defined as

$$\Delta_\mu^2\psi(i) = U_\mu^\dagger(i-\hat{\mu})\psi(i-\hat{\mu}) - 2\psi(i) + U_\mu(i)\psi(i+\hat{\mu}). \tag{1.21}$$

The inverse propagator in this case is

$$\left(i\gamma^\mu\frac{\sin p_\mu a}{a} + m + \frac{r}{a}2(\cos p_\mu a - 1)\right). \tag{1.22}$$

For the doublers with $p_\mu \not\approx 0$, this new term does not vanish and so prevents the inverse propagator from behaving as in the continuum.

Twisted mass fermions

The naive action, Equation 1.13, has a chiral symmetry as it is invariant under

$$\psi \to e^{i\alpha\gamma_5}\psi. \tag{1.23}$$

The extra term added in the Wilson action to remove the doublers breaks this symmetry. There is nothing to stop the kinetic part of the Wilson Dirac operator, $\not{D}_W$, having an eigenvalue close to $-m$ on some gauge configurations. On these 'exceptional' gauge configurations, the inversion of $\not{D}_W + m$ diverges and damages the ensemble average.

The effects of exceptional configurations are removed by twisted mass fermions [21]. In this discretisation an extra term $+i\mu\gamma_5\tau_3$ is added, where τ_3 is an $SU(2)$ generator acting in flavour space. The twisted mass Dirac operator is then

$$\not{D}_{twist} = \not{D}_W + m + i\mu\gamma_5\tau_3. \tag{1.24}$$

It has determinant [22]

$$\det \not{D}_{twist} = \det((\not{D}_W + m)^\dagger(\not{D}_W + m) + \mu^2) > 0 \tag{1.25}$$

so avoids the problem of exceptional configurations because there cannot be any zero eigenmodes of $\not{D}_{twist}$.

Twisted mass QCD reproduces QCD away from $\mu = 0$ because for a chiral rotation

$$\psi \to e^{i\alpha\gamma_5\frac{\tau_3}{2}}\psi \tag{1.26}$$

with $\alpha = \tan^{-1}\frac{\mu}{m}$ the twisted mass action becomes

$$\bar{\psi}(\not{D}_W + M)\psi \tag{1.27}$$

where $M = \sqrt{m^2 + \mu^2}$. At maximal twist, $\alpha = \frac{\pi}{2}$, twisted mass fermions can be used in simulations with the leading errors $\mathcal{O}(a^2)$ [21].

Staggered fermions

Staggered fermions are the lattice fermions used for the physical results presented in this thesis.

They reduce the 16-fold doubling to 4-fold by trivialising the Dirac spin index in the action of Equation 1.13 using the staggering transformation [23] given by

$$\psi(i) \to \Omega(i)\chi(i), \tag{1.28}$$

where

$$\Omega(i) = \prod_{\mu} \gamma_{\mu}^{i_\mu}. \tag{1.29}$$

Applying this transformation gives the staggered action

$$\mathcal{S}_{stag} = \sum_{i} \bar{\chi}(i)((-1)^{i_\mu^<}\Delta_\mu + m)\chi(i) \tag{1.30}$$

which is diagonal in spin space. It is convenient to use the notation

$$i_\mu^< = \sum_{\nu<\mu} i_\nu \tag{1.31}$$

for the phase factor in the staggered action.

The Dirac γ matrices no longer appear explicitly in the action, having been replaced by position dependent ± 1 phases. Because there is no dependence on the spinor component in the action, the four components of $\chi(i)$ are equivalent and three of them can be discarded. This leaves $\chi(i)$ as a one-component spinor, which is cheaper to simulate with. It also reduce the doublers by 1/4 and leaves only 4. With staggered quarks, these 4 remaining doublers are usually called 'tastes'.

The tastes remain in staggered simulations and must be accounted for in both the valence quarks and the sea quarks.

Chapter 2

Lattice QCD with staggered fermions

2.1 Calculations with staggered fermions

In simulations with staggered quarks, only one spinor component is used in the simulation. Four tastes are left and all four propagate in staggered quark loops. For the valence quarks, this can be accounted for by dividing the correlation functions by a factor of 4. Simulations with staggered quarks are further complicated by the appearance of oscillations in the correlator and the need to sometimes consider non-local meson operators.

2.1.1 Point split operators

The position dependent staggering transformation $\Omega(i)$ only depends on the position of the site i in a hypercube, i.e. on whether the lattice coordinates of the site are even or odd. This follows trivially from $(\gamma_\mu)^2 = 1$ and means that $\Omega(i + 2\hat{\mu}) = \Omega(i)$.

For practical calculations with staggered fields, $\chi(i)$, it can be useful to relate them to naive fermions, $\psi(i)$. A 2-point correlator with naive quarks is

$$\sum_{i,j} \langle \bar{\psi}(i)\Gamma_1\psi(i)\bar{\psi}(j)\Gamma_2\psi(j)\rangle, \tag{2.1}$$

where $\psi(i)$ is a 4-component spinor and the sum over sites i and j is over sites on the same timeslice. The naive version of the correlator must be spin diagonal to write it using 1-component staggered fields because $\chi(i)$ only contains one spin component. This means that the correlator must be able to be written so that all the Dirac γ matrices cancel out and are replaced by $\pm$ phase factors. For local operators, this means that Γ_1 and Γ_2 must be the same. This restriction can be avoided by using non-local meson operators, $\bar{\psi}(i)\Gamma\psi(i')$ where the sites i and i' are within the same hypercube. This changes the γ matrix content of the correlator because $\Omega(i + \hat{\mu}) = \pm\gamma_\mu\Omega(i)$, so an operator containing one link of point splitting in the μ direction contains an extra

γ_μ when the staggered transformation is applied. When working with gauge fixed configurations, the gauge links can be ignored in point-split operators; most of the calculations in this thesis were carried out with configurations in the Coulomb gauge.

The spin of a staggered meson operator determines what J^{PC} it couples to and is written γ_n. The taste of the operator, γ_s, is the total γ matrix content of the operator after the staggering transformation has been applied. The operator is defined by its spin and taste and can be written as $\gamma_n \otimes \gamma_s$. Including point splitting, this general operator looks like

$$\bar{\chi}(i)\Omega^\dagger(i)\gamma_n\Omega(i+n+s)\chi(i+n+s), \tag{2.2}$$

where the point splitting is such that

$$\Omega^\dagger(i)\gamma_n\Omega(i+n+s) = \pm\gamma_s. \tag{2.3}$$

All staggered operators with the same spin γ_n create different tastes of meson. At finite lattice spacing, the masses of these mesons differ slightly, but they are the same in the continuum limit because the taste-splitting is a discretisation effect. With improved staggered quark actions, the taste-splitting is very small and it typically doesn't matter which taste of meson is used in simulations. This means different tastes are used depending on which is most suitable for the calculation. Taste-splittings for charmonium mesons are considered in Section 5.3.3. The taste-splittings for D_s mesons are compared in Section 7.4.2.

2.1.2 Oscillations

In simulations with staggered quarks, the correlators are complicated by the presence of oscillating contributions. These appear as terms which have an additional time dependence of $(-1)^t$ and are due to the extra tastes arising from fermion doubling.

The action of Equation 1.13 is invariant under the transformation

$$\psi(k) \to i\gamma_5\gamma_\rho(-1)^{k_\rho}\psi(k). \tag{2.4}$$

A field, $\psi(i)$, intended to describe a quark with low energy will also describe 15 other quarks with large momentum. A field describing a quark at rest will have zero momentum, so it will respond to a momentum operator as $p_\rho\psi(i) = -i\partial_\rho\psi(i) = 0$. As before, the doubler quarks correspond to quarks with momentum of $\frac{\pi}{a}$:

$$-i\partial_\rho(i\gamma_5\gamma_\rho(-1)^{k_\rho}\psi(k)) = -i\partial_\rho(i\gamma_5\gamma_\rho e^{ik_\rho\pi/a}\psi(k)) = \frac{\pi}{a}i\gamma_5\gamma_\rho e^{ik_\rho\pi/a}\psi(k) \tag{2.5}$$

where the factor of a appears because the lattice points are separated by a distance a. There are 15 doublers in total because the transformation can be applied sequentially

in any of 4 space-time directions and it is clear that the action will be invariant under

$$\psi(i) \to i\gamma_5\gamma_\rho(-1)^{i_\rho}[i\gamma_5\gamma_\sigma(-1)^{i_\sigma}\psi(i)] \tag{2.6}$$

for any pairs of directions ρ and σ.

In a correlation function as Equation 2.1, there is a sum over space but not time. This means that the doublers with a factor $(-1)^x$ will cancel out in the sum, but the doubler with $(-1)^t$ will not. Therefore, Equation 2.1 will contain an extra contribution (with the previously discussed restriction $\Gamma_1 = \Gamma_2 = \Gamma$ now enforced)

$$(-1)^{j_t - i_t} \sum_{i,j} \langle \bar{\psi}(i)\gamma_5\gamma_t\Gamma\psi(i)\bar{\psi}(j)\gamma_5\gamma_t\Gamma\psi(j)\rangle. \tag{2.7}$$

This oscillating contribution couples to states with opposite parity to the non-oscillating piece. Oscillations commonly appear in staggered simulations and can easily be dealt with in the analysis.

2.1.3 Staggered operator phases

Staggered correlation functions must contain a taste-singlet combination of operators, so the operators used in a calculation must be chosen such that the product of all their tastes is 1. The staggered correlator then includes a position dependent phase factor coming from anticommuting the γ matrices so they can be cancelled out, which can be found in a systematic way.

To work out the phase of a staggered operator, it is convenient to use the notation

$$i_\mu^< = \sum_{\nu<\mu} i_\nu, \tag{2.8}$$

which arises from extracting the extra γ matrices to the front of a point-split staggering transformation

$$\Omega(i + \hat{\mu}) = (-1)^{i_\mu^<}\gamma_\mu\Omega(i). \tag{2.9}$$

It is also convenient to introduce

$$\varepsilon(i) = (-1)^{\sum_\mu i_\mu} \tag{2.10}$$

which appears in the phase factor which comes from anticommuting $\Omega(i)$ with γ_5

$$\Omega(i)\gamma_5 = \varepsilon(i)\gamma_5\Omega(i). \tag{2.11}$$

It is also convenient to introduce

$$\bar{i}_\mu = \sum_{\nu\neq\mu} i_\nu, \tag{2.12}$$

which is in the phase from anticommuting $\Omega(i)$ with γ_μ

$$\Omega(i)\gamma_\mu = (-1)^{\bar{i}_\mu}\gamma_\mu\Omega(i) \tag{2.13}$$

and also

$$i_\mu^> = \sum_{\nu>\mu} i_\nu, \tag{2.14}$$

which appears in the phase factor resulting from pulling the extra γ matrices out to the right of $\Omega(i)$,

$$\Omega(i+\hat{\mu}) = (-1)^{i_\mu^>}\Omega(i)\gamma_\mu. \tag{2.15}$$

These phase factors are useful when working out and writing down the phase factors for staggered operator and obey the straightforward relations

$$(-1)^{i_\mu^>}\varepsilon(i) = (-1)^{i_\mu^< + i_\mu} \tag{2.16}$$

and for $\mu \neq \nu$

$$(-1)^{\bar{i}_\mu + \bar{i}_\nu} = (-1)^{i_\mu + i_\nu}. \tag{2.17}$$

To work out its phase, consider a general staggered operator $\gamma_n \otimes \gamma_s$. Each γ matrix can be represented as a 4-component binary vector (i.e. each component is 0 or 1) written as (n_1, n_2, n_3, n_4), such that $\gamma = \gamma_1^{n_1}\gamma_2^{n_2}\gamma_3^{n_3}\gamma_4^{n_4}$. The operator has a point splitting $n+s$, where the binary vectors are added mod 2 for each component. After applying the staggering transformations, the operator can be written as

$$\bar{\chi}(i)\Omega^\dagger(i)\gamma_n\Omega(i+n+s)\chi(i+n+s). \tag{2.18}$$

The first step is to extract the 'extra' γ matrices from the point split staggered transformation matrix. Equivalently, this means finding the phase factor arising from writing $\Omega(i+n+s)$ as $\gamma_{(n+s)}\Omega(i)$. For each component of $(n+s)_\mu = 1$, this gives a factor of $(-1)^{i_\mu^<}$ and is done from $i = 1$ to 4 in numerical order. These anticommutions bring the operator to

$$\left(\prod_{(n+s)_\mu=1}(-1)^{i_\mu^<}\right)\bar{\chi}(i)\Omega^\dagger(i)\gamma_n\gamma_{(n+s)}\Omega(i)\chi(i+n+s) \tag{2.19}$$

and it is clear that $\gamma_n\gamma_{(n+s)} = \pm\gamma_s$, where the $\pm$ is position independent and therefore just an overall factor. The next step is to anticommute γ_s with $\Omega(i)$ so the staggering transformations can cancel out. This gives a factor of $(-1)^{\bar{i}_\mu}$ for each μ for which $s_\mu = 1$ so the overall phase for the operator is

$$\left(\prod_{(n+s)_\mu=1}(-1)^{i_\mu^<}\right)\left(\prod_{s_\mu=1}(-1)^{\bar{i}_\mu}\right). \tag{2.20}$$

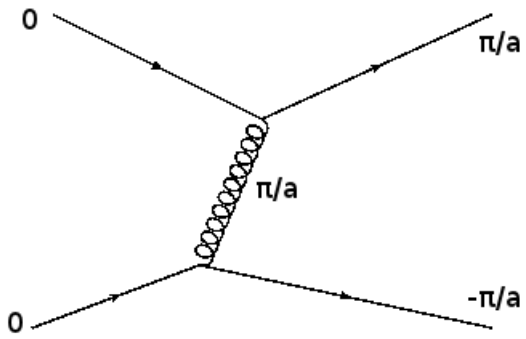

Figure 2.1: A taste exchange interaction where a low energy quark emits a gluon with energy π/a and changes to another taste, which also resembles a low energy quark. The gluon is reabsorbed by another quark, which also changes taste and this process is unphysical.

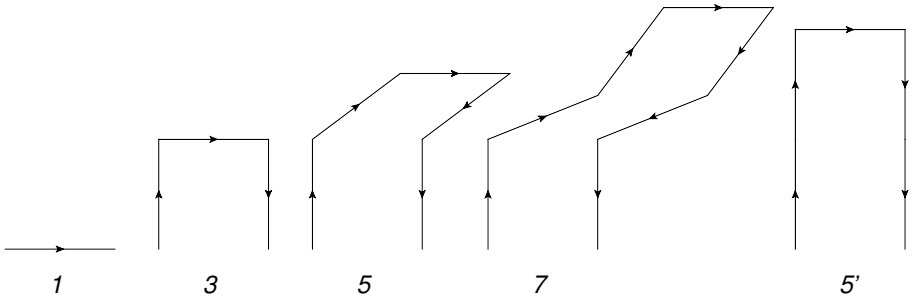

Figure 2.2: The 3-link, 5-link and 7-link smeared gauge links which are included in the asqtad action to remove the coupling of quarks to high energy gluons.

The final consideration for staggered quark phases is the difference between quark and antiquark propagation. If the 4 spinor component propagator $G(i,j)$ describes a naive quark propagating from i to j, then $\gamma_5 G^\dagger(i,j)\gamma_5$ describes an antiquark propagating from i to j. This leads to the relation for staggered propagators that $g^\dagger(i,j)$ and $g^\dagger(i,j)\varepsilon(i)\varepsilon(j)$ respectively describe a staggered quark and antiquark propagating between i and j.

2.2 Improved staggered quarks

A large source of errors for unimproved staggered quarks is taste-exchange interactions, in which quarks exchange high-energy gluons. A low-energy quark can emit a gluon with any components of four-momentum equal to π/a and, rather than becoming off-shell, changes into a quark of another taste, which has high momentum but resembles the original low-energy quark due to the doubling symmetry. The gluon can then be absorbed by another quark, which also changes taste. This process is shown in Figure 2.1. This interaction does not appear in continuum QCD and is a consequence of the lattice doubling symmetry, so it introduces discretisation errors.

Taste-exchange interactions can be removed from simulations by reducing the coupling between quarks and high momentum gluons to zero [24, 25, 26]. This can be done by replacing the gauge links with fattened links including a combination of 3-link, 5-link and 7-link paths between neighbouring sites. The link fattening in [25] introduces a new lattice artefact, which can be corrected by adding another 5-link term – the Lepage term – to the fattened gauge links [27]. The terms which go into the link fattening are shown in Figure 2.2, where the right-most one is the Lepage term.

The fermion action can be further improved by introducing a 3-link term in the discretised derivative, called the Naik term [28]. For staggered fermions, this does not upset the phase factor because $\Omega(i+3\hat{\mu}) = \Omega(i+\hat{\mu})$ so the 3-link term behaves exactly the same way as a one-link term.

This action is improved to $\mathcal{O}(a^2)$ and is called the asqtad (a^2 tadpole improved) action.

The fattened gauge links act as a form factor which vanish for coupling to gluons with momentum $p \simeq \pi/a$. Explicitly, the form factor is given by

$$\mathcal{F}_\mu = \prod_{\rho\neq\mu} \left(1 + \frac{a^2\delta_\rho^{(2)}}{4}\right), \tag{2.21}$$

where

$$\begin{aligned}\delta_\rho^{(2)} U_\mu(x) = \frac{1}{a^2}\big(&U_\rho(x)U_\mu(x+\hat{\rho})U^\dagger(x+\hat{\mu}) - 2U_\mu(x) \\ &+ U_\rho^\dagger(x-\hat{\rho})U_\mu(x-\hat{\rho})U_\rho(x-\hat{\rho}+\hat{\mu})\big)\end{aligned} \tag{2.22}$$

The smearing for the asqtad action also includes the Lepage term:

$$\mathcal{F}_\mu^{asqtad} = \mathcal{F}_\mu - \sum_{\rho\neq\mu} \frac{a^2(\delta_\rho)^2}{4}, \tag{2.23}$$

where

$$\begin{aligned}\delta_\rho U_\mu(x) = \frac{1}{a}\big(&U_\rho(x)U_\mu(x+\hat{\rho})U_\rho^\dagger(x+\hat{\mu}) \\ &- U_\rho^\dagger(x-\hat{\rho})U_\mu(x-\hat{\rho})U_\rho(x+\hat{\mu}-\hat{\rho})\big)\end{aligned} \tag{2.24}$$

The asqtad action is then

$$\mathcal{S}_{asqtad} = \sum_i \bar{\psi}(i)\{\gamma_\mu(\Delta_\mu(V) - \frac{1}{6}\Delta_\mu^3(U)) + m\}\psi(i), \tag{2.25}$$

where $V_\mu(x) = \mathcal{F}_\mu^{asqtad} U_\mu(x)$. The one-link deriative is Δ_μ and the three term in the deriative is Δ_μ^3.

2.2.1 Highly Improved Staggered Quarks

The main source of errors in the asqtad action comes from taste exchange in loops. This effect can be significantly reduced by multiple iterations of the link smearing process [29]. Repeated smearings enhance diagrams with two-gluon vertices because the gauge links are replaced with a sum over many combinations of products of links. This is dealt with by reunitarising the gauge links after smearing.

In the Highly Improved Staggered Quark (HISQ) action [29], this smearing operation is applied twice with a reunitarisation of the smearing gauge links after the first smearing. For charm quarks, the largest remaining discretisation errors are $\mathcal{O}((am)^4)$ and can be removed by tuning the Naik term coefficient, which appears in the action as $(1+\epsilon_N)$. The tuning ϵ_N is not important for light (up, down and strange) quarks and can be tuned for charm quarks to give the right dispersion relation. This means that charm quarks can be accurately simulated with the HISQ action.

The smearing used in the HISQ action can is then [29]

$$\mathcal{F}_\mu^{HISQ} = \left(\mathcal{F}_\mu - \sum_{\rho\neq\mu} \frac{a^2(\delta_\rho)^2}{2}\right)\mathcal{U}\mathcal{F}_\mu \tag{2.26}$$

where $\mathcal{U}$ denotes a reunitaritisation of the gauge links. The correction from the Lepage term is moved to apply to the second smearing step.

The HISQ action can be written as

$$\mathcal{S}_{HISQ} = \sum_i \bar{\psi}(i)\{\gamma_\mu(\Delta_\mu(W) - \frac{1}{6}(1+\varepsilon_N)\Delta_\mu^3(X)) + m\}\psi(i). \tag{2.27}$$

The gauge links are $W_\mu(x) = \mathcal{F}_\mu^{HISQ}U_\mu(x)$ in the 1-link difference and the Naik term includes ϵ_N and gauge links $X_\mu = \mathcal{U}\mathcal{F}_\mu U_\mu(x)$.

In this thesis, the fermion action used for the valence quarks in all simulations is the HISQ action.

2.3 Gauge configurations with staggered sea quarks

The QCD action contains terms for both the gluons and the quarks. In simulations of full QCD, the gauge configurations representing the QCD vacuum must include the effects of dynamical sea quark loops. Because the quarks are fermions, they are represented by anticommuting Grassmann variables. The path integral, in which the action appears, can be written as

$$\int [dU_\mu][d\bar{\psi}][d\psi] e^{-S_g + \bar{\psi}(\not{D}(U_\mu)+m)\psi}, \tag{2.28}$$

where S_g is the gauge action. It does not contain Grassmann variables and can be integrated over simply by generating a ensemble of sample gauge configurations.

The fermionic part of the action is more difficult because the anticommuting Grassmann variables cannot be easily simulated by a computer, so this integral is done analytically. For Grassmann numbers $\bar{\psi}$ and ψ [30]

$$\int [d\bar{\psi}][d\psi] e^{\bar{\psi}(\not{D}(U_\mu)+m)\psi} = \det(\not{D}(U_\mu)+m). \tag{2.29}$$

After this integration, the path integral is

$$\int [dU_\mu] e^{-S_g + \ln(\det(\not{D}(U_\mu)+m))}. \tag{2.30}$$

Including the effects of sea quarks is expensive computationally and becomes more difficult for smaller quark masses. An approximation made in the past to simplify the action was $\not{D}(U_\mu) + m = 1$, which removes the effects of sea quarks entirely. This approach is known as the quenched approximation and leads to systematic errors from neglecting the sea quarks. These errors can be $\mathcal{O}(10\%)$ [31].

Modern lattice calculations use gauge configurations generated with unphysically heavy up and down quarks in the sea to reduce the cost. Simulating at different sea quark masses allows an extrapolation to be made to the physical limit. Some new gauge configurations have been generated with physical light masses [32, 33, 34].

2.3.1 Rooted staggered sea quarks

Most of the calculations of semileptonic and radiative meson decays presented in this thesis are made using gauge configurations generated by the MILC Collaboration with $N_f = 2+1$ flavours of sea quark [35]. The up and down quarks are taken to be degenerate in mass and both are unphysically heavy, while the strange quark is also included in the sea at approximately its physical mass. These sea quarks are simulated with the asqtad improved staggered action. More recently generated MILC configurations also include the effects of charm quarks in the sea and all the sea quarks are simulated with the further improved HISQ action [36].

These ensembles use staggered sea quarks, which means there are four tastes in the sea and they must be accounted for. To deal with this, the fourth root of the determinant is taken to remove the three extra tastes (this step is known as rooting).

The fourth root is motivated by the expectation that the tastes are equivalent in the continuum, so the determinant is just four copies of the same fermion determinant. If the tastes can be taken to be equivalent and taste-exchange interactions neglected, then the Dirac operator would have a matrix structure

$$\not{D}+m = \begin{pmatrix} \not{D}_1+m & 0 & 0 & 0 \\ 0 & \not{D}_1+m & 0 & 0 \\ 0 & 0 & \not{D}_1+m & 0 \\ 0 & 0 & 0 & \not{D}_1+m \end{pmatrix}, \tag{2.31}$$

in which $\not{D}_1 + m$ is a 1 taste Dirac operator.

From Equation 2.31, rooting is justified as

$$\sqrt[4]{\det(\not{D} + m)} = \det(\not{D}_1 + m). \tag{2.32}$$

The off-diagonal entries in Equation 2.31 are non-zero when taste-exchange is allowed, which complicates this picture at finite lattice spacing. However, the off-diagonal entries should vanish as $a \to 0$ and so recover the picture of Equation 2.31, in which rooting is justified.

However, the validity of the rooting procedure has not been rigorously proven and is controversial [37, 38, 39]. It is an important theoretical consideration to test to the validity of the fourth root, which can be done by considering the behaviour of the eigenvalues and eigenvectors of the staggered $\not{D}$ operator.

Whilst the study is motivated by rooting, the structure of $\not{D}$ can be examined for staggered valence quarks on quenched gauge configurations [40].

2.4 Low-lying eigenvalues of $\not{D}_{stag}$

A numerical test of rooting can be obtained by looking at the eigenvalues of the massless staggered Dirac operator $\not{D}_{stag}$. Numerical studies of the eigenvalues [41, 42, 43, 44] show that they appear in quartets which become increasingly degenerate in the limit $a \to 0$. Taking the fourth root of the determinant averages over the four equivalent eigenvalues.

In Figure 2.3, my calculation of the low-lying eigenvalue spectrum is shown for three configurations of different lattice spacing. Each of these configurations includes one quartet of modes with near-zero eigenvalues. These near-zero eigenvalues appear with two on either side of zero and the spread in the quartet decreases with lattice spacing.

2.4.1 Continuum zero modes

In the continuum, the eigenmodes of the Dirac operator obey symmetries which should also be visible in the lattice simulation. If ϕ_A is an eigenvector of the massless Dirac operator $\not{D}$, the corresponding eigenvalue is purely imaginary:

$$\not{D}\phi_A = i\lambda_A\phi_A. \tag{2.33}$$

The eigenvectors of $\not{D}$ are orthogonal, so $\phi_A^\dagger\phi_B = \delta_{AB}$. From the fact that γ_5 anticommutes with $\not{D}$, it follows that $\gamma_5\phi_A$ is also an eigenvector with eigenvalue $-i\lambda_A$. The chirality of an eigenvector is defined as $\chi_A = \phi_A^\dagger\gamma_5\phi_A$ and $\chi = 0$ unless $\lambda_A = 0$ because the eigenvectors are orthogonal.

If $\not{D}$ has zero-modes – eigenmodes with eigenvalue $\lambda_A = 0$ – then ϕ_A and $\gamma_5\phi_A$ are

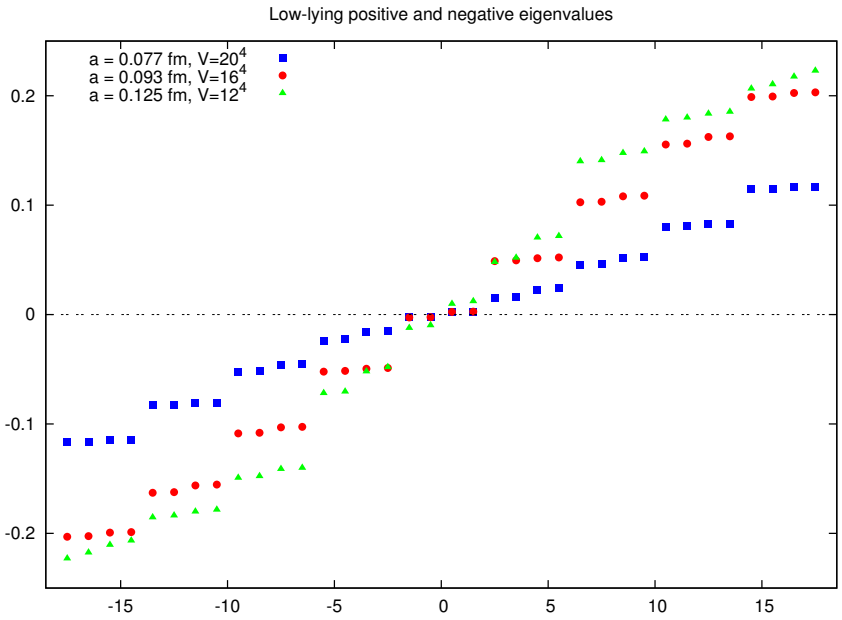

Figure 2.3: The 20 lowest-lying eigenvalues of a sample $|Q| = 1$ gauge configuration with lattice spacings $a = 0.125$ fm, $a = 0.093$ fm and $a = 0.077$ fm. These configurations have approximately the same physical volume. The x-axis is eigenvalue number, where the smallest positive eigenvalue is eigenvalue 1 and the smallest negative eigenvalue is eigenvalue -1.

not orthogonal and the mode has chirality $\chi_A = \pm 1$. The number of zero-modes on a gauge configuration is related to the topology of the gauge fields by the Atiyah-Singer Index Theorem [45] by

$$Q = \frac{1}{32\pi^2} \int d^4x \mathrm{Tr} F_{\mu\nu}(x) F_{\rho\sigma}(x) \varepsilon_{\mu\nu\rho\sigma} = n_+ - n_-, \tag{2.34}$$

where $n_\pm$ is the number of modes with positive or negative chirality and $F_{\mu\nu}$ is the gluon field strength tensor. Q is called the topological charge of the configuration and is a topological invariant.

Q can be calculated from the gluon fields and, if $|Q|$ is non-zero, indicates the presences of zero modes; in the continuum these are eigenfunctions of $\not{D}$ with eigenvalue 0 and chirality ± 1.

2.4.2 Lattice near-zero modes

With staggered fermions, each continuum zero mode of the massless $\not{D}$ is replaced by a quartet of near-zero modes. These modes do not have eigenvalues of exactly 0 on the lattice, nor do they have chirality of exactly ± 1.

On the lattice, the phase factor $\varepsilon(i) = (-1)^{i_x+i_y+i_z+i_t}$ anticommutes with the staggered Dirac operator, so there is a continuum-like symmetry between the lattice eigenmodes $f_A(i)$ and $\varepsilon(i) f_A(i)$. As in the continuum, the eigenvalues of the massless lattice $\not{D}_{stag}$ operator are purely imaginary and here $\varepsilon(i)$ plays the role of γ_5 in the continuum.

It follows that

$$\not{D}_{stag} f_A(i) = i\lambda_A f_A(i) \implies \not{D}_{stag}\varepsilon(i) f_A(i) = -i\lambda_A \varepsilon(i) f_A(i) \tag{2.35}$$

and this applies to the near-zero modes as well as the non-zero modes. Therefore, the near-zero quartets are made up of 2 modes with small positive eigenvalues and 2 with (related) negative eigenvalues. Because of the symmetry between positive and negative eigenvalues, it is sufficient to calculate only the positive half of the eigenvalue spectrum.

For the eigenmodes of the staggered Dirac operator, the chirality must be defined using the appropriate staggered γ_5 operator, which is the taste-singlet $\gamma_5 \otimes 1$ [46]. This staggered operator resembling γ_5 in the continuum is not the same $\varepsilon(i)$ as before. Here the taste-singlet operator must be used as it is the only taste with the right gluonic coupling and is the one that must be used to study flavour-singlet mesons such as the η' with staggered quarks. It is a four-link point-split operator, where the four-links are in each of the four orthogonal lattices directions. In practice, the chirality is calculated by averaging over all of the possible directions and orders of these links.

The four near-zero modes in a quartet have the same chirality. This is straightforward to show for the 'mirror' eigenmodes:

$$f_A^\dagger(i)(\gamma_5 \otimes 1) f_A(i) = f_A^\dagger(i)\varepsilon(i)(\gamma_5 \otimes 1)(\varepsilon(i) f_A(i)). \tag{2.36}$$

The 4-link operator shifts $\varepsilon(i)$ to $\varepsilon(i + \hat{x} + \hat{y} + \hat{z} + \hat{t}) = (-1)^4\varepsilon(i) = \varepsilon(i)$. That the two positive modes also have the same chirality has been shown empirically by numerical simulation [42]. The near-zero modes on the lattice can thus still be identified as modes with small eigenvalues and high chirality, similarly to as in the continuum.

In Figure 2.4, my results for the eigenvalue of the 4 lowest-lying positive eigenvalued modes is plotted against the modes' chirality for gauge configurations with $|Q| = 1$. These gauge configurations are expected to contain 4 near-zero modes (so 2 with positive eigenvalues), so the smallest eigenvalues plotted in Figure 2.4 should correspond to the near-zero modes and therefore have non-zero chirality. On the finest lattice configurations, the separation of chirality between the near-zero and non-zero modes is clearest.

The cut-off $\chi = 0.4$ is shown in Figure 2.4, which was used to assign the topological charge of a gauge configuration. This fermionic method was compared to gluonic methods of measuring the topological charge. The disagreement between the assignment of Q using the chirality and gluonic definitions was found in [42] to be the same as the ambiguity between different gluonic definitions and to improve for finer lattice spacings.

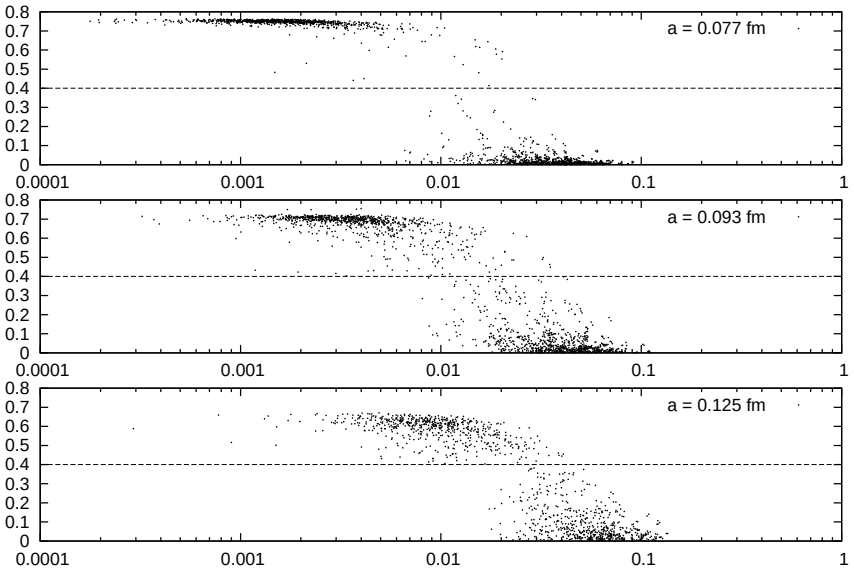

Figure 2.4: A plot of chirality against eigenvalue for the 4 lowest-lying modes with positive eigenvalue on gauge configurations with $|Q| = 1$ for lattice spacings $a = 0.125$ fm, $a = 0.093$ fm and $a = 0.077$ fm. Also plotted is the line $\chi = 0.4$ used to assign configurations to sectors of topological charge by the chirality of the low-lying modes.

2.4.3 Criticisms of rooting

It is suggested in [37] that rooted staggered fermions give the wrong answer for topologically sensitive quantities, such as for flavour-singlet mesons. The η' is a flavour-singlet pseudoscalar containing light quarks and has a much larger mass than flavour non-singlet mesons, due to its interactions with gauge field topology. The 't Hooft vertex [47] describes interactions between flavour-singlet mesons and zero modes of the gauge field that give the η' meson a non-zero mass in the chiral limit $m_q \to 0$.

Reference [37] contends that the 't Hooft vertex for staggered fermions generates contributions to the η' correlator that diverge in the chiral limit. This is inconsistent with the expectation that the η' should remain massive in the limit of zero quark mass. Due to the disconnected diagrams, simulations of the η' meson [48, 49] are difficult.

The conclusions of [37] are refuted in [39], which concludes that there will be no divergent contribution to the η' correlator if the eigenvectors of different tastes decouple. To investigate this criticism of rooted staggered quarks requires study of the eigenvectors of $\not{D}_{stag}$, which is described in Chapter 3.

Chapter 3

Eigenvectors of $\not{D}_{stag}$

3.1 Zero mode contributions to correlators

To see the effect of the zero modes, consider the connected and disconnected parts of a flavour- and taste-singlet meson correlator. Whilst the pseudoscalar case is particularly important, these contributions can be found for any taste-singlet operator, Γ.

Allowing for point-splitting in the operators, the correlation function

$$\langle \bar{\psi}(i)\Gamma\psi(i')\bar{\psi}(j)\Gamma'\psi(j')\rangle \tag{3.1}$$

can be Wick contracted to give either a connected or disconnected piece.

Figure 3.1 shows the connected (above) and disconnected (below) contributions to the correlator. The disconnected piece only contributes for flavour-singlet mesons because only they can couple to purely gluonic intermediate states.

The connected piece is given by

$$C(i,j) = \mathrm{Tr}(G(i',j)\Gamma' G(j',i)\Gamma), \tag{3.2}$$

and the disconnected piece by

$$D(i,j) = \mathrm{Tr}(G(i',i)\Gamma)\mathrm{Tr}(G(j',j)\Gamma'). \tag{3.3}$$

The expression for the disconnected correlator contains $\mathrm{Tr}(\Gamma)$ so there will only be a disconnected piece if Γ is a taste-singlet staggered operator. This makes it particularly clear that the only appropriate staggered operator to use for flavour-singlet mesons is the taste-singlet.

Writing the connected part in terms of the eigenvectors and eigenvalues of the Dirac operator gives

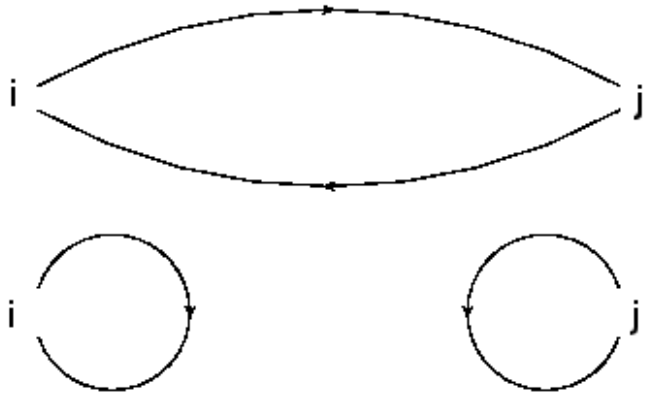

Figure 3.1: Diagrams of the connected and disconnected contributions to a 2-point flavour-singlet meson correlator for a meson propagating between lattice sites i and j. The connected contribution ($C(i,j)$) is shown above the disconnected one ($D(i,j)$).

$$\begin{aligned}
C(i,j) =& \mathrm{Tr}(G(i',j)\Gamma' G(j',i)\Gamma) \\
=& \mathrm{Tr}\left(\sum_A \frac{1}{i\lambda_A + m} f_A(i') f_A^\dagger(j)\Gamma' \sum_B \frac{1}{i\lambda_B + m} f_B(j') f_B^\dagger(i)\Gamma\right) \\
=& \sum_{A,B} \frac{1}{(i\lambda_A + m)(i\lambda_B + m)} (f_A(i'))_a (f_A^\dagger(j))_b (\Gamma')_{bc} (f_B(j'))_c (f_B^\dagger(i))_d (\Gamma)_{da} \\
=& \sum_{A,B} \frac{1}{(i\lambda_A + m)(i\lambda_B + m)} f_A^\dagger(j)\Gamma' f_B(j') f_B^\dagger(i)\Gamma f_A(i'), \qquad (3.4)
\end{aligned}$$

using the eigenvalue-eigenvector representation of the quark propagator

$$G(i,j) = \sum_A \frac{1}{i\lambda_A + m} f_A(i) f_A^\dagger(j). \qquad (3.5)$$

The propagator can be written in terms of the eigenvectors of $\not{D} + m$ because it is in the inverse of $\not{D} + m$. The sum is over the eigenvectors $f_A(i)$ and $f_B(i)$, where $(\not{D} + m) f_A(i) = (i\lambda_A + m) f_A(i)$.

Similarly, the eigenvalue-eigenvector representation of the disconnected correlator is given by

$$D(i,j) = \left(\sum_A \frac{1}{(i\lambda_A + m)} f_A^\dagger(i)\Gamma f_A(i')\right)\left(\sum_B \frac{1}{(i\lambda_B + m)} f_B^\dagger(j)\Gamma' f_B(j')\right). \qquad (3.6)$$

The correct way to combine these pieces to give the total correlator $T(i,j)$ is [39]

$$T(i,j) = -\frac{1}{4} C(i,j) + \frac{1}{16} D(i,j). \qquad (3.7)$$

For each closed quark loop, there is a factor of $\frac{1}{4}$ for the four tastes; there are two of

these in the disconnected correlator. The relative minus sign for the two contributions comes from Fermi statistics.

For staggered fermions to reproduce the correct continuum result and avoid the total correlator diverging in the chiral limit, the different tastes must decouple. This means that ζ^{Γ}_{AB}, defined as

$$\zeta^{\Gamma}_{AB} = f^{\dagger}_{A}(i)\Gamma f_{B}(i'), \tag{3.8}$$

where some point-splitting associated with the staggered meson operator Γ is permitted, must satisfy

$$\zeta^{\Gamma}_{AB} = 0 \text{ for } A \neq B \tag{3.9}$$

up to discretisation effects which are expected to be proportional to a^2 [50].

In the chiral limit, the near-zero modes will dominate both the connected and disconnected correlators, as can be seen from the eigenvector-eigenvalue representation. For configurations with Q=1, there are four near zero modes. Ignoring the non-zero modes and assuming that the off-diagonal $\zeta^{\Gamma}_{AB} \sim 0$ means

$$D(i,j) \sim \left(\sum_{4 \text{ modes}} \frac{1}{m} \zeta^{\Gamma}_{AA} \right)^2 = \left(\frac{4}{m} \zeta^{\Gamma}_{AA} \right)^2 \tag{3.10}$$

and

$$C(i,j) \sim \sum_{4 \text{ modes}} \frac{1}{m^2} \left(\zeta^{\Gamma}_{AA} \right)^2 = \frac{4}{m^2} \left(\zeta^{\Gamma}_{AA} \right)^2, \tag{3.11}$$

which, when combined according to Equation 3.7, will leave no contribution proportional to $\frac{1}{m^2}$ that diverges in the limit $m \to 0$.

The off-diagonal overlaps should behave in the same way for all Γ. The diagonal eigenvector overlaps are each expected to behave in a similar way to the single continuum zero modes and the multiplicity of near-zero modes will be compensated by the taste factors included in the correlator.

3.1.1 Lattice calculation

The requirement that the staggered eigenvectors of different tastes must decouple in the $a \to 0$ limit can be tested numerically by calculating and comparing the eigenvector overlaps ζ^{Γ}_{AB} for the diagonal and off-diagonal cases [40].

The gauge configurations used are listed in Table 3.1.1. Ensembles 1, 3 and 5 have different lattice spacings, but approximately the same physical volume. They can be used to examine the lattice spacing dependence. Ensembles 2, 3 and 4 have the same lattice spacing but different volumes, so the volume dependence can be checked.

These gauge configurations are the same as used in the previous eigenvalue study [42] and are quenched. In the last column of Table 3.1.1, the number of configurations determined to have topological charge of ± 1 is listed. Configurations with $|Q| = 1$ are convenient to study as they contain only one near-zero quartet.

Ensemble	β	a/fm	Volume	aL/fm	$\lvert Q\rvert = 1$
1	4.6	0.125	12^4	1.50	294
2	4.8	0.093	12^4	1.12	806
3	4.8	0.093	16^4	1.49	424
4	4.8	0.093	20^4	1.86	288
5	5.0	0.077	20^4	1.54	430

Table 3.1: Details of the gauge configurations used; the bare gauge coupling, lattice spacing, volume, physical size of the lattice and number of $|Q| = 1$ configurations in each ensemble.

The topological charge of a gauge configuration can be ambiguous at finite lattice spacing. Counting the number of eigenmodes with 'large' chirality agrees well with gluonic measurements and is straightforward to implement. The low-lying positive eigenvalues of the HISQ Dirac operator, $\not{D}_{HISQ}$, and their corresponding eigenvectors were calculated on each ensemble with a Lanczos algorithm. The code for the Lanczos algorithm was written by Eduardo Follana and used in the eigenvalue study in References [41, 42]. The eigenvectors are normalised such that

$$\sum_i f_A^\dagger(i) f_B(i) = \delta_{AB}. \tag{3.12}$$

This is true for the lattice near-zero modes as well as the non-zero modes because there are no exact zero eigenvalues.

As stated in Section 2.4.2, a cutoff of chirality $\chi_A > 0.4$ was used to define modes with large chirality. In Figure 2.4, $\chi = 0.4$ is plotted and lies in the gap between the near-zero and non-zero modes. On finer configurations, there are fewer modes with unclear chirality and it is easier to assign a value of $|Q|$. Gauge configurations with exactly $2|Q|$ positive eigenmodes with high chirality are deemed to have topological charge $|Q|$. Note that the sign of Q can be found from the sign of the modes' chirality, but the same behaviour is expected on gauge configurations with $\pm Q$. Few gauge configurations have an odd number of near-zero modes; the ones that do are not included in any of the $|Q| = 0, 1, 2$ sub-ensembles. The number of gauge configurations with ambiguous topological charge reduces with lattice spacing.

3.2 Results for $\zeta^\Gamma_{AB}(i)$

The eigenvector overlaps calculated are defined as

$$\zeta^\Gamma_{AB}(i) = \sum_{\text{hypercube}} f_A^\dagger(i) \Gamma f_B(i'), \tag{3.13}$$

where i is summed over a 2^4 hypercube and the point-split site i' is defined to be in the same hypercube as i. A lattice containing L^4 lattice sites contains $\frac{L^4}{16}$ hypercubes.

For $|Q| = 1$ configurations, there is one quartet of near-zero modes, denoted by $A = \pm 1, \pm 2$. The Lanczos algorithm gives only $f_1(i)$ and $f_2(i)$, from which $f_{-1}(i)$ and $f_{-2}(i)$ can be reconstructed. The phase factor $\varepsilon(i)$ divides the lattice into 2 halves; the even and odd sublattices for which $\varepsilon(i) = +1$ and $\varepsilon(i) = -1$ respectively. On the even sublattice $f_A(i) = f_{-A}(i)$ and on the odd $f_A(i) = -f_{-A}(i)$.

In the next sections, scatter plots of $\zeta^{\Gamma}_{AB}(i)$ on each hypercube for the 4 near-zero eigenvectors A, B are shown for several taste-singlet Γ. As there are a large number of hypercubes on a single configuration, the data plotted is $\zeta^{\Gamma}_{AB}(i)$ only for one or two sample configurations. For the pseudoscalar operator, which is sensitive to the chirality, two sample configurations are used – one with $Q = +1$ and one with $Q = -1$.

3.2.1 Pseudoscalar

The taste-singlet pseudoscalar operator contains 4 links of point splitting. For convenience, the site $(i+\hat{x}+\hat{y}+\hat{z}+\hat{t})$ is written as $(i+\hat{4})$. Explicitly applying the staggering transformation to the pseudoscalar correlator gives

$$\begin{aligned} C(i,j) &= \langle \bar{\chi}(i)\Omega^{\dagger}(i)\gamma_5\Omega(i+\hat{4})\chi(i+\hat{4})\bar{\chi}(j)\Omega^{\dagger}(j)\gamma_5\Omega(j+\hat{4})\chi(j+\hat{4})\rangle \\ &= (-1)^{i_x+i_z+j_x+j_z}\bar{\chi}(i)\chi(i+\hat{4})\bar{\chi}(j)\chi(j+\hat{4}) \\ &= \sum_{A,B}\frac{(-1)^{i_x+i_z+j_x+j_z}}{(i\lambda_A+m)(i\lambda_B+m)}f^{\dagger}_A(j)f_B(j+\hat{4})f^{\dagger}_B(i)f_A(i+\hat{4}). \end{aligned} \tag{3.14}$$

$$D(i,j) = \left(\sum_A \frac{(-1)^{i_x+i_z}}{(i\lambda_A+m)}f^{\dagger}_A(i)f_A(i+\hat{4})\right)\left(\sum_B \frac{(-1)^{j_x+j_z}}{(i\lambda_B+m)}f^{\dagger}_B(j)f_B(j+\hat{4})\right). \tag{3.15}$$

The eigenvector overlaps that these contributions to the flavour-singlet pseudoscalar correlator depend on are

$$\zeta^{\gamma_5}_{AB}(i) = \sum_{\text{hypercube}} (-1)^{i_x+i_z}f^{\dagger}_A(i)f_B(i+\hat{4}). \tag{3.16}$$

Due to the symmetries between the mirror eigenvectors, $\zeta^{\gamma_5}_{AB}(i)$ satisfies

$$\zeta^{\gamma_5}_{AB}(i) = \zeta^{\gamma_5}_{-A,-B}(i). \tag{3.17}$$

The sum over the hypercube in $\zeta^{\gamma_5}_{AB}(i)$ includes

$$(-1)^{i_x+i_z}f^{\dagger}_A(i)f_B(i+\hat{4}) + (-1)^{i_x+1+i_z+1}f^{\dagger}_A(i+\hat{4})f_B(i), \tag{3.18}$$

which means that $\zeta^{\Gamma}_{AA}(i)$ is purely real. Because $\sum_{\text{All hypercubes}}\zeta^{\gamma_5}_{AA}(i) = \chi_A$, where χ_A is the chirality of mode A, the values of $\zeta^{\gamma_5}_{AA}(i)$ should be mainly positive for the

configuration with $Q = +1$ and negative for the configuration with $Q = -1$. The off-diagonal pieces $\zeta^{\gamma_5}_{A,-A}(i)$ will also be real, but smaller than the diagonal pieces. This is because, rather than typically summing over sixteen terms with the same sign, the sum over the hypercube for $\zeta^{\gamma_5}_{A,-A}(i)$ will generally be over eight positive and eight negative terms for the even and odd lattice sites.

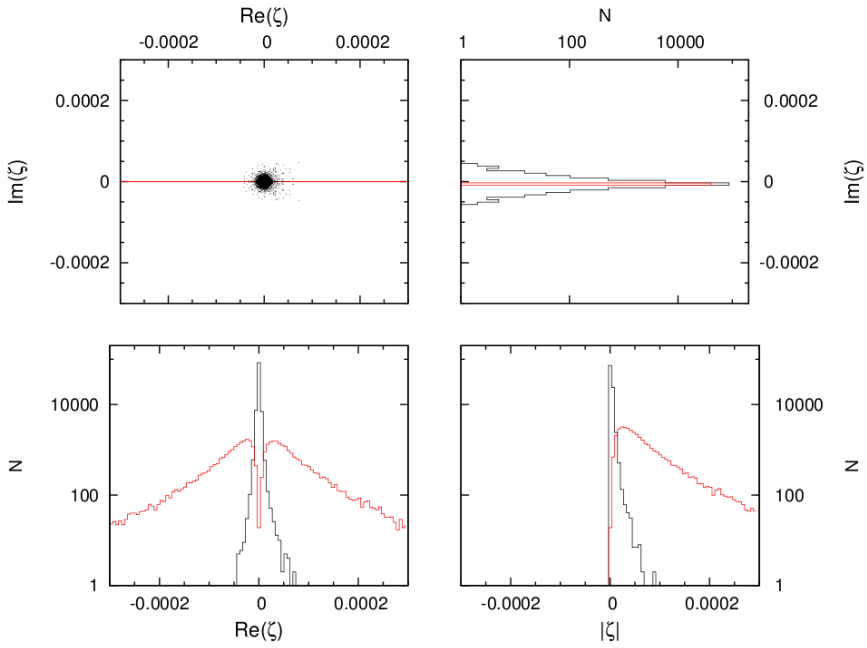

Figure 3.2: $\zeta^{\gamma_5}_{AB}(i)$ on 2 gauge configurations with $Q = \pm 1$ from the finest ensemble. The quadrants of the plot show (from left to right, top to bottom) a scatter plot of $\zeta^{\gamma_5}_{AB}(i)$, then histograms of the imaginary part, real part and modulus of $\zeta^{\gamma_5}_{AB}(i)$. The diagonal overlaps are plotted in red and the others in black. In this plot, the off-diagonal points are plotted on top of the diagonal ones.

Figures 3.2, 3.3 and 3.4 show $\zeta^{\gamma_5}_{AB}(i)$ calculated on ensembles 5, 3 and 1 respectively, so with increasing lattice spacing. The upper left portion of the plots shows a scatter plot of $\zeta^{\gamma_5}_{AB}(i)$ in the complex plane. The diagonal overlaps $\zeta^{\gamma_5}_{AA}(i)$ are plotted in red and the off-diagonal ones are in black. The upper right part of the plots shows a histogram of the imaginary part of $\zeta^{\gamma_5}_{AB}(i)$, the lower left a histogram of the real part and the lower right section a histogram of the modulus of $\zeta^{\gamma_5}_{AB}(i)$. In all these histograms, the diagonal and off-diagonal $\zeta^{\gamma_5}_{AB}(i)$ are plotted separately with the diagonal in red and the off-diagonal in black. Note that the histograms are plotted with a logarithmic scale.

In these scatter plots, the red diagonal points are much larger in magnitude than the off-diagonal ones. Indeed, the red distributions extend well beyond the small region around zero plotted in the scatter plots. The size (real part, imaginary part and modulus) of the off-diagonal contributions can be seen to reduce as the lattice spacing is reduced.

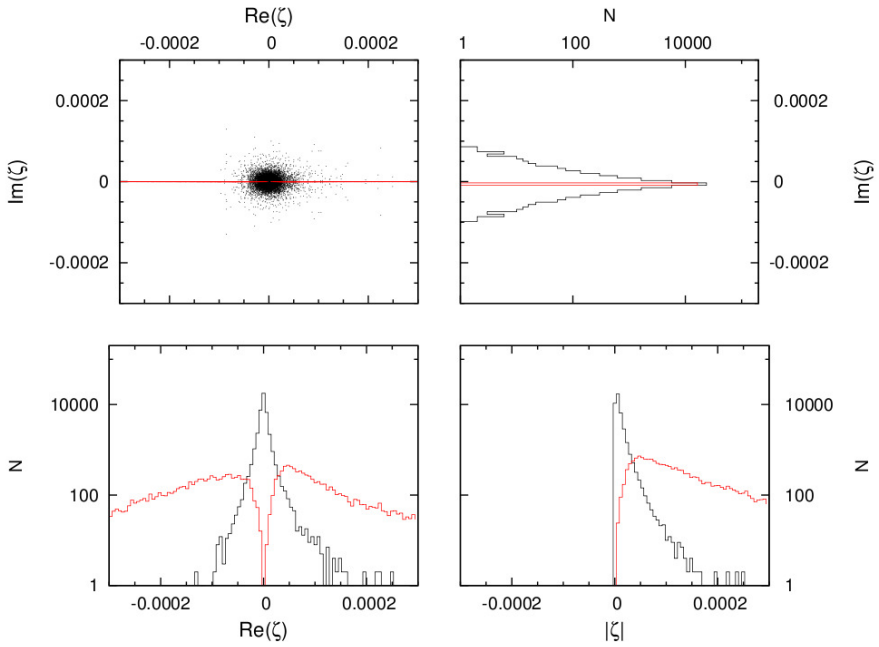

Figure 3.3: $\zeta^{\gamma_5}_{AB}(i)$ on 2 gauge configurations with $Q = \pm 1$ from ensemble 3, which has an intermediate lattice spacing and approximately the same physical volume as the finer and coarser ensembles. The quadrants of the plot show (from left to right, top to bottom) a scatter plot of $\zeta^{\gamma_5}_{AB}(i)$, then histograms of the imaginary part, real part and modulus of $\zeta^{\gamma_5}_{AB}(i)$. The diagonal overlaps are plotted in red and the others in black.

$\zeta^{\gamma_5}_{AB}(i)$ on different volumes

It is important to separate the effects of lattice spacing and number of lattice sites. The eigenvectors are normalised so that $\sum_i f^\dagger_A(i) f_A(i) = 1$, which means that

$$\sum_{1 \text{ hypercube}} f^\dagger_A(i) f_A(i) \simeq \frac{1}{N}, \tag{3.19}$$

where $N = \frac{L^4}{16}$ is the number of hypercubes on an L^4 lattice. This means that the off-diagonal $\zeta^{\gamma_5}_{AB}(i)$ can be expected to be smaller on the fine ensemble than the coarse simply due to the number of lattice sites.

This can be tested using ensembles 2 and 4, which both have the same lattice spacing as ensemble 3, but different volumes. Ensembles 1 and 2 have the same number of sites, as do ensembles 4 and 5.

Figures 3.5 and 3.6 show similar scatter plots and histogram as before for sample gauge configurations in ensembles 4 and 2 respectively. Figure 3.5 shows $\zeta^{\gamma_5}_{AB}(i)$ on configurations with a larger volume and can be compared to Figure 3.2, which shows results with the same number of lattice sites. A comparison can also be made between Figures 3.6 and 3.4 of $\zeta^{\gamma_5}_{AB}(i)$ on configurations with 12^4 lattice sites. These comparisons show that the off-diagonal $\zeta^{\gamma_5}_{AB}(i)$ are smaller on finer configurations.

Figure 3.7 compares the distributions of $|\zeta^{\gamma_5}_{AB}(i)|$ on ensembles 4 and 5 for the off-diagonal overlaps. The distribution for the finer ensemble 5 is shown in red and that

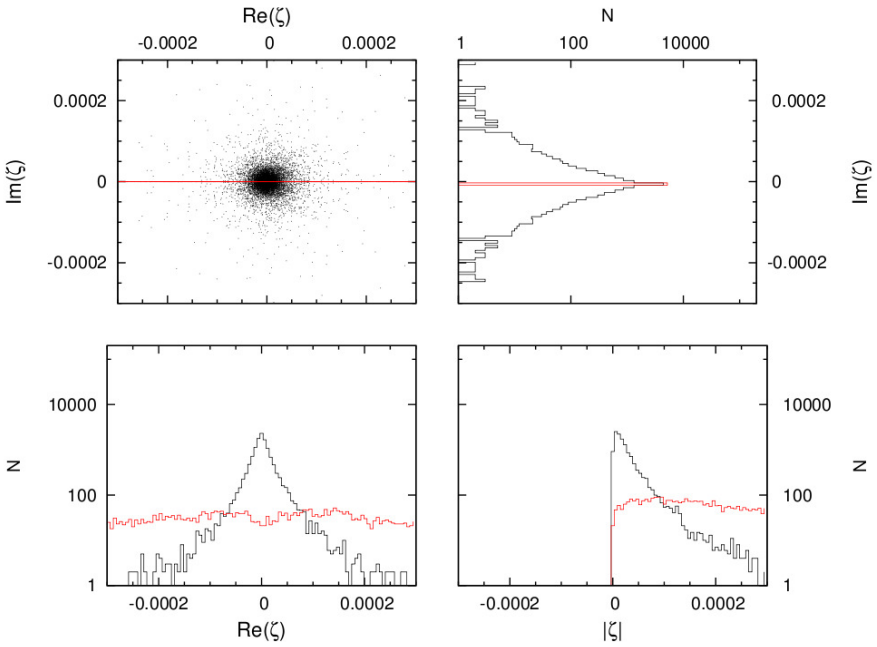

Figure 3.4: $\zeta^{\gamma_5}_{AB}(i)$ on 2 gauge configurations with $Q = \pm 1$ from the coarsest ensemble. The quadrants of the plot show (from left to right, top to bottom) a scatter plot of $\zeta^{\gamma_5}_{AB}(i)$, then histograms of the imaginary part, real part and modulus of $\zeta^{\gamma_5}_{AB}(i)$. The diagonal overlaps are plotted in red and the others in black.

for ensemble 4 in black. These are the same distributions as shown for the off-diagonal pieces in the lower right quadrants of Figures 3.2 and 3.5, but plotted together to compare the ensembles. Figure 3.7 shows a noticeably narrower distribution for the finer ensemble 5 than ensemble 4. This indicates that the off-diagonal $\zeta^{\gamma_5}_{AB}(i)$ become smaller as $a \to 0$, as already discussed.

Figures 3.8 shows a similar plot for the diagonal $|\zeta^{\gamma_5}_{AA}(i)|$. The distributions is a little broader on the fine ensemble, but the distributions are similar as the lattice size is the same.

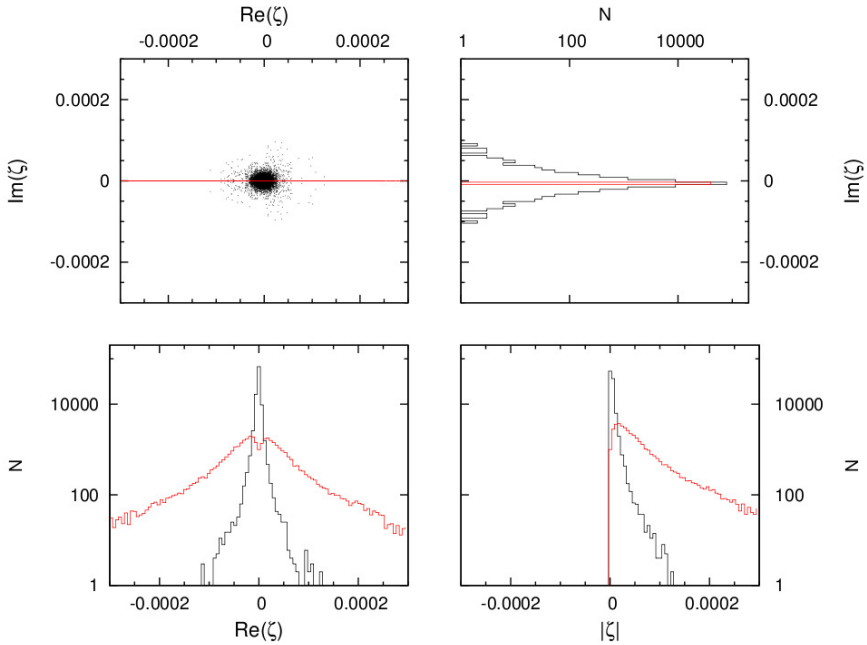

Figure 3.5: $\zeta^{\gamma_5}_{AB}(i)$ on 2 gauge configurations with $Q = \pm 1$ from ensemble 4, which has an intermediate lattice spacing and 20^4 lattice sites, which is the same number of sites as the finer ensemble 5. The quadrants of the plot show (from left to right, top to bottom) a scatter plot of $\zeta^{\gamma_5}_{AB}(i)$, then histograms of the imaginary part, real part and modulus of $\zeta^{\gamma_5}_{AB}(i)$. The diagonal overlaps are plotted in red and the others in black.

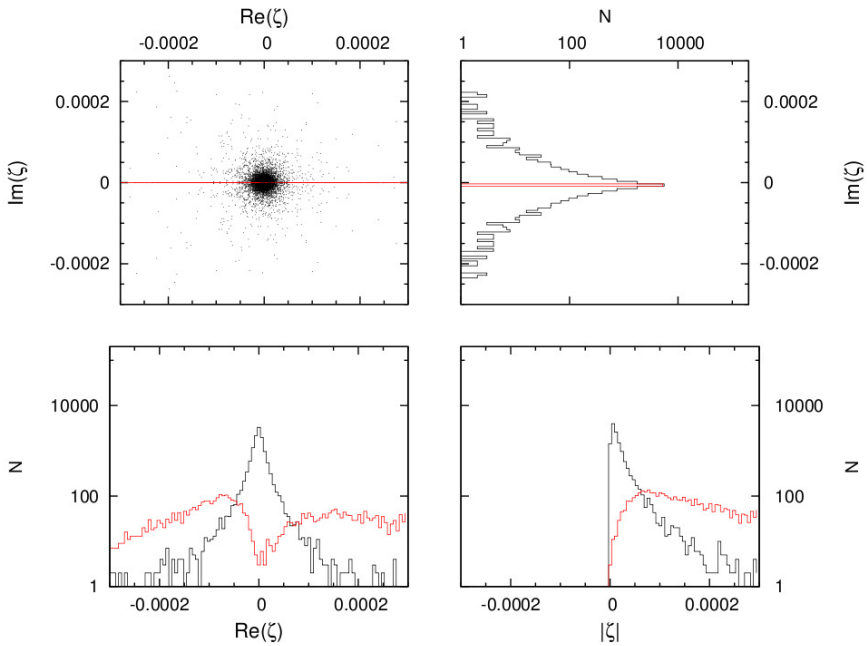

Figure 3.6: $\zeta^{\gamma_5}_{AB}(i)$ on 2 gauge configurations with $Q = \pm 1$ from ensemble 2, which has 12^4 lattice sites, the same as the coarsest ensemble 1, but with the same lattice spacing as ensemble 3. The quadrants of the plot show (from left to right, top to bottom) a scatter plot of $\zeta^{\gamma_5}_{AB}(i)$, then histograms of the imaginary part, real part and modulus of $\zeta^{\gamma_5}_{AB}(i)$. The diagonal overlaps are plotted in red and the others in black.

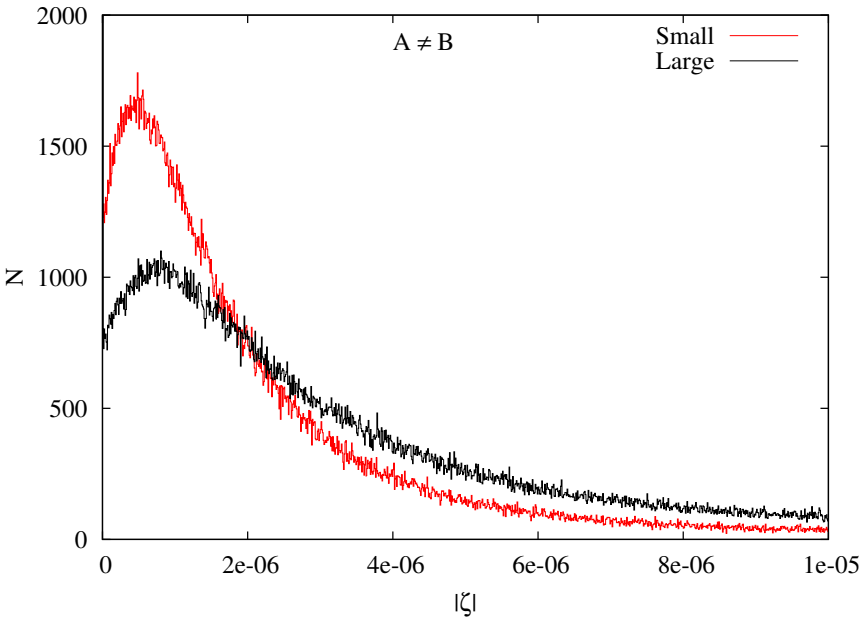

Figure 3.7: Histograms of off-diagonal $|\zeta^{\gamma_5}_{AB}(i)|$ $(A \neq B)$ plotted on ensembles 4 and 5, both of which have 20^4 lattice sites. The data for ensemble 4 (which has a larger physical volume) is plotted in black and the ensemble 5 (with finer lattice spacing) is in red.

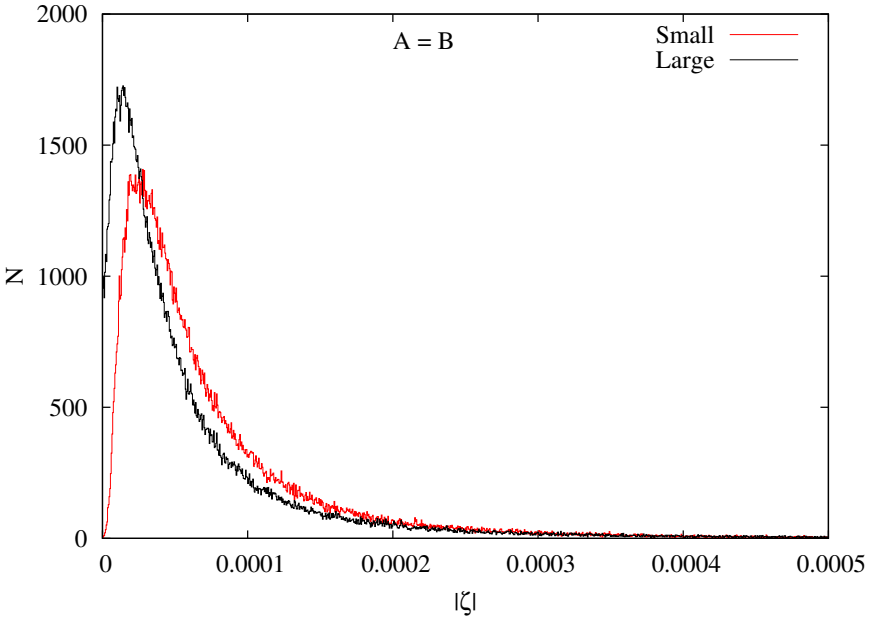

Figure 3.8: Histograms of $|\zeta^{\gamma_5}_{AA}(i)|$ plotted on ensembles 4 and 5, both of which have 20^4 lattice sites. The data for ensemble 4 (which has a larger physical volume) is plotted in black and the ensemble 5 (with finer lattice spacing) is in red.

3.2.2 Scalar

The taste-singlet scalar operator is local, so it easily follows that

$$\zeta^1_{AB}(i) = \sum_{\text{hypercube}} f^\dagger_A(i) f_B(i). \tag{3.20}$$

Once again, ζ^1_{AA} is real and positive with $\sum_{\text{All hypercubes}} \zeta^1_{AA}(i) = 1$. As in the pseudoscalar case, $\zeta^1_{A,-A}$ is also real, but can be positive or negative and is expected to be small compared to ζ^1_{AA}.

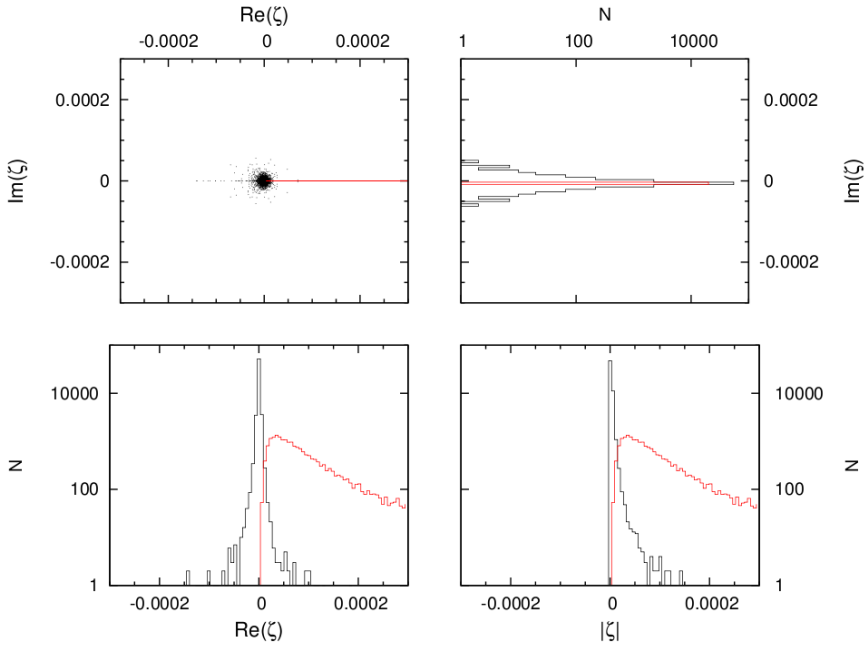

Figure 3.9: $\zeta^1_{AB}(i)$ on a single gauge configuration from the finest ensemble, ensemble 5. The quadrants of the plot show (from left to right, top to bottom) a scatter plot of $\zeta^1_{AB}(i)$, then histograms of the imaginary part, real part and modulus of $\zeta^1_{AB}(i)$. The diagonal overlaps are plotted in red and the others in black.

Scatter plots and histograms for the scalar operator on ensembles 5, 3 and 1 with similar physical volume but different lattice spacings are shown in Figures 3.9, 3.10 and 3.11 respectively. As with the scatter plots of the taste-singlet pseudoscalar operator, the diagonal terms are plotted in red and the off-diagonal in black. The scatter plots and histograms of the real and imaginary parts and modulus of $\zeta^1_{AB}(i)$ are plotted as for the pseudoscalar. In each of these figures, the diagonal terms are clearly large, positive and real, as expected from the normalisation of the eigenvectors. The purely real $\zeta^1_{A,-A}(i)$ terms can be seen in the scatter plots for those with negative values. The positive ones are obscured by the diagonal terms, but can be seen from the roughly symmetrical histogram of the real part of the off-diagonal terms in the lower left quadrant.

As was seen in the pseudoscalar case, the magnitude of the off-diagonal scalar overlaps decreases with lattice spacing. Figures 3.9, 3.10 and 3.11 plot $\zeta^1_{AB}(i)$ for only

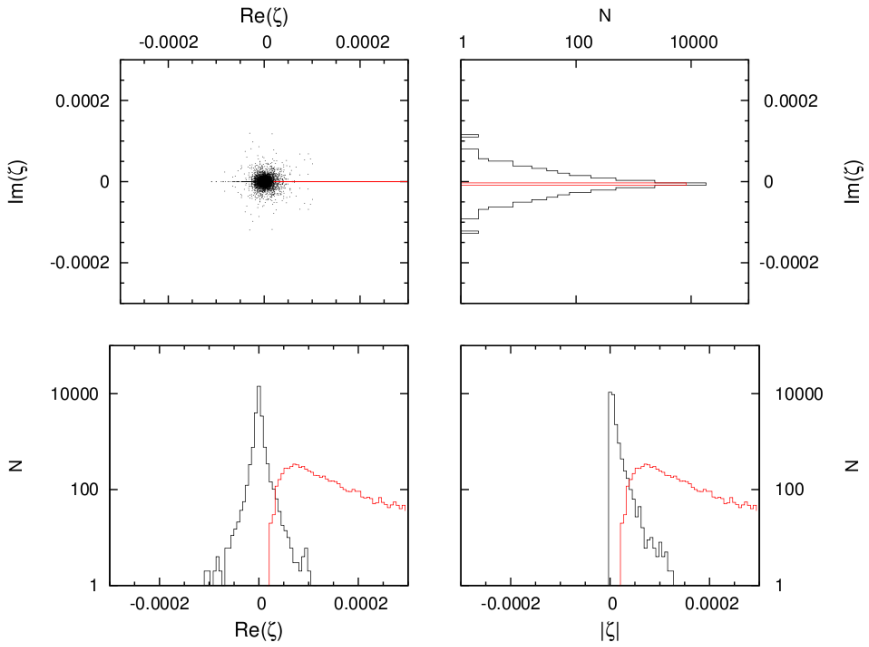

Figure 3.10: $\zeta^1_{AB}(i)$ on a single gauge configuration from ensemble 3 with intermediate lattice spacing and volume. This ensemble has the same physical volume as ensembles 1 and 5. The quadrants of the plot show (from left to right, top to bottom) a scatter plot of $\zeta^1_{AB}(i)$, then histograms of the imaginary part, real part and modulus of $\zeta^1_{AB}(i)$. The diagonal overlaps are plotted in red and the others in black.

one configuration, but the observed distributions are seen on other configurations as well.

$\zeta^1_{AB}(i)$ on different volumes

The effect of the number of lattice sites on the normalisation of the eigenvectors is relevant for the scalar operator too. In Figures 3.12 and 3.13, $\zeta^1_{AB}(i)$ is plotted for 1 configuration from the large and small ensembles 4 and 2 respectively.

As for the pseudoscalar case, comparison of Figures 3.12 and 3.9 shows that the magnitude of the off-diagonal $\zeta^1_{AB}(i)$ is smaller on the finer lattices, even with the same number of lattice sites.

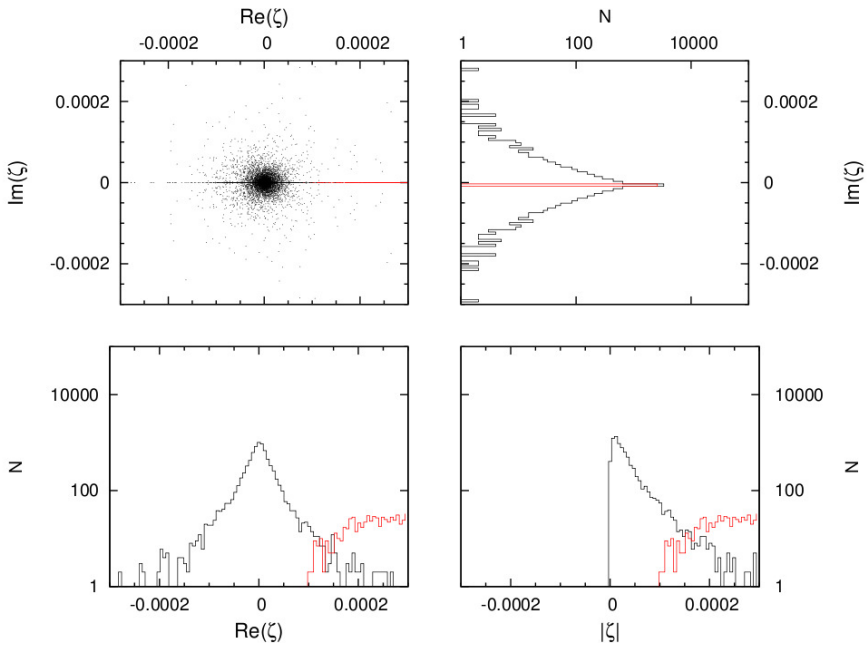

Figure 3.11: $\zeta^1_{AB}(i)$ on a single gauge configuration from the coarsest ensemble 1. The quadrants of the plot show (from left to right, top to bottom) a scatter plot of $\zeta^1_{AB}(i)$, then histograms of the imaginary part, real part and modulus of $\zeta^1_{AB}(i)$. The diagonal overlaps are plotted in red and the others in black.

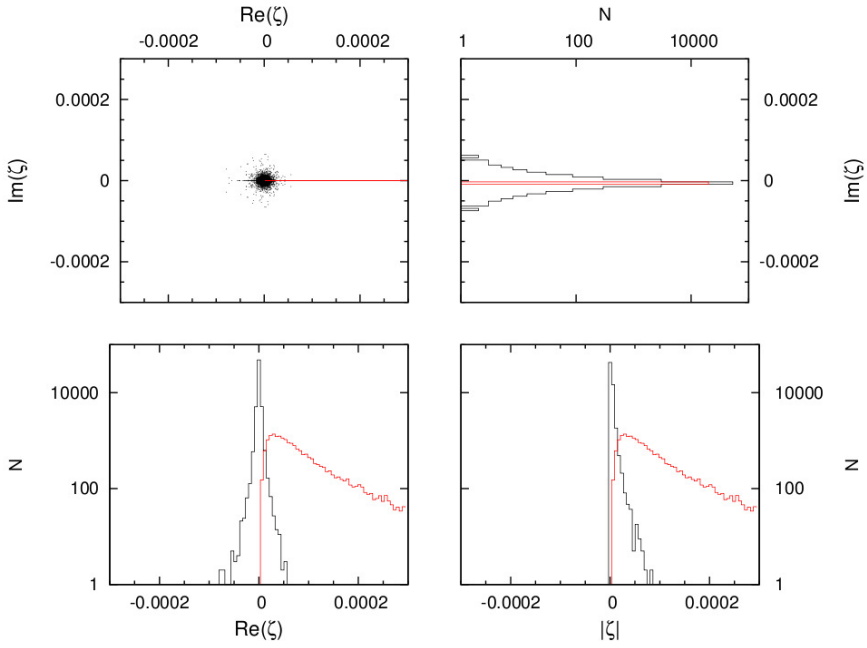

Figure 3.12: $\zeta^1_{AB}(i)$ on a single gauge configuration from ensemble 4. This ensemble has an intermediate lattice spacing and 20^4 lattice sites. The quadrants of the plot show (from left to right, top to bottom) a scatter plot of $\zeta^1_{AB}(i)$, then histograms of the imaginary part, real part and modulus of $\zeta^1_{AB}(i)$. The diagonal overlaps are plotted in red and the others in black.

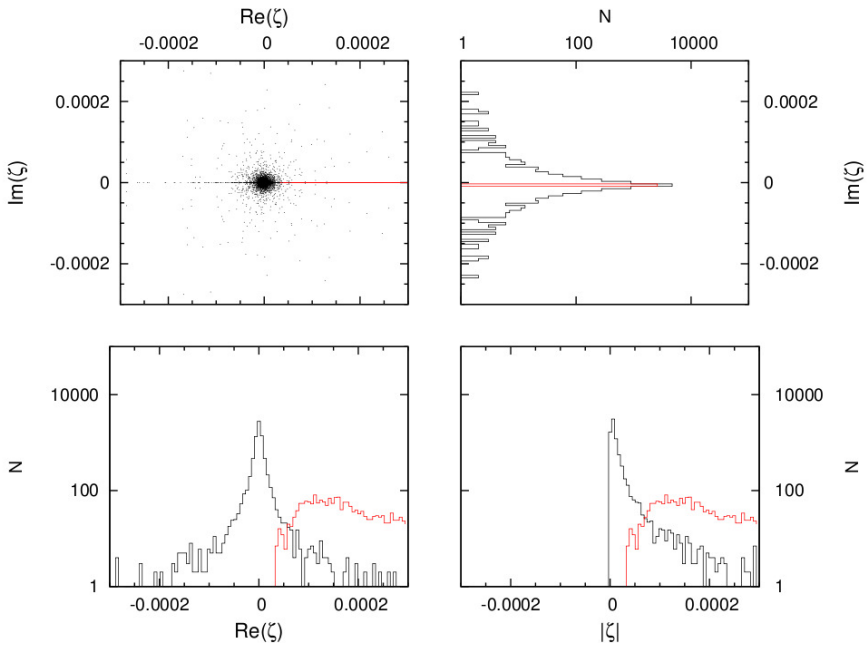

Figure 3.13: $\zeta^1_{AB}(i)$ on a single gauge configuration from ensemble 2, the smallest ensemble with intermediate lattice spacing and 12^4 sites. The quadrants of the plot show (from left to right, top to bottom) a scatter plot of $\zeta^1_{AB}(i)$, then histograms of the imaginary part, real part and modulus of $\zeta^1_{AB}(i)$. The diagonal overlaps are plotted in red and the others in black.

3.2.3 Vector

For the vector operator, the continuum behaviour is different. In the continuum, the zero modes do not interact with a vector operator because the zero modes satisfy $\phi_0(x) = \pm\gamma_5\phi_0(x)$ and γ_5 anticommutes with γ_μ, so

$$\phi_0(x)^\dagger\gamma_\mu\phi_0(x) = \phi_0(x)^\dagger\gamma_5\gamma_\mu\gamma_5\phi_0(x) = -\phi_0(x)^\dagger\gamma_\mu\phi_0(x) = 0. \tag{3.21}$$

To reproduce this on the lattice, all $\zeta^{\gamma_\mu}_{AB}(i)$ must vanish as $a \to 0$, even the diagonal $\zeta^{\gamma_\mu}_{AA}(i)$. The taste-singlet vector operator $\gamma_\mu \otimes 1$ is a 1-link operator

$$\bar{\psi}(i)\gamma_\mu\psi(i+\hat{\mu}). \tag{3.22}$$

Applying the staggering transformation, it is equal to

$$(-1)^{i^<_\mu}\bar{\chi}(i)\chi(i+\hat{\mu}). \tag{3.23}$$

Therefore $\zeta^{\gamma_\mu}_{AB}(i)$ is defined as

$$\sum_{\text{hypercube}} \zeta^{\gamma_\mu}_{AB}(i) = (\sqrt{-1})(-1)^{i^<_\mu} f_A(i)^\dagger f_B(i+\hat{\mu}). \tag{3.24}$$

The factor of $\sqrt{-1}$ (written like this to avoid confusion with lattice site i) in the definition means that the diagonal terms $\zeta^{\gamma_\mu}_{AA}(i)$ are purely imaginary. As the phase factor $\varepsilon(i)$ used to reconstruct the mirror eigenvectors changes sign for 1 link translations on the lattice ($\varepsilon(i) = -\varepsilon(i+\hat{\mu})$), the eigenvector overlaps between modes and their mirrors, $\zeta^{\gamma_\mu}_{A,-A}(i)$, is real. The other $\zeta^{\gamma_\mu}_{AB}(i)$ with $|A| \neq |B|$ are complex.

$\zeta^{\gamma_\mu}_{AB}(i)$ on one $|Q| = 1$ configuration from ensemble 5, the finest ensemble, is plotted in Figure 3.14. Once again, the quadrants show a scatter plot of $\zeta^{\gamma_\mu}_{AB}(i)$ and log-scale histograms of the real part, imaginary part and modulus of $\zeta^{\gamma_\mu}_{AB}(i)$. The different combinations of eigenvectors obey different properties; the diagonal $\zeta^{\gamma_\mu}_{AA}(i)$ are plotted in red and lie on the imaginary axis, as expected. The $\zeta^{\gamma_\mu}_{A,-A}(i)$ are in blue along the real axis and the rest are plotted in black. Figures 3.15 and 3.16 show the data for $\zeta^{\gamma_\mu}_{AB}(i)$ from configurations on ensembles 3 and 1, with coarser lattice spacings. The magnitude of $\zeta^{\gamma_\mu}_{AB}(i)$, whether $A = B$, $A = -B$ or $|A| \neq |B|$, decreases with the lattice spacing. Whilst some overlaps are purely real or imaginary, the modulus of all the contributions is seen to follow the same distribution on each ensemble.

$\zeta^{\gamma_\mu}_{AB}(i)$ on different volumes

As a check, $\zeta^{\gamma_\mu}_{AB}(i)$ were also calculated and studied on the intermediate ensembles with larger and smaller lattice sizes. Figure 3.17, which shows $\zeta^{\gamma_\mu}_{AB}(i)$ for a configuration on ensemble 4, which can be compared to Figure 3.14, which is for a configuration with the same number of lattice sites but finer lattice spacing. Figure 3.18 shows similar

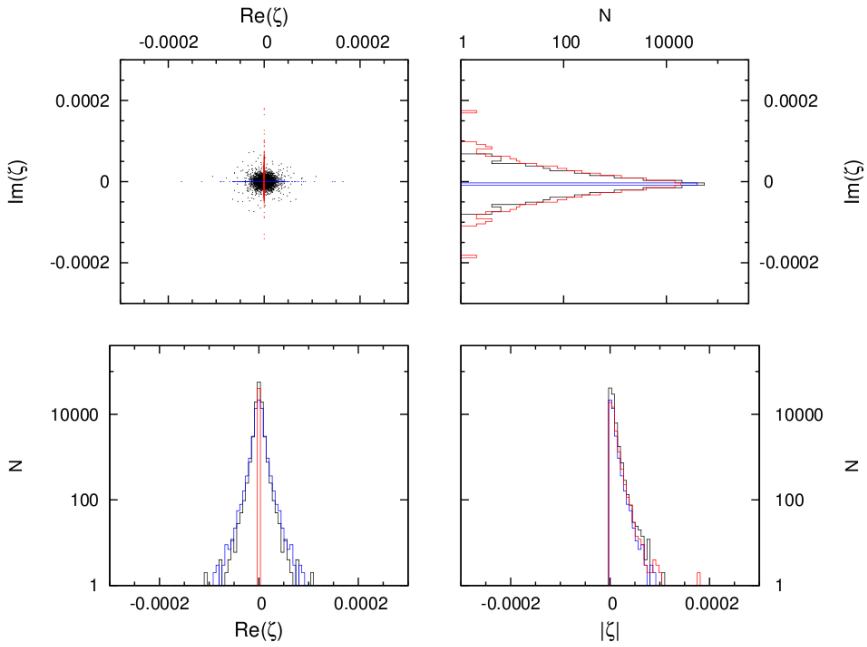

Figure 3.14: $\zeta^{\gamma_\mu}_{AB}(i)$ on a single gauge configuration from the finest ensemble, ensemble 5. The quadrants of the plot show (from left to right, top to bottom) a scatter plot of $\zeta^{\gamma_\mu}_{AB}(i)$, then histograms of the imaginary part, real part and modulus of $\zeta^{\gamma_\mu}_{AB}(i)$. The diagonal $\zeta^{\gamma_\mu}_{AA}(i)$ are plotted in red, the $\zeta^{\gamma_\mu}_{AB}(i)$ with $A = -B$ are in blue and $|A| \neq |B|$ in black.

data for a configuration from ensemble 2 and can be compared to Figure 3.16.

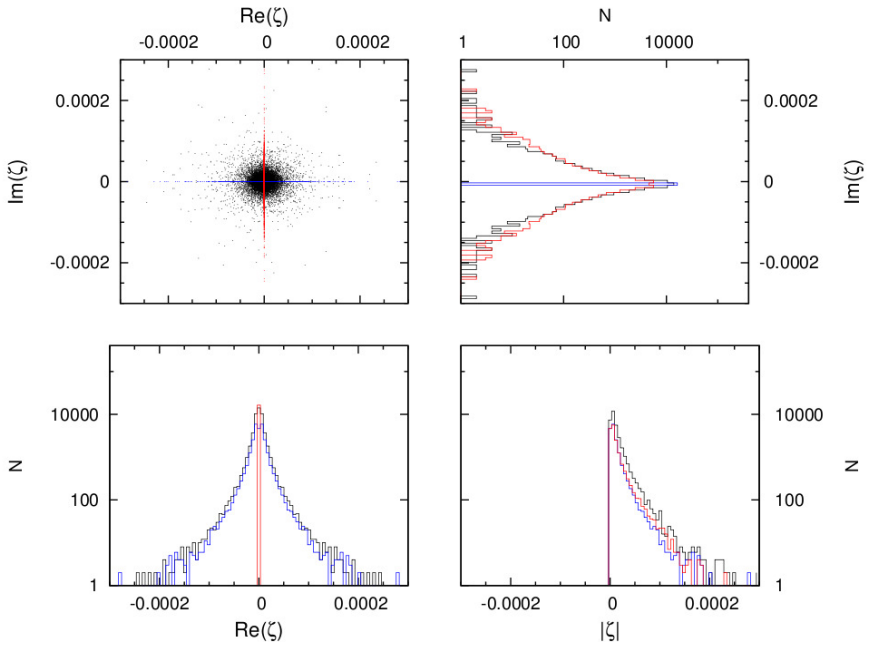

Figure 3.15: $\zeta^{\gamma_\mu}_{AB}(i)$ on a single gauge configuration from ensemble 3, with intermediate lattice spacing. The quadrants of the plot show (from left to right, top to bottom) a scatter plot of $\zeta^{\gamma_\mu}_{AB}(i)$, then histograms of the imaginary part, real part and modulus of $\zeta^{\gamma_\mu}_{AB}(i)$. The diagonal $\zeta^{\gamma_\mu}_{AA}(i)$ are plotted in red, the $\zeta^{\gamma_\mu}_{AB}(i)$ with $A = -B$ are in blue and $|A| \neq |B|$ in black.

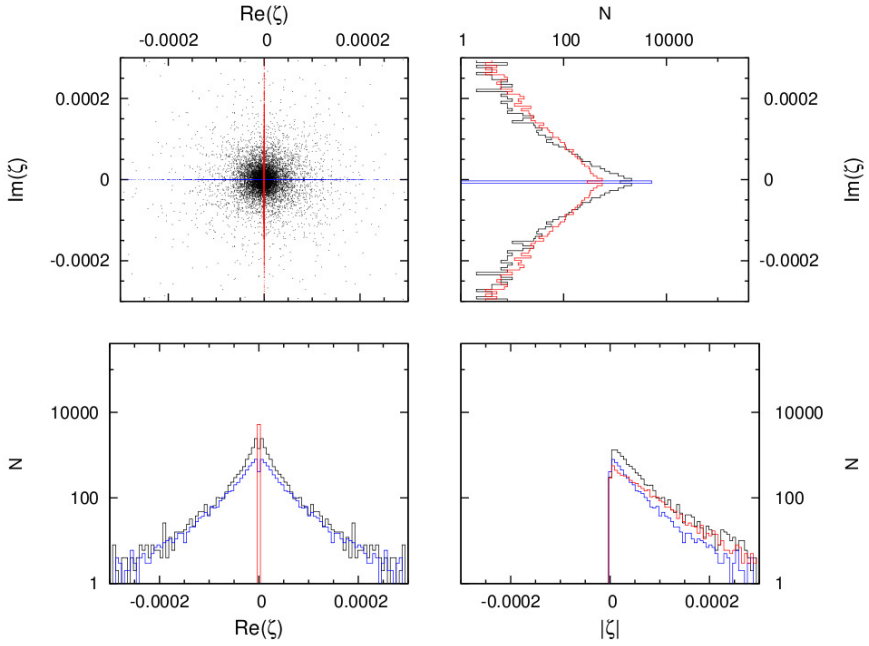

Figure 3.16: $\zeta^{\gamma_\mu}_{AB}(i)$ on a single gauge configuration from the coarse ensemble, ensemble 1. The quadrants of the plot show (from left to right, top to bottom) a scatter plot of $\zeta^{\gamma_\mu}_{AB}(i)$, then histograms of the imaginary part, real part and modulus of $\zeta^{\gamma_\mu}_{AB}(i)$. The diagonal $\zeta^{\gamma_\mu}_{AA}(i)$ are plotted in red, the $\zeta^{\gamma_\mu}_{AB}(i)$ with $A = -B$ are in blue and $|A| \neq |B|$ in black.

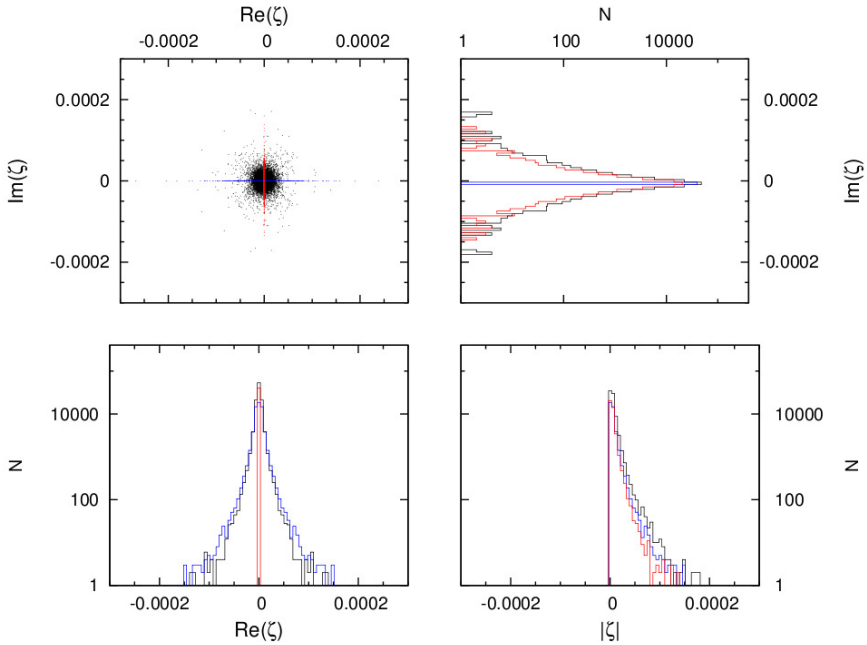

Figure 3.17: $\zeta^{\gamma_\mu}_{AB}(i)$ on a single gauge configuration from the ensemble 4, which has intermediate lattice spacing and a larger volume. The quadrants of the plot show (from left to right, top to bottom) a scatter plot of $\zeta^{\gamma_\mu}_{AB}(i)$, then histograms of the imaginary part, real part and modulus of $\zeta^{\gamma_\mu}_{AB}(i)$. The diagonal $\zeta^{\gamma_\mu}_{AA}(i)$ are plotted in red, the $\zeta^{\gamma_\mu}_{AB}(i)$ with $A = -B$ are in blue and $|A| \neq |B|$ in black.

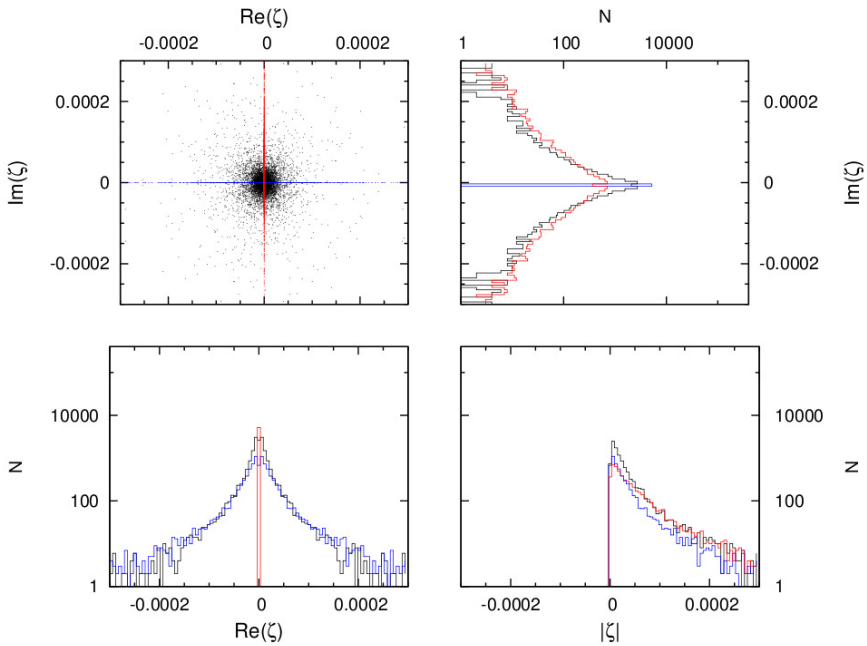

Figure 3.18: $\zeta^{\gamma_\mu}_{AB}(i)$ on a single gauge configuration from ensemble 2 with a smaller volume of 12^4 lattice sites and an intermediate lattice spacing. The quadrants of the plot show (from left to right, top to bottom) a scatter plot of $\zeta^{\gamma_\mu}_{AB}(i)$, then histograms of the imaginary part, real part and modulus of $\zeta^{\gamma_\mu}_{AB}(i)$. The diagonal $\zeta^{\gamma_\mu}_{AA}(i)$ are plotted in red, the $\zeta^{\gamma_\mu}_{AB}(i)$ with $A = -B$ are in blue and $|A| \neq |B|$ in black.

3.2.4 Scaling with volume and lattice spacing

The observed trend that the off-diagonal components of $\zeta^{\Gamma}_{AB}(i)$ vanish in the continuum limit can be quantified by looking at the width of the distribution of $|\zeta^{\Gamma}_{AB}(i)|$ as a function of lattice spacing, a. The width of a distribution, $W(\zeta^{\Gamma}_{AB}(i))$, is defined such that 66% of the data for $|\zeta^{\Gamma}_{AB}(i)|$ lie in between zero and $W(\zeta^{\Gamma}_{AB}(i))$. The widths are calculated for 10 sample gauge configurations with $|Q| = 1$, rather than just the one or two plotted and the error is estimated by comparing the widths obtained from subsets of only five configurations.

The widths for the distributions of the plotted eigenvector overlaps – that is the diagonal and off-diagonal for the scalar and pseudoscalar operators are shown in Table 3.2. The widths for the diagonal and separated $A = -B$ and $|A| \neq |B|$ off-diagonal contributions for the vector are shown in Table 3.3.

In Figure 3.19, the ratio of distribution widths is plotted against a for the scalar and pseudoscalar operator. The widths at each lattice spacing depend on the number of lattice sites, because the eigenvectors are normalised so that $\sum_i f^{\dagger}_A(i) f_A(i) = 1$. To account for the normalisation and compare off-diagonal widths on different lattice spacings, the off-diagonal scalar and pseudoscalar widths are divided by the corresponding diagonal widths. The pseudoscalar is plotted in blue and the scalar in red. The dashed lines show fits to the data as a polynomial in a^2, which are consistent with zero at $a = 0$ for both operators.

Figure 3.20 shows the various vector widths. None of the eigenvector overlaps is expected to be large, so they are all normalised by the diagonal pseudoscalar width. The diagonal distribution width is plotted in black, the $A = -B$ in red and the $|A| \neq |B|$ in blue. Again the simple fits to the data are consistent with zero at $a = 0$.

	γ_5		1	
Ens.	$A = B$	$A \neq B$	$A = B$	$A \neq B$
1	3.93(31)	0.296(26)	6.84(17)	0.285(23)
2	4.08(56)	0.180(11)	6.07(70)	0.158(9)
3	1.49(3)	0.0635(38)	2.15(6)	0.0566(27)
4	0.548(26)	0.0390(16)	0.846(29)	0.0406(22)
5	0.716(14)	0.0230(7)	0.954(16)	0.0199(5)

Table 3.2: Widths (multiplied by 10^4) of the distributions of $|\zeta^{\Gamma}_{AB}|$ histograms for 10 $|Q| = 1$ gauge configurations taken from each ensemble. The widths and an estimate of the error is given for the plotted eigenvector overlaps for the pseudoscalar and scalar.

Ens.	$A = B$	$A = -B$	$\lvert A\rvert \neq \lvert B\rvert$
1	0.242(11)	0.202(21)	0.224(1)
2	0.188(23)	0.146(12)	0.155(16)
3	0.0567(36)	0.0541(42)	0.0561(22)
4	0.0242(10)	0.0246(17)	0.0258(4)
5	0.0211(2)	0.0206(2)	0.0219(5)

Table 3.3: Widths (multiplied by 10^4) of the distributions of $|\zeta^{\gamma_\mu}_{AB}|$ histograms for 10 $|Q| = 1$ gauge configurations taken from each ensemble. The widths and an estimate of the error is given for the plotted eigenvector overlaps for the vector operator.

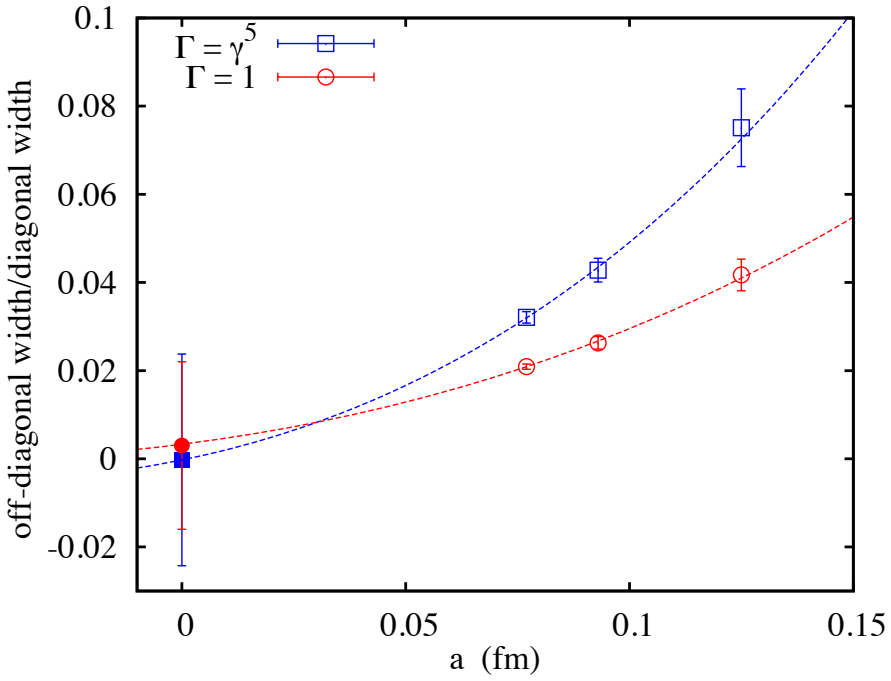

Figure 3.19: Ratio of the off-diagonal to diagonal widths of the $\zeta^{\gamma_5}_{AB}(i)$ and $\zeta^{1}_{AB}(i)$ distributions, as a function of lattice spacing. The pseudoscalar is plotted with blue squares and the scalar with red circles. Dashed lines are simple fits to the data as a polynomial in a^2 and the solid points are at $a = 0$.

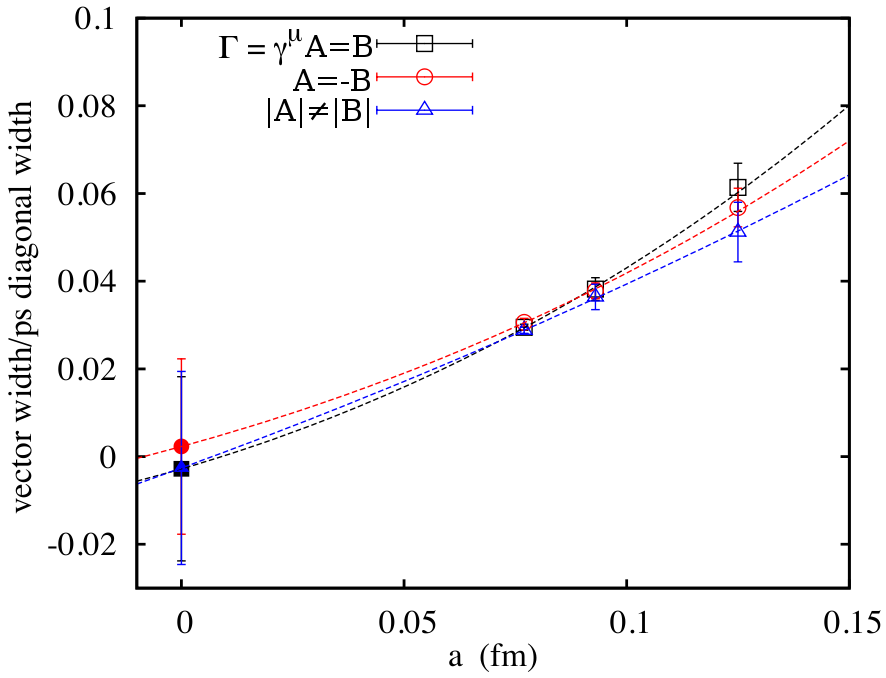

Figure 3.20: The widths of the distributions of $|\zeta^{\gamma_\mu}_{AB}(i)|$, normalised using the diagonal pseudoscalar widths. The diagonal $A = B$ is plotted in black, $A = -B$ in red and $|A| \neq |B|$ in blue. Dashed lines are simple fits to the data as a polynomial in a^2 and the solid points are at $a = 0$.

3.3 Zero mode contributions to correlators

The contributions of the near-zero modes to correlation functions will be considered in this section. The $\zeta^{\Gamma}_{AB}(i)$ considered in the previous section were summed over a hypercube, but correlation functions for flavour-singlet mesons describe the mesons propagating from one timeslice to another. The eigenvector overlaps for a timeslice are defined as

$$\tilde{\zeta}^{\Gamma}_{AB}(t) = \sum_{\vec{i}} f_A(i)\Gamma f_B(i'), \tag{3.25}$$

where now the sum is over all i on a timeslice t. Point-split operators are averaged over all sites i' suitably separated in either the forward or backward direction and not restricted to being in the same 2^4 hypercube as i. For operators (like the taste-singlet pseudoscalar operator) which include a time-like gauge link, the site i is on timeslice t and the point-split site i' averaged over those on timeslices $t \pm 1$.

Combinations of the eigenvector overlaps $\tilde{\zeta}^{\Gamma}_{AB}(t)$ that appear in the connected and disconnected parts of the correlator respectively are defined as:

$$X^{\Gamma}_{AB}(T) = \sum_{t} \tilde{\zeta}^{\Gamma}_{AB}(t)\tilde{\zeta}^{\Gamma}_{BA}(t+T), \tag{3.26}$$

$$Y^{\Gamma}_{AB}(T) = \sum_{t} \tilde{\zeta}^{\Gamma}_{AA}(t)\tilde{\zeta}^{\Gamma}_{BB}(t+T). \tag{3.27}$$

From the definitions, it follows that $X^{\Gamma}_{AA}(T) = Y^{\Gamma}_{AA}(T)$. In this section, the eigenmodes studied, A and B, are no longer restricted to the near-zero modes; the correlator contributions involving non-zero modes will also be examined.

Comparing to Equations 3.4 and 3.6 for the connected and disconnected correlator contribution, shows that $X^{\Gamma}_{AB}(T)$ are the eigenvector combinations in the connected piece and $Y^{\Gamma}_{AB}(T)$ the eigenvector combinations in the disconnected piece. The connected correlator as a function of T is $C(T) = \sum_{i,j} C(i,j)$ with sites i and j at times i_t and j_t satisfying $|j_t - i_t| = T$. Then

$$C^{\Gamma}(T) = \sum_{AB} \frac{X^{\Gamma}_{AB}(T)}{(i\lambda_A + m)(i\lambda_B + m)}. \tag{3.28}$$

Similarly, the disconnected correlator is made from $Y^{\Gamma}_{AB}(T)$ and the corresponding eigenvalues λ_A and λ_B:

$$D^{\Gamma}(T) = \sum_{AB} \frac{Y^{\Gamma}_{AB}(T)}{(i\lambda_A + m)(i\lambda_B + m)}. \tag{3.29}$$

In the chiral limit $m \to 0$, the potentially divergent near-zero modes arising in $C(T)$ and $D(T)$ are expected to cancel as they are combining to make the total correlator

$$T(T) = -\frac{1}{4}C(T) + \frac{1}{16}D(T). \tag{3.30}$$

The contributions to the correlators are averaged over all gauge configurations in each ensemble with the same $|Q|$. The different $|Q|$ sectors have to be separated to deal with the number of near-zero modes in each, whose behaviour is being studied. The focus is once again on $|Q| = 1$ and the number of such configurations in each ensemble is listed in Table 3.1.1.

3.3.1 Pseudoscalar

In the continuum, large contributions come from combinations of modes with

$$\sum_x \phi_A^\dagger(x)\phi_B(x) \neq 0. \tag{3.31}$$

For the pseudoscalar, these are easy to identify (and here the continuum modes are assumed to be normalised to 1). The zero modes satisfy

$$\sum_x \phi_0^\dagger(x)\gamma_5\phi_0(x) = \chi_0 = \pm 1, \tag{3.32}$$

so they will give a large contribution. The non-zero modes contribute only in partnership with their mirror modes $\phi_{-A} = \gamma_5\phi_A$ as

$$\sum_x \phi_A^\dagger(x)\gamma_5\phi_{-A}(x) = \sum_x \phi_A^\dagger(x)(\gamma_5)^2\phi_A(x) = 1. \tag{3.33}$$

These combinations only appear in the connected correlator.

With staggered fermions, each continuum mode, $\phi_A(x)$, is replaced by a quartet of lattice modes, $f_A(i)$. To reproduce continuum QCD, the lattice modes must combine to mimic the continuum behaviour.

Figure 3.21 shows the behaviour of $X_{AB}^{\gamma_5}(T)$ for the near-zero mode quartet, $A, B = \pm 1, \pm 2$ on ensemble 5. This ensemble is the ensemble with the finest lattice spacing. The modes $A = 1, 2$ are the modes with positive near-zero eigenvalue and $A = -1, -2$ are their corresponding mirror eigenmodes. In Figure 3.21, the overlaps $X_{11}^{\gamma_5}(T)$ and $X_{22}^{\gamma_5}(T)$ are large and equal. The sum over all T of $X_{AA}^{\gamma_5}(T)$ is χ_A^2. Contributions $X_{AB}^{\gamma_5}(T)$ are related to the mirror mode contributions by

$$X_{AB}^{\gamma_5}(T) = X_{-A,-B}^{\gamma_5}(T). \tag{3.34}$$

It follows that there are four large contributions to the connected correlator, $X_{AA}^{\gamma_5}(T)$, from each of the quartet of near-zero modes. Some of the cross terms $X_{AB}^{\gamma_5}(T)$ with $A \neq B$ are also plotted in Figure 3.21. Both the overlap between the two positive modes, $X_{12}^{\gamma_5}(T)$, and between a mode and its mirror, $X_{1,-1}^{\gamma_5}(T)$, are zero. This shows that there is no contribution from the cross terms to $X_{AB}^{\gamma_5}(T)$; all of the contributions to the connected correlator come from the diagonal pieces.

Figure 3.22 shows the same combinations of $X_{AB}^{\gamma_5}(T)$ as Figure 3.21 but for the

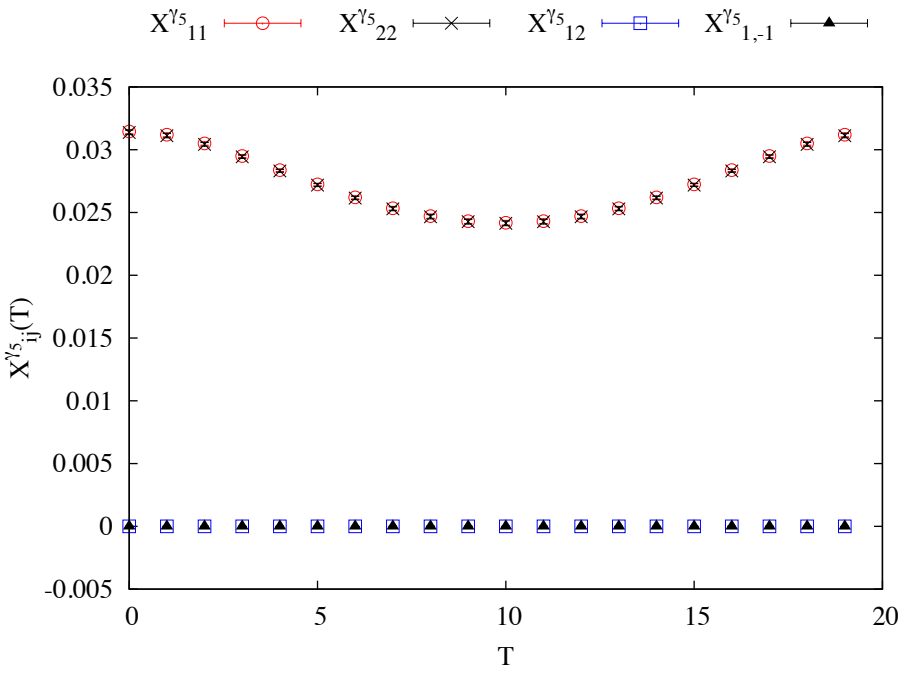

Figure 3.21: Average over the $|Q| = 1$ configurations from ensemble 5 of the connected pseudoscalar contributions $X^{\gamma_5}_{11}(T)$ (red circles), $X^{\gamma_5}_{22}(T)$ (black crosses), $X^{\gamma_5}_{12}(T)$ (blue squares) and $X^{\gamma_5}_{1,-1}(T)$ (filled black triangles).

coarser ensemble 1. Now the range of T only goes up to 12 rather than 20, but the picture is the same on all the ensembles.

The contributions to the disconnected correlator from modes 1 and 3 (a near-zero mode and a non-zero mode) are shown in Figure 3.23. The behaviour of these overlaps is easy to understand. From the definitions, it is clear that

$$X^{\gamma_5}_{AB}(T) = Y^{\gamma_5}_{AB}(T), \tag{3.35}$$

as can be seen for the specific plotted example of $Y^{\gamma_5}_{11}(T)$. Furthermore, the disconnected correlator contributions $Y^{\gamma_5}_{AB}(T)$ all satisfy

$$\sum_T Y^{\gamma_5}_{AB}(T) = \chi_A \chi_B. \tag{3.36}$$

Because all the eigenvectors in the near-zero quartet have the same chirality, it follows that all the contributions $Y^{\gamma_5}_{AB}(T)$ where $A, B = \pm 1, \pm 2$ look the same.

Figure 3.23 also shows the disconnected eigenvector contributions from pairs of mode involving mode 3, the lowest lying non-zero eigenmode on the $|Q| = 1$ configurations. This mode is in a different quartet to the near-zero modes and has chirality $\chi_3 \simeq 0$. It is not then a surprise to see that $Y^{\gamma_5}_{AB}(T)$ is close to zero for $B = 3$ because

$$\sum_T Y^{\gamma_5}_{A3}(T) = \chi_A \chi_3 \to 0 \tag{3.37}$$

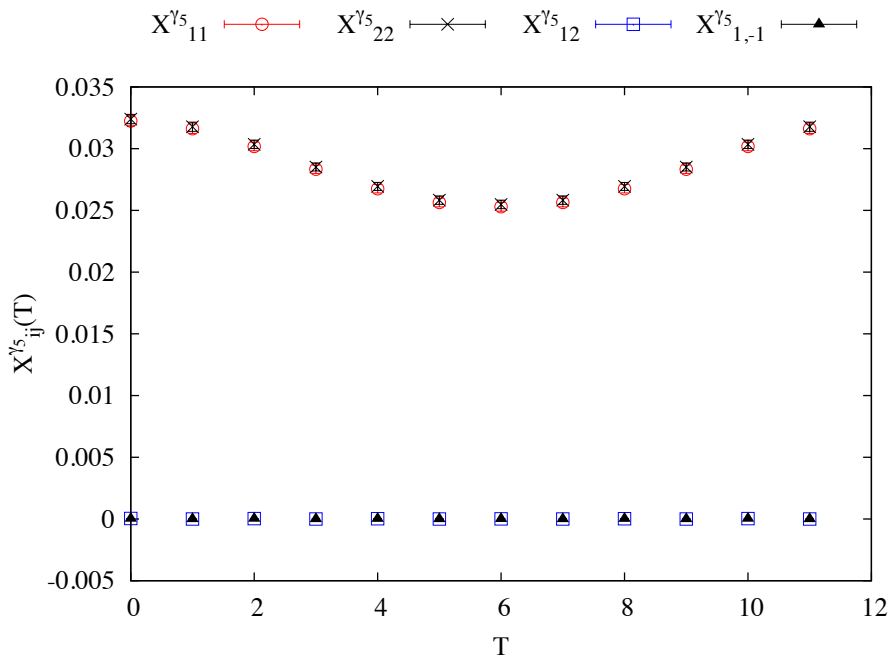

Figure 3.22: Average over the $|Q| = 1$ configurations from ensemble 1 of the connected pseudoscalar contributions $X_{11}^{\gamma_5}(T)$ (red circles), $X_{22}^{\gamma_5}(T)$ (black crosses), $X_{12}^{\gamma_5}(T)$ (blue squares) and $X_{1,-1}^{\gamma_5}(T)$ (filled black triangles). This is from the coarsest ensemble, so the range of T is only up to 12.

in the continuum limit.

This is shown in Figure 3.24, which plots the ensemble average of $\sum_T Y_{13}^{\gamma_5}(T)$ against a^2 for ensembles 1,3 and 5 with approximately equal physical lattice size. It shows that this combination, proportional to χ_3, does indeed vanish with a^2.

In Figure 3.25, the contribution to the connected correlator coming from modes 1 and 3 is plotted. The overlap $X_{13}^{\gamma_5}(T)$ is the mixing between one of the near-zero mode quartet and one of the lowest non-zero quartet. In the continuum, there would only be 1 zero mode and it would be orthogonal to the non-zero mode. Eigenvector 1 is a representative of the quartet of lattice modes corresponding to the single continuum zero mode and eigenvector 3 a representative of the orthogonal non-zero mode quartet, so it is expected that their overlap on the lattice should be zero. Figure 3.25 clearly shows that there is no contribution from $X_{13}^{\gamma_5}(T)$.

The quartet corresponding to a continuum non-zero mode are expected to behaviour differently to the near-zero quartet. This is because, unlike the zero modes, the continuum non-zero modes satisfy $\sum_x \phi_A^\dagger(x)\gamma_5\phi_A(x) = 0$. On the lattice, this translates to the expectation that $X_{AB}^{\gamma_5}(T)$ will not contribute for A, B in the same non-zero quartet. Figure 3.26 shows the overlaps between modes 3 and 4, both from the first non-zero quartet. It shows that the overlaps between these modes do not give an important contribution to the connected pseudoscalar correlator.

In the continuum, the non-zero modes contribute to the pseudoscalar correlator in partnership with their mirror modes. Figure 3.27 shows the connected overlaps

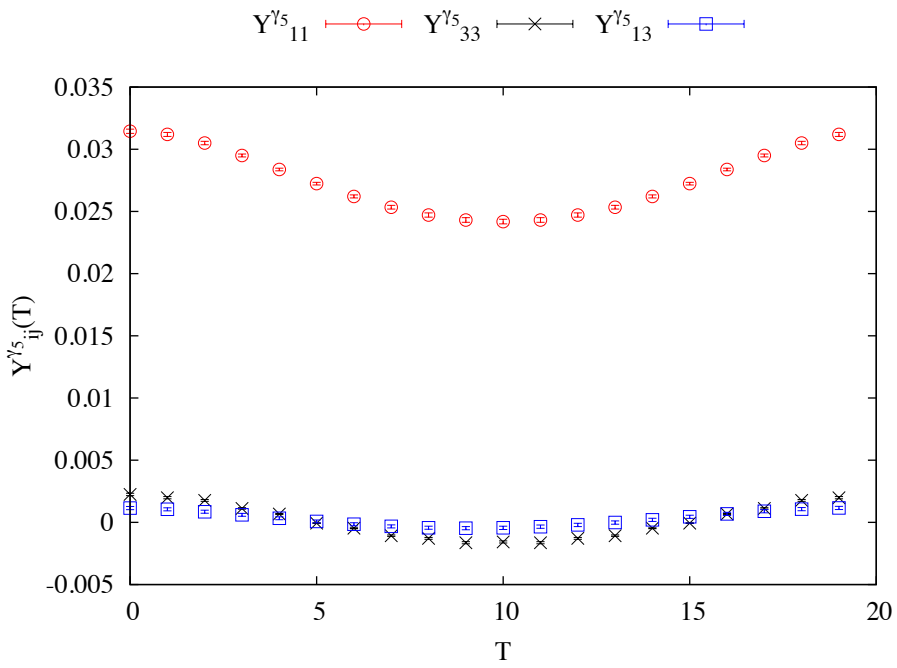

Figure 3.23: Average over the $|Q| = 1$ configurations from ensemble 5 of the disconnected pseudoscalar contributions $Y_{11}^{\gamma_5}(T)$ (red circles), $Y_{33}^{\gamma_5}(T)$ (black crosses) and $Y_{13}^{\gamma_5}(T)$ (blue squares).

between non-zero mode 3 and the quartet of modes -3 to -6. It shows significant contributions from the combinations $X_{3,-5}^{\gamma_5}(T)$ and $X_{3,-6}^{\gamma_5}(T)$, each about half the size of $X_{11}^{\gamma_5}(T)$. Indeed, the numerical results also show that mode 4 has a significant overlap with modes -5 and -6 and that modes 5 and 6 with modes -3 and -4 in the mirror quartet. In this way, it is seen that the quartet reproduce the expected continuum behaviour.

Figure 3.28 shows the same pattern as was seen for the 1st quartet of positive non-zero modes and their mirror quartet repeated for the 2nd quartet – modes 7,8,9 and 10. Again, the total contributions from all the modes agrees with the continuum behaviour.

Whilst it is interesting to see that the non-zero lattice modes also behave in an analogous way to the continuum modes, the most important result is the disappearance of potential divergent contributions coming from the near-zero modes in the chiral limit. Analysis of the eigenvector contributions to the connected correlator shows 4 large contributions coming from the near-zero modes. Similar analysis of the disconnected correlator reveals 16 such contributions. When the two are combined according to Equation 3.7, these should cancel out.

To demonstrate this cancellation, Figure 3.29 shows histograms of the value of

$$\sum_{AB} -\frac{X_{AB}^{\gamma_5}(T)}{4} + \frac{X_{AB}^{\gamma_5}(T)}{16} \tag{3.38}$$

at the midpoint of the lattice $T = T_{mid}$ calculated on each $|Q| = 1$ configuration from

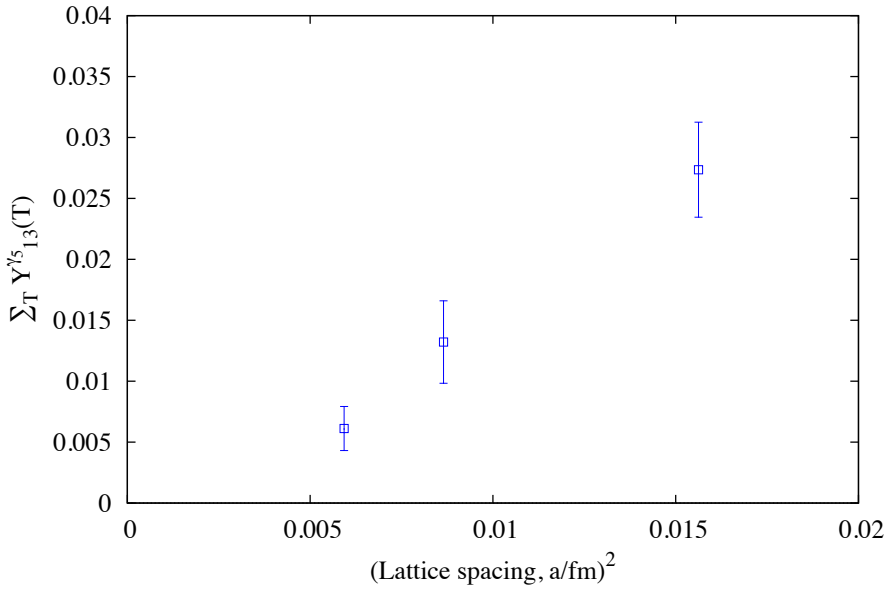

Figure 3.24: Average over the $|Q| = 1$ configurations of $\sum_T Y_{13}^{\gamma_5}(T)$ plotted against a^2 for ensembles 1, 3 and 5. It is expected that $\sum_T Y_{13}^{\gamma_5}(T)$ should vanish with a^2 and $\sum_T Y_{13}^{\gamma_5}(T) = \chi_1\chi_3$ and $\chi_3 \to 0$ as $a \to 0$.

ensembles 1,3 and 5. This combination of eigenvector overlaps is equal to the total correlator with the eigenvalues neglected – in the continuum limit $\lambda_A \to 0$ for the near-zero modes and $m \to 0$ too in the chiral limit. The time $T = T_{mid}$ is chosen to account for the different sizes of the lattices and each histogram is normalised to 1.

Figure 3.29 shows that the distribution is closely centred around zero at finite lattice spacing and becomes narrower as $a \to 0$, indicating the near-zero mode pseudoscalar contributions arising from the near-zero modes cancel out exactly as in the continuum.

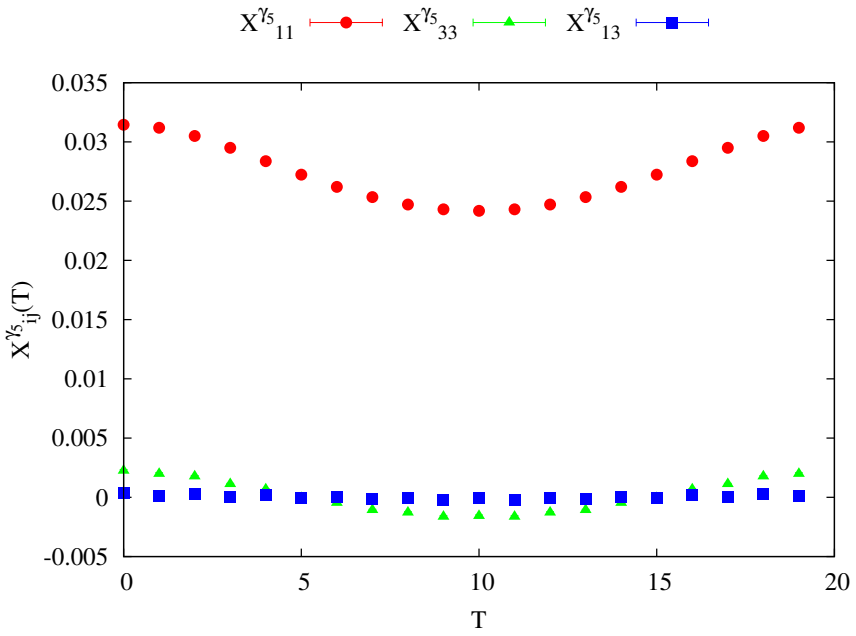

Figure 3.25: Average over the $|Q| = 1$ configurations from ensemble 5 of the connected pseudoscalar contributions $X_{11}^{\gamma_5}(T)$ (filled red circles), $X_{33}^{\gamma_5}(T)$ (filled green triangles) and $X_{13}^{\gamma_5}(T)$ (filled blue squares). Mode 1 is a member of the near-zero quartet and mode 3 a member of the 1st non-zero quartet.

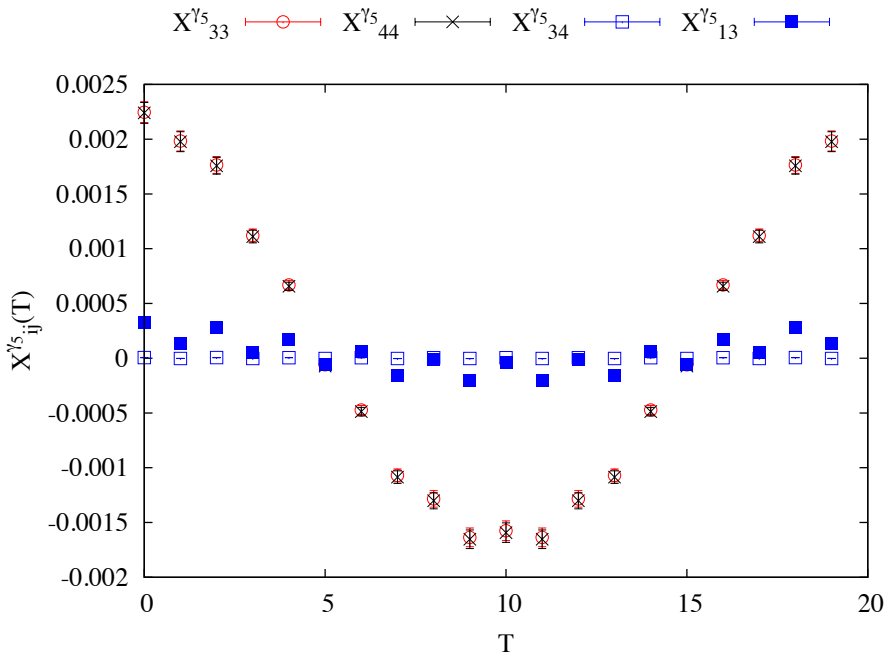

Figure 3.26: Average over the $|Q| = 1$ configurations from ensemble 5 of the connected pseudoscalar contributions $X_{33}^{\gamma_5}(T)$ (red circles), $X_{44}^{\gamma_5}(T)$ (black crosses), $X_{34}^{\gamma_5}(T)$ (blue squares) and $X_{13}^{\gamma_5}(T)$ (filled blue triangles). Modes 3 and 4 are from the same non-zero quartet.

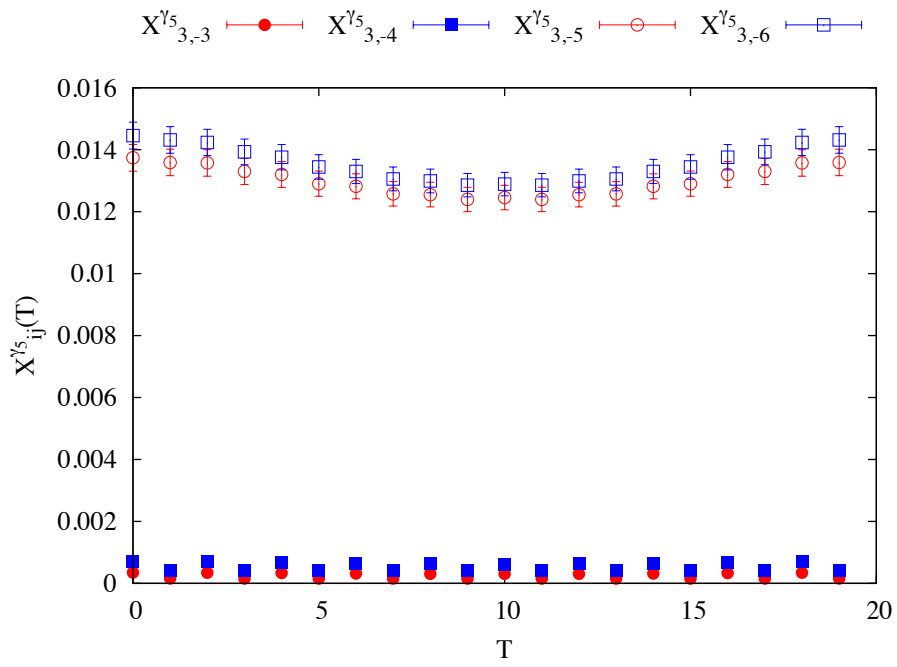

Figure 3.27: Average over the $|Q| = 1$ configurations from ensemble 5 of the connected pseudoscalar contributions $X^{\gamma_5}_{3,-3}(T)$ (filled red circles), $X^{\gamma_5}_{3,-4}(T)$ (filled blue squares), $X^{\gamma_5}_{3,-5}(T)$ (open red circles) and $X^{\gamma_5}_{3,-6}(T)$ (filled blue squares). Mode 3 is in the 1st non-zero quartet and modes -3 $\rightarrow$ -6 are the mirror quartet of eigenmodes.

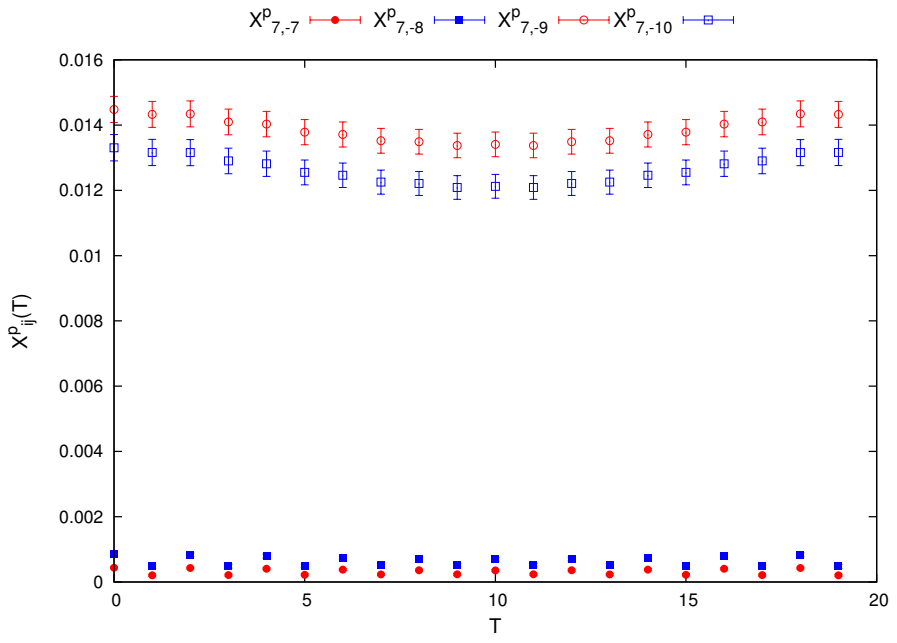

Figure 3.28: Average over the $|Q| = 1$ configurations from ensemble 5 of the connected pseudoscalar contributions $X^{\gamma_5}_{7,-7}(T)$ (filled red circles), $X^{\gamma_5}_{7,-8}(T)$ (filled blue squares), $X^{\gamma_5}_{7,-9}(T)$ (open red circles) and $X^{\gamma_5}_{7,-10}(T)$ (filled blue squares). Mode 3 is in the 2nd non-zero quartet and modes -7 $\rightarrow$ -10 are the mirror quartet of eigenmodes.

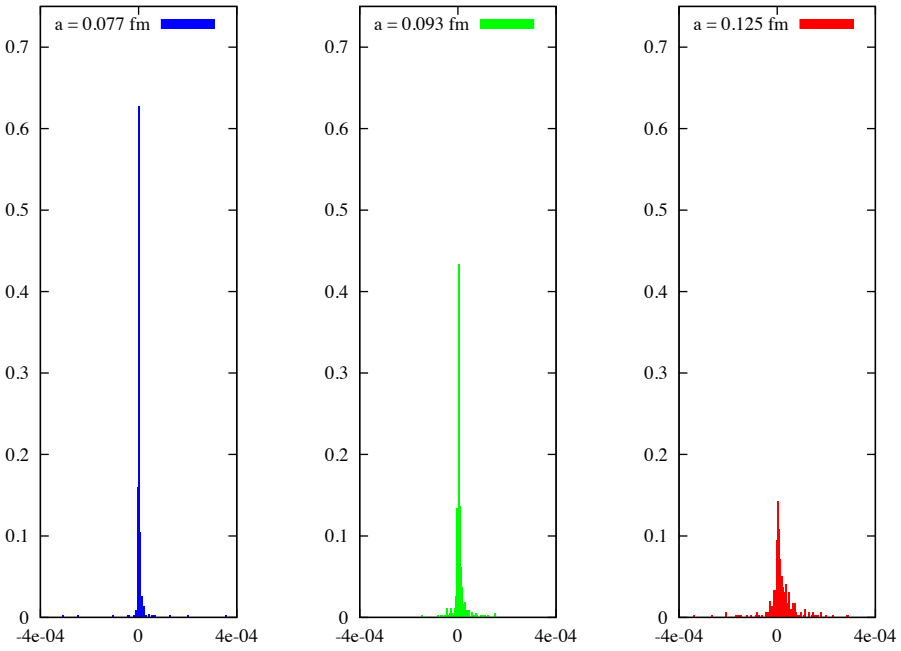

Figure 3.29: Distribution at $T = T_{mid}$ of the total contribution of the near-modes eigenmode overlaps (without the eigenvalues) to the pseudoscalar correlator for the three ensembles with different lattice spacing but the same physical volume. The finest, ensemble 5, is on the left (in blue) with ensemble 3 in the middle (green) and ensemble 1 on the right (red).

3.3.2 Scalar

Expectations for the scalar operator come from the fact that the eigenvectors are orthonormal, both in the continuum and on the lattice. As the taste-singlet scalar operator is also the local one, it is straightforward to explain its behaviour.

Figure 3.30 shows the scalar overlaps $X^1_{AB}(T)$ for modes A, B among the near-zero quartet. It shows a large contribution from the diagonal terms, which is to be expected as $\sum_T X^1_{AA}(T) = 1$ due to the normalisation of the eigenvectors. Similarly, $\sum_T X^1_{AB}(T) = 0$ for $A \neq B$ from the orthogonality of eigenvectors A and B, so the combinations $X^1_{12}(T)$ and $X^1_{1,-1}(T)$ are seen to be zero.

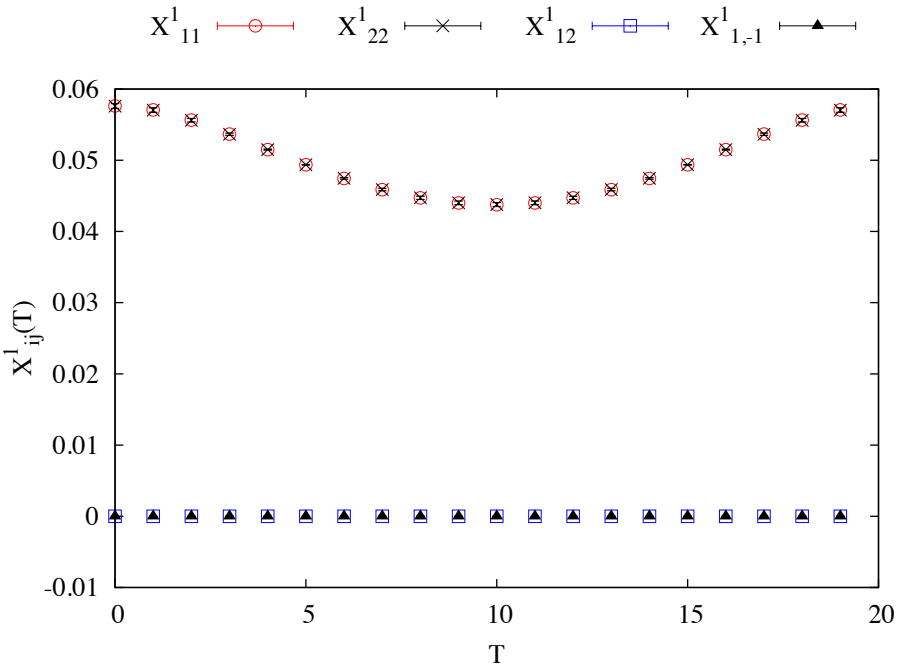

Figure 3.30: Average over the $|Q| = 1$ configurations from ensemble 5 of the connected scalar contributions $X^1_{11}(T)$ (red circles), $X^1_{22}(T)$ (black crosses), $X^1_{12}(T)$ (blue squares) and $X^1_{1,-1}(T)$ (filled black triangles).

The disconnected scalar overlaps are shown in Figure 3.31 for modes 1 and 3. For the scalar, there is no qualitative difference is the behaviour of the near-zero mode 1 and the non-zero mode 3. For the scalar operator $\sum_T Y^1_{AB}(T) = N_A N_B = 1$, where N_A is just the normalisation of eigenvector A and $N_A = \sum_i f^\dagger_A(i) f_A(i) = 1$ for all the eigenvectors. Therefore, the off-diagonal contribution $Y^1_{13}(T)$ is also large. Note that this reflects what would happen in the continuum, where again there is no difference between the zero and non-zero modes in how they overlap with a scalar operator.

In Figure 3.32, the contributions to the connected correlator arising from a combination of modes 1 and 3 is examined. $X^1_{13}(T)$ is zero, which is to be expected as the lattice eigenvectors 1 and 3 are orthogonal. This is again analogous to the continuum as modes 1 and 3 are representatives of quartets from different continuum eigenmodes, which would also be orthogonal.

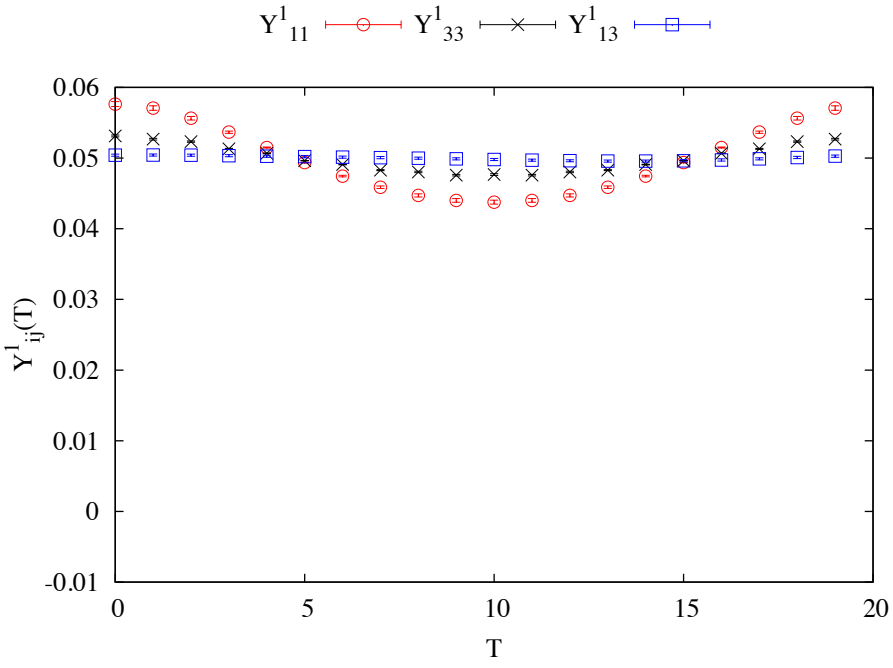

Figure 3.31: Average over the $|Q| = 1$ configurations from ensemble 5 of the disconnected scalar contributions $Y^1_{11}(T)$ (red circles), $Y^1_{33}(T)$ (black crosses) and $Y^1_{13}(T)$ (blue squares).

The scalar overlaps of the eigenvectors in the 1st non-zero quartet are shown in Figure 3.33. As the modes in the quartet are orthogonal, the large overlaps come from the diagonal pieces, $X^1_{AA}(T)$, the same as for the near-zero modes.

In Figure 3.34, the overlaps between mode 3 and modes in the mirror quartet (-3 to -6) are plotted. As these modes are orthogonal, all the overlaps sum to zero and are very small, showing different behaviour to the pseudoscalar.

Returning once again to just the near-zero quartet, the potentially divergent pieces of the scalar flavour-singlet meson correlator are easy to find. As was the case for the pseudoscalar, there are 4 large contributions to the connected correlator and 16 to the disconnected correlator. Figure 3.35 shows histograms of

$$\sum_{AB} -\frac{X^1_{AB}(T_{mid})}{4} + \frac{X^1_{AB}(T_{mid})}{16} \tag{3.39}$$

on ensembles 1,3 and 5 with varying lattice spacing.

Once again, this combination is close to zero and the distribution narrows in the limit $a \to 0$.

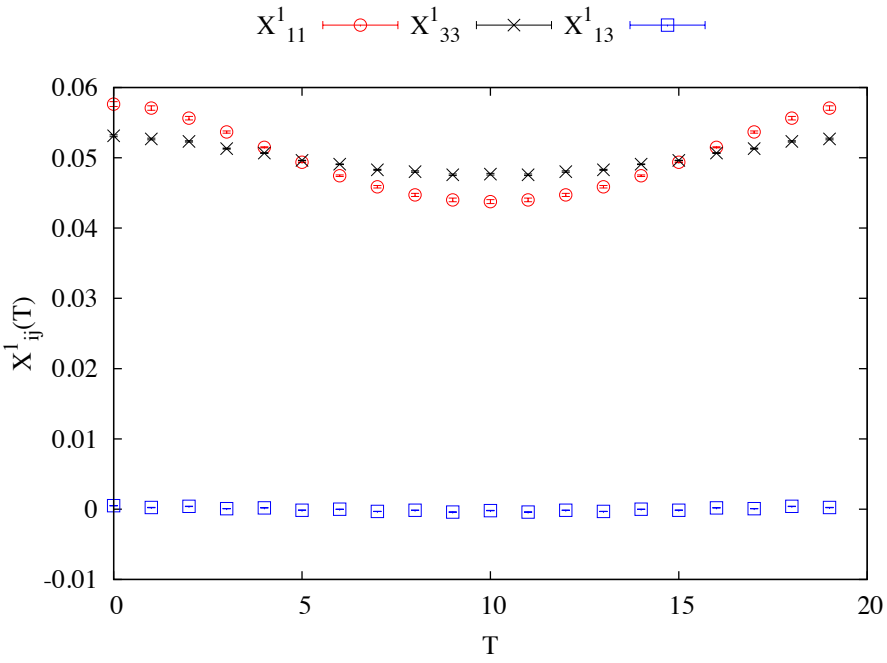

Figure 3.32: Average over the $|Q| = 1$ configurations from ensemble 5 of the connected scalar contributions $X^1_{11}(T)$ (red circles), $X^1_{33}(T)$ (black crosses), $X^1_{13}(T)$ (blue squares). Mode 1 is from the near-zero quartet and mode 3 is a member of the 1st non-zero quartet.

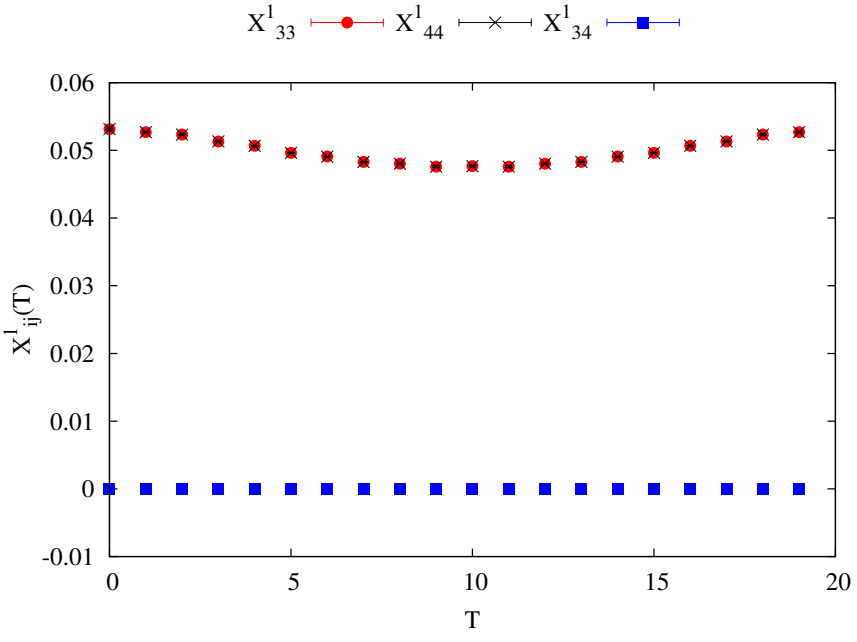

Figure 3.33: Average over the $|Q| = 1$ configurations from ensemble 5 of the connected scalar contributions $X^1_{33}(T)$ (filled red circles), $X^1_{44}(T)$ (black crosses), $X^1_{34}(T)$ (blue squares). Modes 3 and 4 are in the 1st non-zero quartet.

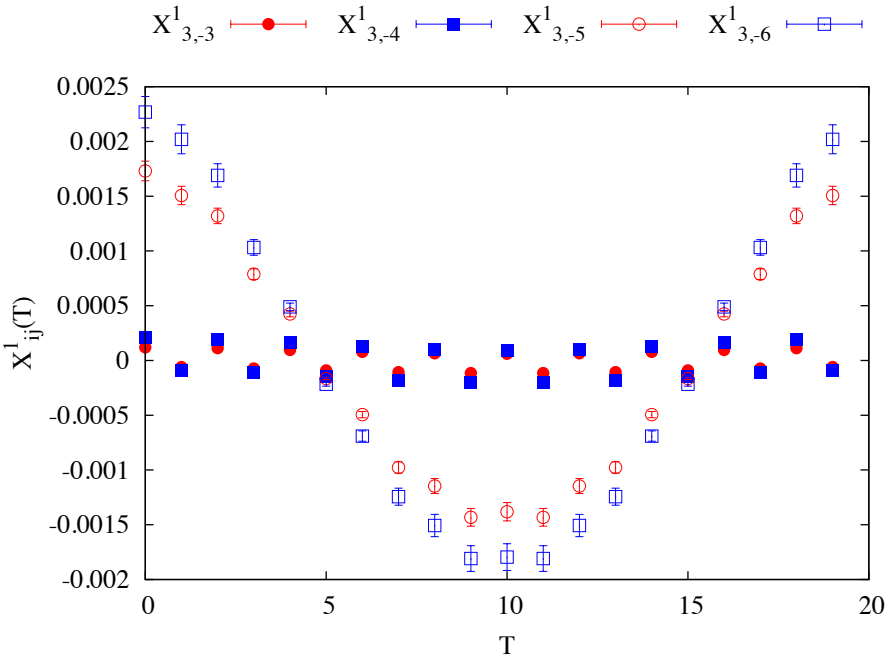

Figure 3.34: Average over the $|Q| = 1$ configurations from ensemble 5 of the connected scalar contributions $X^1_{3,-3}(T)$ (filled red circles), $X^1_{3,-4}(T)$ (filled blue squares), $X^1_{3,-5}(T)$ (open red circles) and $X^1_{3,-6}(T)$ (filled blue squares). Mode 3 is in the 1st non-zero quartet and modes -3 $\rightarrow$ -6 are the mirror quartet of eigenmodes.

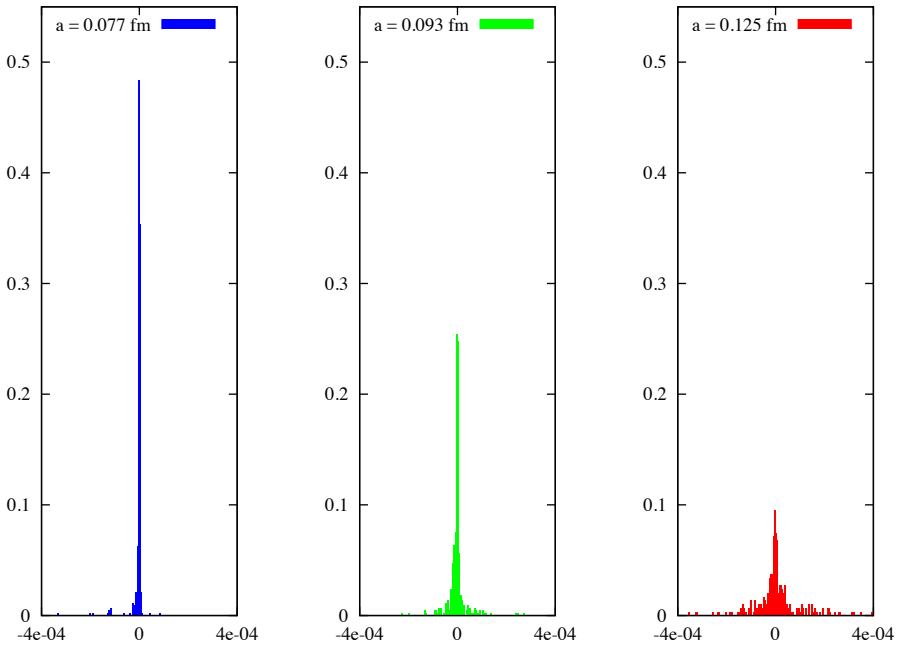

Figure 3.35: Distribution at $T = T_{mid}$ of the total contribution of the near-modes eigenmode overlaps (without the eigenvalues) to the scalar correlator for the three ensembles with different lattice spacing but the same physical volume. The finest, ensemble 5, is on the left (in blue) with ensemble 3 in the middle (green) and ensemble 1 on the right (red).

3.3.3 Vector

As previously discussed, the vector overlaps of the near-zero modes are expected to vanish as their continuum analogue is zero:

$$\sum_x \phi_0^\dagger(x)\gamma_\mu\phi_0(x) = 0. \tag{3.40}$$

It therefore follows that the total zero mode contribution to each of the connected and disconnected correlators is zero.

The taste-singlet staggered vector operator is a 1-link operator connecting even to odd lattice sites and therefore has different symmetries to operators connecting even sites to even sites and odd to odd (like the pseudoscalar and scalar operators). This means that

$$\tilde{\zeta}^{\gamma_\mu}_{AB}(t) = (-1)^{i_\mu^<}\sum_{\vec{i}} f_A(i)\gamma_\mu f_B(i+\hat{\mu}) = -\tilde{\zeta}^{\gamma_\mu}_{-A,-B}(t). \tag{3.41}$$

as $\varepsilon(i) = -\varepsilon(i+\hat{\mu})$ The same behaviour is seen for vector operators in all directions. The results shown are for a vector in the $\mu = x$ direction.

From the definition of the disconnected correlator contributions, Equation 3.27, it follows that

$$Y^{\gamma_\mu}_{AB}(T) = Y^{\gamma_\mu}_{-A,-B}(T) = -Y^{\gamma_\mu}_{-A,B}(T) = -Y^{\gamma_\mu}_{A,-B}(T) \tag{3.42}$$

and all these related contributions will cancel out, leaving the disconnected correlator exactly zero.

Figure 3.36 shows the vector disconnected correlator contributions from the modes $A = \pm 1$. It clearly demonstrates that $Y^{\gamma_\mu}_{11}(T) = Y^{\gamma_\mu}_{-1,-1}(T) = -Y^{\gamma_\mu}_{1,-1}(T)$. It is noticeable too that, aside from the cancellation between them, each of these terms is purely an oscillation.

Recalling that the diagonal $X^{\gamma_\mu}_{AA}(T) = Y^{\gamma_\mu}_{AA}(T)$, the low-lying modes' contributions to the connected correlator are plotted in Figure 3.37. All of the terms here are small (compared to the pseudoscalar and scalar contributions which have a non-zero continuum analogue) and purely oscillatory. As there is only an oscillation, the near-zero modes would make no contribution to the non-oscillating vector states in a simulation using staggered quarks.

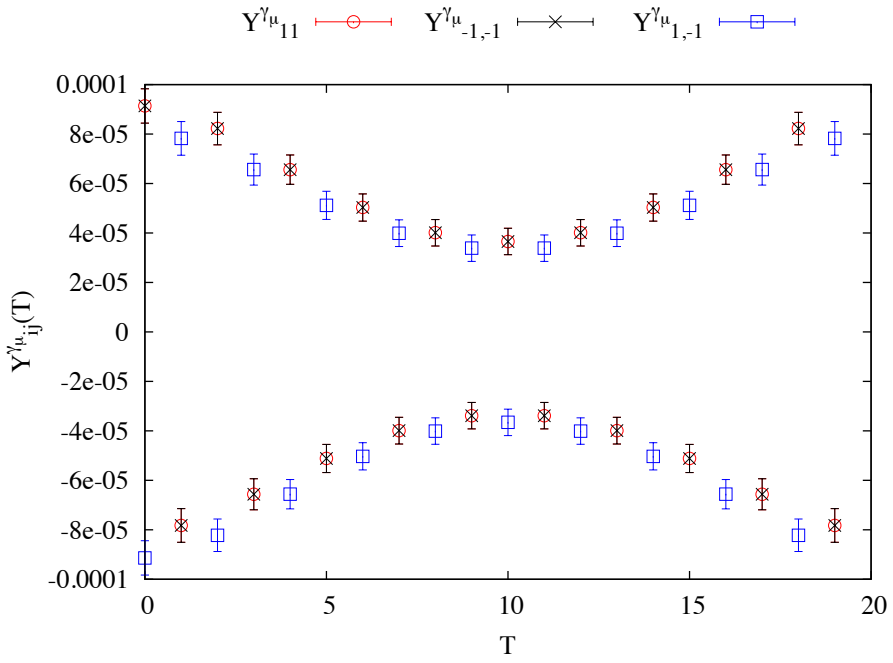

Figure 3.36: Average over the $|Q| = 1$ configurations from ensemble 5 of the disconnected vector contributions $Y_{11}^{\gamma_\mu}(T)$ (red circles), $Y_{-1,-1}^{\gamma_\mu}(T)$ (black crosses) and $Y_{1,-1}^{\gamma_\mu}(T)$ (blue squares). All of these contributions are purely oscillatory.

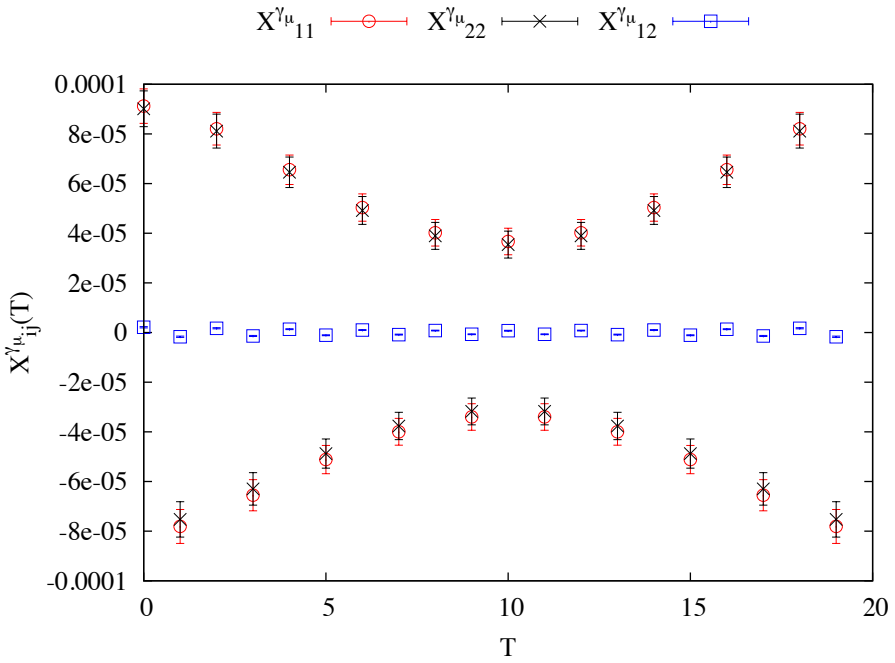

Figure 3.37: Average over the $|Q| = 1$ configurations from ensemble 5 of the connected vector contributions $X_{11}^{\gamma_\mu}(T)$ (red circles), $X_{22}^{\gamma_\mu}(T)$ (black crosses) and $X_{12}^{\gamma_\mu}(T)$ (blue squares).

3.3.4 Axial vector

Like the vector, the taste-singlet axial vector connects evens sites to odd. It behaves in a similar way to the vector, so the near-zero modes' contribution to the disconnected correlator is zero. The operator is a 3-link operator and can be written explicitly as

$$\tilde{\zeta}_{AB}^{\gamma_\mu\gamma_5}(t) = \pm \sum_{\vec{i}} \varepsilon(i)(-1)^{i_\mu} \prod_{\nu\neq\mu} (-1)^{i_\nu^<} f_A^\dagger(i) f_B(i+\hat{4}-\hat{\mu}), \tag{3.43}$$

where the overall sign is $+1$ for $\mu = x, z$ and -1 for $\mu = y, t$.

In Figure 3.38, the contributions of modes 1 and 2 (in the near-zero quartet) to the connected correlator. The behaviour is very similar to the same modes' contribution to the connected vector correlator in Figure 3.37. As in that case, the only contributions to the correlator are purely oscillatory and do not correspond to a state coupling to the axial vector operator. Again, the direction μ in the axial vector operator does not change the picture seen and the data shown is for $\mu = x$

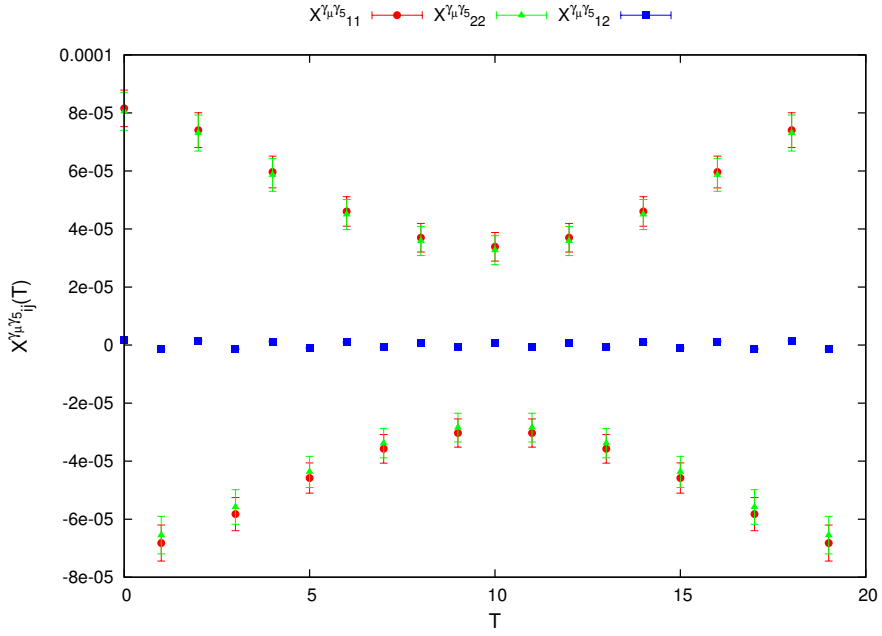

Figure 3.38: Average over the $|Q| = 1$ configurations from ensemble 5 of the connected axial vector contributions $X_{11}^{\gamma_5\gamma_\mu}(T)$ (filled red circles), $X_{22}^{\gamma_5\gamma_\mu}(T)$ (filled green triangles) and $X_{12}^{\gamma_5\gamma_\mu}(T)$ (filled blue squares).

3.3.5 Tensor

The taste-singlet tensor operator resembles the scalar and pseudoscalar in that it connects even site to even sites because it is a two-link operator.

The behaviour is the same whether the two tensor directions are both spatial or one is the temporal direction and the other is spatial. Figure 3.39 plots the contributions of modes 1 and 2 to the connected correlator for a tensor operator in the x and y

directions. This is

$$\tilde{\zeta}_{AB}^{\gamma_x\gamma_y}(t) = \sum_{\vec{i}} -(-1)^{i_x} f_A^\dagger(i) f_B(i+\hat{x}+\hat{y}). \tag{3.44}$$

As before, the disconnected correlator contributions are related by $X_{AA}^{\gamma_\mu\gamma_\nu}(T) = Y_{AA}^{\gamma_\mu\gamma_\nu}(T)$. The disconnected $Y_{AA}^{\gamma_\mu\gamma_\nu}(T)$ contains 16 terms with approximately the same sizeable contribution, while the connected correlator has four significant contributions from the diagonal pieces. The cancellation of the connected and disconnected pieces relies on the vanishing of the off-diagonal contributions to the connected correlator.

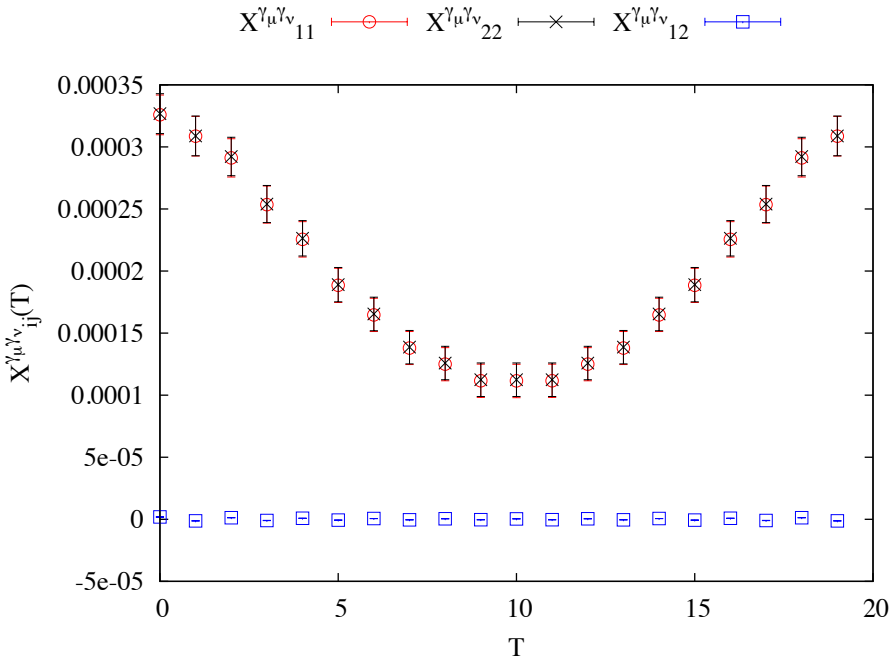

Figure 3.39: Average over the $|Q| = 1$ configurations from ensemble 5 of the connected tensor contributions $X_{11}^{\gamma_\mu\gamma_\nu}(T)$ (red circles), $X_{22}^{\gamma_\mu\gamma_\nu}(T)$ (black crosses) and $X_{12}^{\gamma_\mu\gamma_\nu}(T)$ (blue squares).

In Figure 3.39, the off-diagonal term $X_{12}^{\gamma_\mu\gamma_\nu}(T)$ is smaller than the diagonal terms and oscillatory, so this satisfies the requirements needed for the cancellation in the total correlator.

Figure 3.40 shows histograms of the combined contribution of the near-zero quartet to the total correlator on ensembles 1,3 and 5. As for the scalar and pseudoscalar, it is narrowly distributed around zero and the distribution becomes narrower as $a \to 0$.

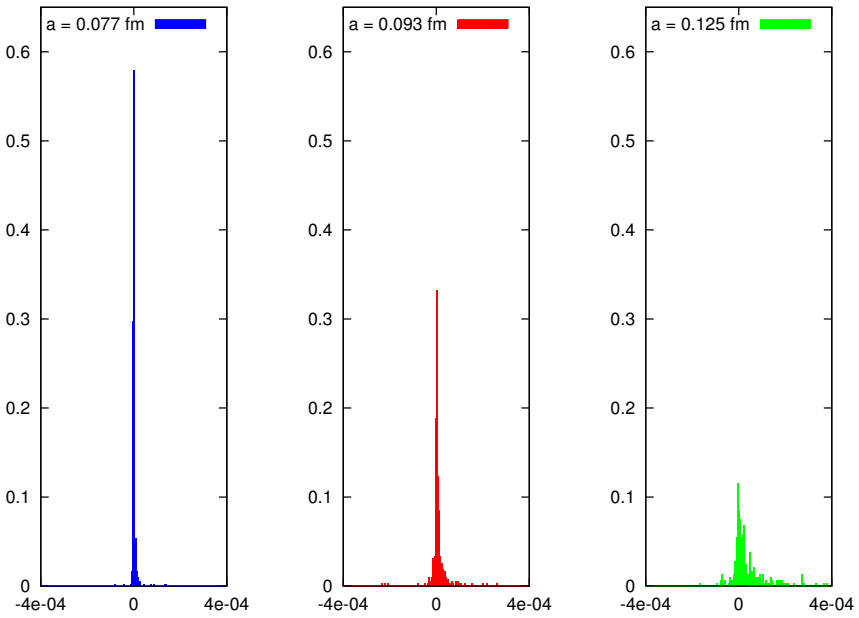

Figure 3.40: Distribution at $T = T_{mid}$ of the total contribution of the near-modes eigenmode overlaps (without the eigenvalues) to the tensor correlator for the three ensembles with different lattice spacing but the same physical volume. The finest, ensemble 5, is on the left (in blue) with ensemble 3 in the middle (green) and ensemble 1 on the right (red).

3.3.6 $|Q| = 2$

The behaviour of the quartets of near-zero staggered eigenmodes can be understood by looking at configurations with $|Q| = 1$ and only one near-zero quartet. The contributions of pairs of eigenmodes within a near-zero or non-zero quartet can easily be studied, as can the combination of a near-zero and non-zero mode. For cases with $|Q| > 1$, the only new issue is the overlap between modes in different near-zero quartets. Modes in distinct quartets correspond to different continuum zero modes in the $a \to 0$ limit and, in the continuum, the zero modes are orthogonal to one another if there are more than one of them.

The expectation on the lattice is that there should be no extra contribution from near-zero modes in different quartets. In Figure 3.41, the averaged contribution from modes 1 and 3 is plotted for 27 configurations on the finest ensemble, ensemble 5, with $|Q| = 2$. On these configurations, the modes $\pm 1, \pm 2$ are a near-zero quartet with degenerate eigenvalues close to zero and modes $\pm 3, \pm 4$ are another near-zero quartet, so the modes shown in Figure 3.41 are near-zero modes in different quartets.

The diagonal contributions to the connected pseudoscalar operator $X_{11}^{\gamma_5}(T)$ and $X_{33}^{\gamma_5}(T)$ are both large, indicating that both modes 1 and 3 are near-zero modes, but the off-diagonal contribution $X_{13}^{\gamma_5}(T)$ is zero, as expected for modes in different quartets.

The contribution $X_{13}^{\gamma_5}(T)$ in Figure 3.41 closely resembles the $X_{13}^{\gamma_5}(T)$ in Figure 3.25 which shows the overlap between modes 1 and 3 where mode 3 is part of a non-zero quartet.

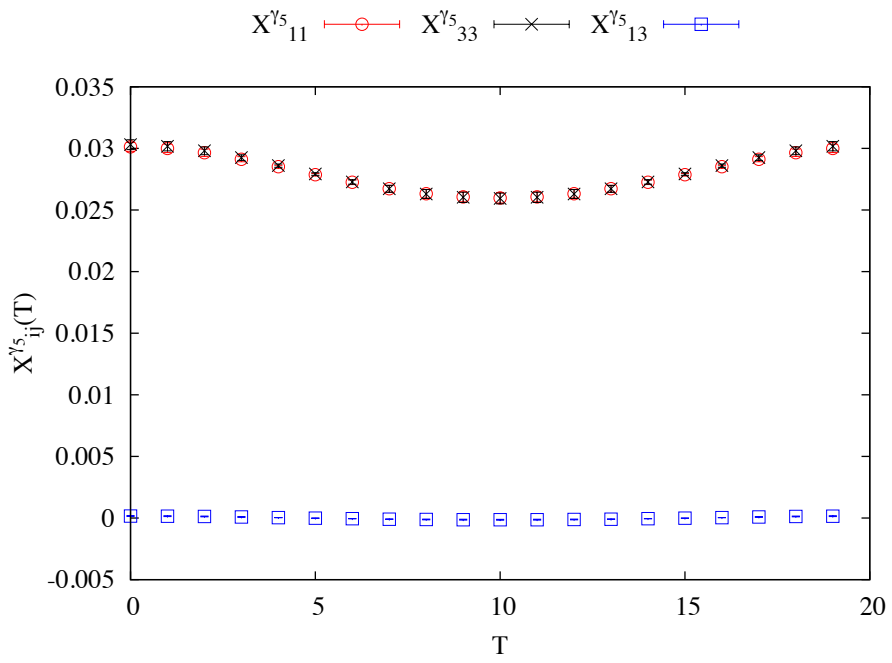

Figure 3.41: Average over the $|Q| = 2$ configurations from ensemble 5 of the connected pseudoscalar contributions $X_{11}^{\gamma_5}(T)$ (red circles), $X_{33}^{\gamma_5}(T)$ (black crosses) and $X_{13}^{\gamma_5}(T)$ (blue squares). Modes 1 and 3 and near-zero modes from each of the two near-quartets on the $|Q| = 2$ configurations.

3.3.7 Local pseudoscalar

It is instructive to look at the 'Goldstone' local pseudoscalar operator, $\gamma_5 \otimes \gamma_5$. The phase factor for this operator is $\varepsilon(i)$, which anticommutes with the massless $\not{D}_{HISQ}$ and plays the role of the continuum γ_5 in the definition of the mirror eigenmodes with eigenvalues of opposite sign. This operator is used in [37] to draw conclusions about staggered flavour-singlet mesons.

However, $\gamma_5 \otimes \gamma_5$ is not a taste-singlet and is not the right operator to study the η' meson because it does not couple to gluons. Therefore, there is no disconnected piece for $\gamma_5 \otimes \gamma_5$. There is only the connected piece, which is closely related to the scalar and comes from the definition of

$$\zeta_{AB}^{\gamma_5 \otimes \gamma_5} = \sum_{\vec{i}} f_A^\dagger(i)\varepsilon(i)f_B(i). \tag{3.45}$$

Therefore, it is clear that

$$\zeta_{AB}^{\gamma_5 \otimes \gamma_5} = \zeta_{A,-B}^{1} \implies X_{AB}^{\gamma_5 \otimes \gamma_5} = X_{A,-B}^{1} \tag{3.46}$$

and it follows that the total contribution of a quartet of eigenmodes is the same for the scalar and Goldstone pseudoscalar

$$\sum_{AB=\pm1,\pm2} X_{AB}^{\gamma_5 \otimes \gamma_5} = \sum_{AB=\pm1,\pm2} X_{AB}^{1}. \tag{3.47}$$

On its own, the connected piece does diverge in the chiral limit as

$$C^{\gamma_5\otimes\gamma_5}(i,j) \sim \sum_{4 \text{ modes}} \frac{1}{m^2} \left(\zeta^{\gamma_5\otimes\gamma_5}_{A,-A}\right)^2 = \frac{4}{m^2} \left(\zeta^{\gamma_5\otimes\gamma_5}_{A,-A}\right)^2 . \tag{3.48}$$

This indicates that a flavour-non-singlet pseudoscalar meson will be massless in the limit of the quark mass $m_q \to 0$, which is the expected behaviour for the Goldstone pion simulated with a $\gamma_5 \otimes \gamma_5$ operator and containing only a connected contribution to the correlator.

Chapter 4

Flavour physics with HISQ

4.1 Random wall sources for propagators

On the lattice, results for meson masses and decays are extracted from correlation functions. A correlation function for a meson created with J^{PC} set by Γ at site i and destroyed at j is given by

$$\langle\bar{\psi}(i)\Gamma\psi(i)\bar{\psi}(j)\Gamma\psi(j)\rangle. \tag{4.1}$$

Applying the staggering transformations and Wick contracting the fermion fields gives the correlation function in terms of staggered quark propagators

$$\mathrm{Tr}(\Omega(i)g(i,j)\Omega^{\dagger}(j)\Gamma\Omega(j)g(j,i)\Omega^{\dagger}(i)\Gamma) \tag{4.2}$$

where $g(i,j)$ is the propagator and the trace is over colour.

The staggered quark propagator $g(i,j)$ is obtained by inverting the Dirac matrix $[\not{D}_{stag}+m](i,j)$, where m is the quark mass. The inversion is carried out using code for a conjugate gradient algorithm written by Eduardo Follana. For a square matrix M and vector b, the conjugate gradient algorithm solves

$$Mx = b \tag{4.3}$$

for x.

For a propagator inversion, the matrix in Equation 4.3 is the Dirac matrix $[\not{D}_{stag}+m](i,j)$ and $b=\eta(i)$ is called the source vector. The solution is $g(j)=\sum_i g(i,j)\eta(i)$ because the propagator $g(i,j)$ is the inverse of $[\not{D}_{stag}+m](i,j)$. Therefore $g(j)$ describes the propagation of a quark from site i to all sites j.

To increase the statistics, a random wall source is used for $\eta(i)$, where the source vector is defined for all sites on the source timeslice t_0. The source vector $\eta(i)=0$ for all sites i where $i_t \neq t_0$ and $\eta(i)=e^{i\theta}$, a complex number with random phase and modulus one when $i_t=t_0$. If $\eta(i)$ is non-zero on just one site, i, the resultant propagator $g(j)$ then describes propagation from all sites i on timeslice t_0 to site j.

These propagators can be contracted to give the correlators as

$$g^\dagger(j)g(j) = \sum_{i,i'} g^\dagger(i',j)g(i,j)\eta^\dagger(i')\eta(i) \simeq \sum_{i,i'} g^\dagger(i',j)g(i,j)\delta_{ii'} = \sum_i g^\dagger(i,j)g(i,j) \tag{4.4}$$

as all the contributions from $i' \neq i$ will average to zero and only contribute noise to the correlator. This increases the statistics as the source is at all spatial sites at t_0, rather than just one.

With staggered quarks, not just the source timeslice is embedded in $g(j)$; so too is the source operator as the corresponding staggered phase and point-splitting needs to be applied to $\eta(i)$. To make a local vector (where the vector operator is in the x direction so $\gamma_x \otimes \gamma_x$) meson correlator, there needs to be a phase of $(-1)^{i_x}$ at the source. The correlator is made by combining a propagator $g_\eta(j)$ made with a random wall source $\eta(i)$ and $g_\rho(j)$ made with a source $\rho(i) = \eta(i)(-1)^{i_x}$.

A similar modification to the wall source must be done for point split operators at the source. For a 1-link $\gamma_x \otimes 1$ vector meson correlator, $g_\eta(j)$ is combined with $g_\sigma(j)$ made using source vector $\sigma(i) = \frac{1}{2}[\eta(i+\hat{x}) + \eta(i-\hat{x})]$. The point-splitting for a non-local operator is done symmetrically in the forward and backward directions.

Random wall sources for staggered operators with different tastes can be added together. A propagator made with source $\tau(i) = \rho(i) + \sigma(i)$ will satisfy $g_\tau(j) = g_\rho(j) + g_\sigma(j)$ and either source operator can be extracted in a 2-point correlator by using the appropriate operator at the sink. This works because

$$\begin{aligned} &\langle \left[\bar{\psi}(i)(\gamma_x \otimes \gamma_x)\psi(i) + \bar{\psi}(i)(\gamma_x \otimes 1)\psi(i)\right] \ \bar{\psi}(j)(\gamma_x \otimes \gamma_x)\psi(j)\rangle \\ =&\langle \bar{\psi}(i)(\gamma_x \otimes \gamma_x)\psi(i) \ \bar{\psi}(j)(\gamma_x \otimes \gamma_x)\psi(j)\rangle + \text{ noise} \end{aligned} \tag{4.5}$$

and similarly

$$\begin{aligned} &\langle \left[\bar{\psi}(i)(\gamma_x \otimes \gamma_x)\psi(i) + \bar{\psi}(i)(\gamma_x \otimes 1)\psi(i)\right] \ \bar{\psi}(j)(\gamma_x \otimes 1)\psi(j)\rangle \\ =&\langle \bar{\psi}(i)(\gamma_x \otimes 1)\psi(i) \ \bar{\psi}(j)(\gamma_x \otimes 1)\psi(j)\rangle + \text{ noise.} \end{aligned} \tag{4.6}$$

This is straightforward to extend to 3-point functions as well. Figure 4.1 shows data for the $D_s \to \phi$ 3-point correlator (this calculation uses MILC configurations with 2+1 flavours of asqtad sea quarks and is discussed in Chapter 7) calculated using propagators $g_\tau(j)$ and $g_\sigma(j)$. The data plotted is the ratio of the 3-point correlator to the 2-point correlators

$$\frac{C_{3pt}(t)}{C_{2pt,\phi}(t)C_{2pt,D_s}(T-t)}. \tag{4.7}$$

The red points are the ratio calculated using g_σ which has 1 taste in the source vector and the blue with g_τ which includes the sum of two tastes in the source vector.

Figure 4.1 shows the data agrees for these two calculations, but there are bigger errors when the source vector contains a extra random wall of another taste. This is not

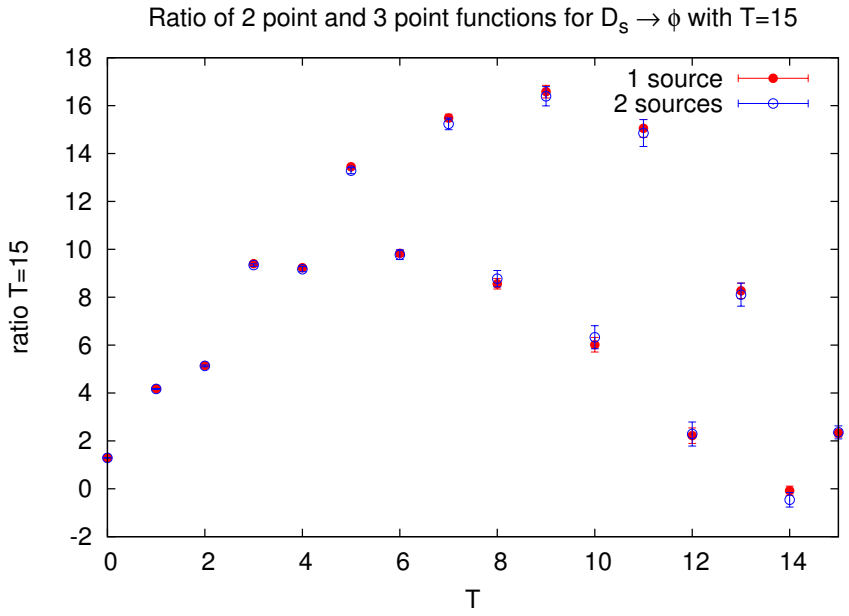

Figure 4.1: The ratio of the 3-point to 2-point correlators, where the propagator containing the $\gamma_\mu \otimes 1$ vector operator for the ϕ meson is computed with either a single random wall source (red points labelled 1 source) or the sum of two random walls (blue points labelled 2 sources).

surprising as the second operator at the source generates extra noise which contributes to the statistical error.

4.2 Fitting

Staggered two-point correlators are fitted as a function of the time separation between the source and sink, t. Figure 4.2 shows a diagram of 2-point correlator between $t_0 = 0$ and t. Staggered correlators contain oscillating states so are fitted to

$$C^{2pt}(t) = \sum_{A,A_o} a_A^2 e^{-E_A t} + (-1)^t a_{A_o}^2 e^{-E_{A_o}^{osc} t}. \tag{4.8}$$

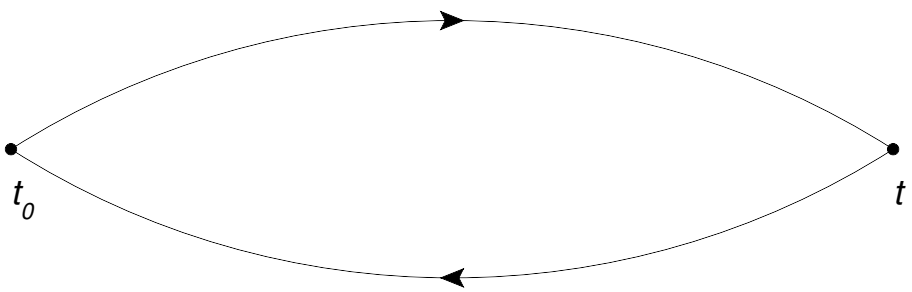

Figure 4.2: A diagram of the quark propagators in a 2-point correlator for a meson propagating from the source $t_0 = 0$ to time t.

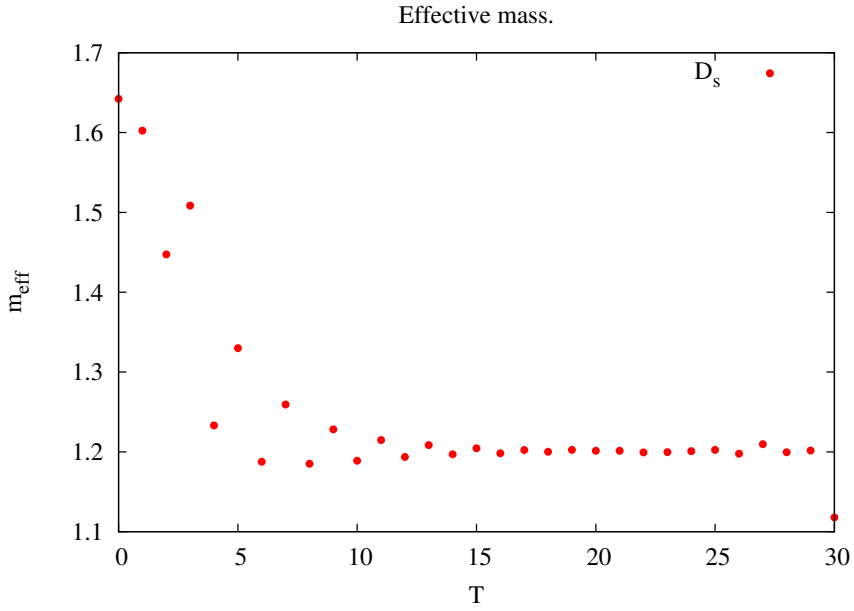

Figure 4.3: The effective mass of a D_s meson. The charm and strange quarks are staggered, so oscillations are observed in the effective mass. The temporal length of the lattice is 64 and the effect of periodic boundary conditions starts to become apparent at the midpoint of the lattice.

The sum is over states A with the same quantum numbers, which are dictated by Γ in the calculation. At rest, the energies of the states equal their masses $E_A = m_A$. The fit amplitudes a_A are related to the matrix element $\langle 0|\Gamma|A\rangle$ and give information about the decays of meson A.

In practice, because periodic boundary conditions are used, Equation 4.8 becomes

$$C^{2pt}(t) = \sum_{A,A_o} a_A^2(e^{-E_A t} + e^{-E_A(L_t-t)}) + (-1)^t a_{A_o}^2(e^{-E_{A_o}^{osc} t} + e^{-E_{A_o}^{osc}(L_t-t)}), \qquad (4.9)$$

where L_t is the time extent of the lattice. The extra terms account for mesons propagating on the lattice in the other direction. These terms are present in all the 2-point correlator fits, but will not be written out explicitly from now on.

The oscillating contributions come from the time doubler. These oscillation contributions in the data can clearly be seen in Figure 4.1.

At large values of t, the correlator is dominated by the ground state, E_0, which is usually the most interesting one. The ground state mass can be estimated by the large t value of the effective mass,

$$m_{eff}(t) = -\ln\left[\frac{C^{2pt}(t+1)}{C^{2pt}(t)}\right]. \qquad (4.10)$$

The effective mass for a D_s meson is plotted in Figure 4.3. This is a pseudoscalar meson containing a charm and strange quark, both simulated with the HISQ action. The semileptonic decay of the D_s to $\phi\ell\nu$ is discussed in Chapter 7.

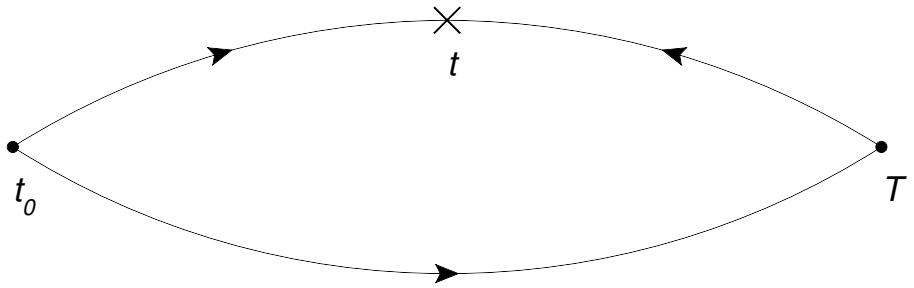

Figure 4.4: A diagram of a 3-point correlator, where a meson is created at time $t_0 = 0$. There is a weak or electromagnetic current inserted at t and the final state meson is destroyed at time T.

3-point correlation functions are fitted analogously. For a 3-point function, as shown in Figure 4.4, where one meson A is created at the source time taken to be $t = 0$ and the final state meson B is destroyed at T, the correlation function is fitted between $t_0 = 0$ and T. It takes the form

$$\begin{aligned} C^{3pt}(t,T) = \sum_{A,B,A_o,B_o} & a_A a_B V^{nn}_{AB} e^{-E_A t} e^{-E_B(T-t)} \\ & + (-1)^t a_{A_o} a_B V^{on}_{A_o B} e^{-E_{A_o} t} e^{-E_B(T-t)} \\ & + (-1)^T a_A a_{B_o} V^{no}_{AB_o} e^{-E_A t} e^{-E_{B_o}(T-t)} \\ & + (-1)^{t+T} a_{A_o} a_{B_o} V^{oo}_{A_o B_o} e^{-E_{A_o} t} e^{-E_{B_o}(T-t)}. \end{aligned} \tag{4.11}$$

This includes oscillations at both ends of the correlator. The superscripts n and o in the V_{AB} terms indicate whether the 3-point amplitude couples non-oscillating or oscillating states.

The data is fitted to the expected form using a multi-exponential fit. $C(t)$ is a function of the fit parameters, a_A and E_A and $\bar{C}(t)$ is the correlator data. The statistical errors in the data are reduced by averaging over different source timeslices on the same configuration. The best fit is found by minimising

$$\chi^2 = \sum_{tt'} \Delta C(t) \sigma^{-2}_{tt'} \Delta C(t') \tag{4.12}$$

where $\Delta C(t) = \bar{C}(t) - C(t)$ is the difference between the data and the fit and

$$\sigma^2_{tt'} = C(t)\bar{C}(t') - \bar{C(t)}\bar{C(t')} \tag{4.13}$$

is the correlation matrix.

It is easiest to extract the ground state from the data, but the more excited states are less well determined by the data and allowed to take on unreasonable values – for example the amplitudes for high-energy states could be many times larger than for the ground state [51]. For a large number of exponentials, this results in excessively large

errors for the ground state parameters.

The poorly determined parameters can be constrained by instead minimising $\chi^2_{aug} = \chi^2 + \chi^2_{prior}$, where the χ^2 is augmented by

$$\chi^2_{prior} = \sum_A \frac{(a_A - \bar{a}_A)^2}{\sigma^2_{a_A}} + \sum_A \frac{(E_A - \bar{E}_A)^2}{\sigma^2_{E_A}}. \tag{4.14}$$

This favours $a_A = \bar{a}_A \pm \sigma_{a_A}$ in the fit.

The terms $\bar{a}_A$ and σ_{a_A} are priors for a_A and inputs to the fit. They should be chosen to have values based on reasonable expectations for the parameters. Typically, the prior used for the ground state energy is taken from an effective mass plot, the energy splittings between successive states are taken to be around 600 MeV with widths of 300 MeV and the amplitudes typically have priors of around $\bar{a}_A(\sigma_{a_A}) = 0.1(1.0)$.

Adding priors to the fit input also means there can be arbitrarily many exponentials without the number of parameters to be fitted exceeding the number of data points. This is because there is a new prior added for each new parameter in the fit. In practice, the fit is done by increasing n_{exp}, the number of exponentials and the fit converges when the ground state parameters do not change as more terms are added to the fit. Constrained multi-exponential fitting can account for the staggered oscillations by including them in the fit form; usually the number of oscillating exponential terms in the fit is $n_{exp} - 1$.

It is useful to fit correlators with shared parameters simultaneously to take account of correlations in the data. A clear example where simultaneous fits are useful is 3-point amplitude where the fit parameter V^{nn}_{AB} is of interest. In the 3-point fit function, this term appears as $a_A V^{nn}_{AB} a_B$, where a_A and a_B are found by fitting the corresponding 2-point correlators.

The fit amplitudes, a_A, are related to matrix elements for creating meson P_A with energy E_0, $\langle 0|\Gamma|P_A\rangle$ by

$$a_A = \frac{\langle 0|\Gamma|P_A\rangle}{\sqrt{2E_A}}. \tag{4.15}$$

This is because the 2-point correlator has a relativistic normalisation. Assuming, for simplicity, the correlator is dominated by the ground state,

$$C_{2pt}(t) = \frac{|\langle 0|\Gamma|P_0\rangle|^2 e^{-M_0 t}}{2E_0}. \tag{4.16}$$

3-points correlators are similarly normalised. Again assuming only the ground states mesons P_0 and P'_0 with respective energies E_0 and E'_0 contribute, the correlator is

$$C_{3pt}(t,T) = \frac{\langle 0|\Gamma|P_0\rangle e^{-M_0 t}\langle P_0|\Gamma'|P'_0\rangle e^{-M'_0(T-t)}\langle P'_0|\Gamma|0\rangle}{2E_0 2E'_0}. \tag{4.17}$$

It then follows that

$$V^{nn}_{AB} = \frac{\langle P_A|\Gamma'|P_B\rangle}{2\sqrt{E_A E_B}}. \tag{4.18}$$

The correlators entering the fits should be normalised for one staggered taste, so divided by 4. However, this cancels in practice for 2-point correlators because each propagator calculated is too small by a factor of 2. This comes from the lattice derivative used in the code, which is $\psi(x+\hat{\mu}-\psi(x-\hat{\mu})$, rather than $\frac{1}{2}\psi(x+\hat{\mu}-\psi(x-\hat{\mu})$. For an n-point correlator function, the correct normalised correlator, C_{npt} is related to the correlator calculation in the simulation, C^{sim}_{npt}, by

$$C_{npt} = \frac{2^n}{4} C^{sim}_{npt}. \tag{4.19}$$

The factors cancel for the 2-point correlators, so Equation 4.15 is correct, but the expression for the 3-point amplitude in Equation 4.18 should be replaced by

$$V^{nn}_{AB} = \frac{\langle P_A|\Gamma'|P_B\rangle}{4\sqrt{E_A E_B}}. \tag{4.20}$$

4.3 Twisted boundary conditions

Lattice QCD simulations generally impose periodic boundary conditions on the lattice's spatial directions, $\psi(k+L_\mu\hat{\mu}) = \psi(k)$ for any spatial direction μ. This means the lattice momentum is quantised so $p_\mu = n_\mu \frac{2\pi}{L_\mu}$ for integer n_μ.

The problem with quantised lattice momentum is that mesons cannot be created with arbitrary momentum. This is a limitation for simulations of momentum dependent form factors or decays at zero momentum transfer ($q^2 = 0$), which require tuning the meson momenta to get the right kinematics.

Twisted boundary conditions are defined by $\psi(k + L_\mu\hat{\mu}) = e^{i\theta_\mu}\psi(k)$ [52], where the phase θ_μ can be tuned to change the momentum p_μ by $\frac{\theta_\mu}{L_\mu}$. As the momentum should be introduced in a spatial direction, the time component $\theta_t = 0$.

A quark field, $\psi'(k)$ which satisfies twisted boundary conditions can be related to one, $\psi(k)$, with periodic boundary conditions by

$$\psi'(k) = e^{i\frac{\theta_\mu k_\mu}{L_\mu}}\psi(k). \tag{4.21}$$

Then

$$\psi(k + L_\mu\hat{\mu}) = \psi(k) \tag{4.22}$$

and

$$\psi'(k + L_\mu\hat{\mu}) = e^{i\theta_\mu k_\mu}\psi'(k). \tag{4.23}$$

To replace the fields $\psi(k)$ with $\psi(k')$ in the action requires modifying the Dirac operator, $\not{D}$, so that the action remains invariant. The naive one-link action from Equation 1.13 is

$$\mathcal{S} = \sum_k \bar{\psi}(k)[\frac{1}{2}\left\{U_\mu(k)\psi(k+\hat{\mu}) - U^\dagger(k-\mu)\psi(k-\hat{\mu})\right\} + m_q\psi(k)]. \tag{4.24}$$

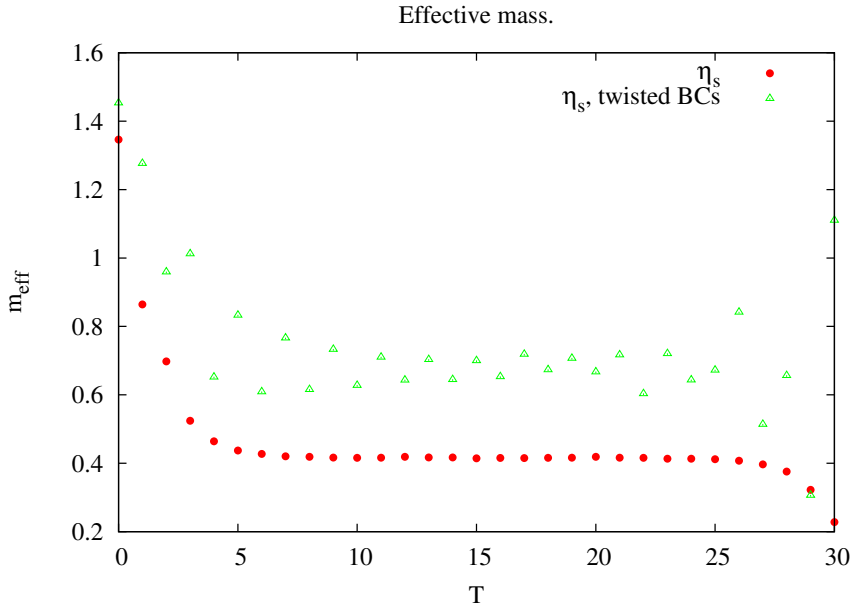

Figure 4.5: The effective mass for η_s mesons with and without twisted BCs. The red points are for an η_s at rest and the green for an η_s carrying high momentum. The use of twisted boundary conditions gives a rise in the ground state energy of the correlator.

The mass term is local and is therefore unaffected by the replacement $\psi(k) \to \psi'(k)$. The phase appearing in the one-link terms can be implemented by rephasing the gauge links by [53, 54]

$$U_\mu(k) \to e^{i\theta_\mu/L_\mu} U_\mu(k). \tag{4.25}$$

For the 3-link Naik terms which appear in the improved staggered action, the long links must be rephased by

$$U^{(3)}_\mu(k) \to e^{3i\theta_\mu/L_\mu} U^{(3)}_\mu(k). \tag{4.26}$$

Figure 4.5 shows the effect of twisted boundary conditions on the effective mass of an η_s correlator. The η_s meson is an unphysical pseudoscalar meson containing a strange quark and strange antiquark. In reality, the pseudoscalar $s\bar{s}$ mixes with light flavours $l\bar{l}$ in η and η' mesons, but the purely $s\bar{s}$ state can be extracted and studied on the lattice. The state studied in lattice QCD only includes the connected 2-point correlator.

The red circles show the effective mass for an η_s meson at rest and the green triangles the effective mass for an η_s meson carrying θ_μ. The ground state energy for the η_s meson with non-zero momentum is clearly larger than the energy at rest (which corresponds to the η_s mass). There are clear oscillations for the effective mass of the η_s carrying momentum. This is because – unlike the case for the η_s at rest – the two quark propagators are different as one of them was calculated using twisted gauge links.

Note that if $g_\theta(i,j)$ is a quark propagator with momentum $p_\mu = \theta_\mu/L_\mu$, then $g^\dagger_\theta(i,j)$ is an antiquark with momentum $-p_\mu$. A meson composed of a quark and antiquark

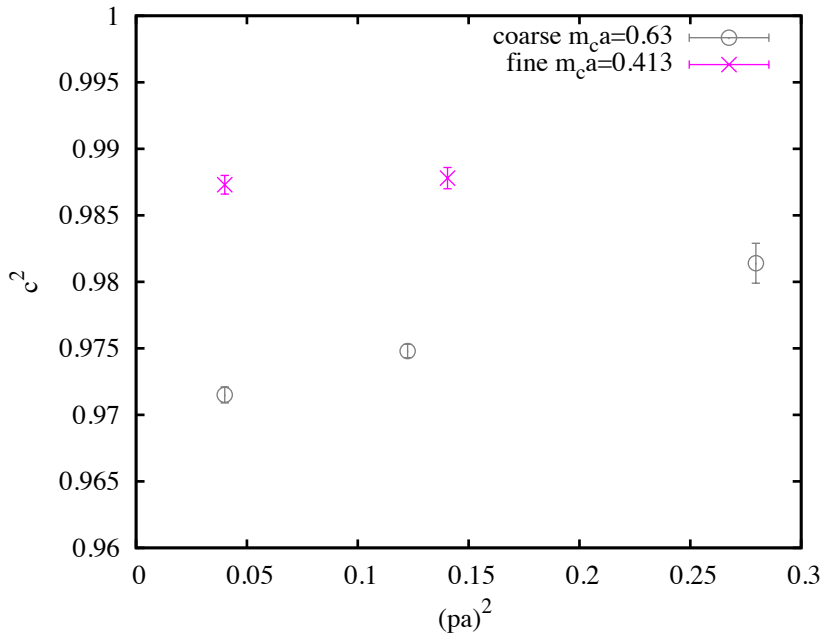

Figure 4.6: The dispersion relation for η_c mesons is checked by plotting c^2 against $(pa)^2$ on different lattice spacings.

which both carry the same θ will then have no overall momentum so its energy will just be the meson mass.

That twisted boundary conditions introduce a momentum as expected can be checked by looking at the dispersion relation. By fitting meson correlators for mesons with different momenta $\vec{p} = \theta_\mu / L$ and extracting the meson energy $E(\vec{p})$, the speed of light can be calculated as

$$c^2 = \frac{E(\vec{p})^2 - m^2}{\vec{p}^2} \tag{4.27}$$

The expectation is that $c^2 = 1$ in the continuum limit, but small discretisation effects, proportional to powers of (ap), are allowed.

The dispersion relation for η_c mesons was checked in [55] and for other mesons in [56, 57]. The speed of light extracted from η_c mesons with different momenta and on different lattice spacings in shown in Figure 4.6. Some dependence on lattice spacing and meson momentum is seen, which is a result of discretisation effects. The dependence on the momentum is much smaller on the fine lattice than on the coarse.

Figure 4.7 shows the dependence of this discretisation effect on lattice spacing, here as a function of $(m_c a)^2$. The data plotted for each configuration is the speed of light extrapolated to $(ap)^2 = 0$. The data for these ensembles depends linearly on $(m_c a)^2$ and $c^2 \to 1$ as $a \to 0$.

4.4 Operator renormalisation

Continuum and lattice meson operators are defined in different regularisation schemes. On the lattice, the finite lattice spacing between sites provides the regularisation by

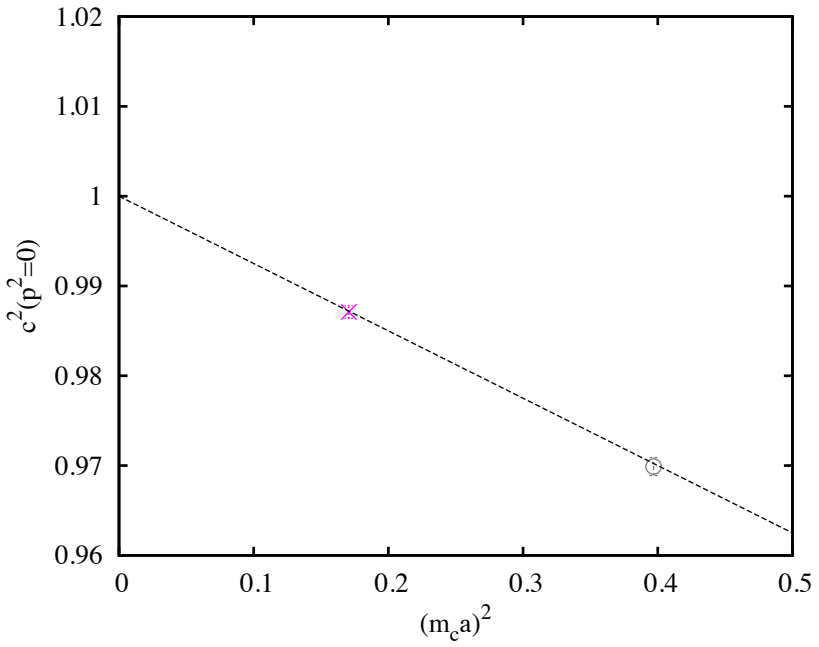

Figure 4.7: c^2 from the dispersion relation for η_c mesons and extrapolated to $(pa)^2 = 0$ for different lattice spacings and plotted against $(m_c a)^2$.

cutting off high energy states. States with $p_\mu > \pi/a_\mu$, where a_μ is the spacing in the μ direction, do not appear on the lattice. Typically, continuum matrix elements are regularised using dimensional regularisation and the $\overline{MS}$ scheme, which is not the same as the lattice scheme.

Therefore, the lattice and continuum operators can differ by a normalisation factor Z:

$$\hat{O}_{continuum} = Z\hat{O}_{lattice}. \tag{4.28}$$

The staggered action has a remnant chiral symmetry

$$\psi \to e^{i\alpha\gamma_5\otimes\gamma_5}\psi, \tag{4.29}$$

as the phase factor for $\gamma_5 \otimes \gamma_5$, $\varepsilon(i)$, anticommutes with the staggered Dirac operator, $\not{D}_{stag}$. Staggered quarks obey the PCAC relation for a conserved lattice axial current

$$\partial_\mu A^\mu = (m_1 + m_2)P, \tag{4.30}$$

where m_1 and m_2 are the valence quark masses and the pseudoscalar operator $P = \gamma_5 \otimes \gamma_5$. The combination $m_q P$ is conserved so the pseudoscalar operator $Z_P = Z_m^{-1}$, so the local pseudoscalar operator needs no renormalisation. The conserved axial current is non-local and is not the simplest lattice operator to use for an axial vector. The Z factors for the simpler operators used can be related to conserved currents and can be calculated perturbatively or non-perturbatively.

For the physical results of Chapters 5, 6 and 7, the staggered operators are normalised using a non-perturbative calculation. The resultant Z factor is combined with the lattice results before extrapolating to the continuum limit.

4.5 Physical extrapolation

4.5.1 Continuum extrapolation

Lattice QCD differs from continuum QCD in that simulations are performed at finite lattice spacing, a. Quantities calculated on the lattice depend on a and must be extrapolated to $a = 0$ before they can be compared with continuum results. Lattice data is calculated at different lattice spacings and fitted to

$$C(a) = C(0) + \sum_A c_A a^A. \tag{4.31}$$

For staggered quarks, the discretisation errors can be taken to be even powers of a [50].

4.5.2 Chiral extrapolation

The masses of the light sea quarks in a gauge ensemble with dynamical quarks are typically too high, although some gauge configurations have recently been generated with physical light sea quark masses [32]. This is because of the numerical difficulties of simulating with the up and down quarks at their physical masses. Therefore, quantities calculated on the lattice also depend on the sea quark mass. Working with different sea quark masses allows an extrapolation to the physical light quark mass to be done using chiral perturbation theory [58]. The chiral extrapolation is done simultaneously with the continuum extrapolation.

For charmonium ($c\bar{c}$ mesons), very little dependence on the sea quark masses is expected.

4.5.3 Finite size effects

The lattices used for calculations have a finite size, which is unlike the continuum because the particles simulated have to be inside this volume. To avoid significant finite size effects, the Compton wavelength of the particle has to fit in the lattice volume [19], which is satisfied for mesons if $mL > 4$, where am is the mass in lattice units and L/a is the number of lattice sites in one direction.

The lightest particle simulated in these calculations is the η_s, which has $m_{\eta_s} L \simeq 8$. The charm-strange D_s has $m_{D_s} L \simeq 24$ and charmonium $m_{\eta_c} L \simeq 36$, so finite size effects are not large for any of these simulations.

Chapter 5

The radiative decay $J/\psi \to \eta_c\gamma$

Charmonium mesons are bound states of a charm quark and a charm antiquark. The lightest charmonium state is the pseudoscalar ($J^{PC} = 0^{-+}$) η_c, which has a mass of 2980 MeV [5]. The J/ψ is the lightest vector charmonium state with a mass of 3096 MeV.

The radiative charmonium decay $J/\psi \to \eta_c$ is mediated by the electromagnetic interaction and the photon-quark coupling is described by a vector current. The decay rate depends on a nonperturbative QCD form factor, $V(q^2)$, which is a function of the momentum transfer squared between the J/ψ and η_c mesons. The vector q^μ is defined as $q^\mu = p^\mu_{J/\psi} - p^\mu_{\eta_c}$. For a physical, massless photon to be produced, $q^2 = 0$. It is simplest for one of the two mesons to be at rest and these kinematics can be obtained with momentum only in either the η_c or J/ψ. If the J/ψ meson is taken to be at rest, the spatial momentum of the η_c must be given by

$$|\vec{p}_{\eta_c}| = \frac{(m_{\eta_c} + m_{J/\psi})(m_{J/\psi} - m_{\eta_c})}{2m_{J/\psi}}. \tag{5.1}$$

The matrix element for the decay is

$$\langle \eta_c(p')|V_\mu|J/\psi(p)\rangle = \frac{2V(q^2)}{m_{J/\psi} + m_{\eta_c}}\epsilon^{\mu\alpha\beta\gamma}p'_\alpha p_\beta \varepsilon_\gamma, \tag{5.2}$$

where ε_γ is the polarisation vector of the J/ψ meson. Because of the $\epsilon^{\mu\alpha\beta\gamma}$ symbol on the right hand side, the matrix element vanishes unless the mesons' momenta, the J/ψ polarisation and the vector current are all in different directions. The normalisation of Equation 5.2 takes account of the charm quark's electric charge and includes a factor of 2 because the photon current interacts with only one of the two charm quarks in the lattice simulation.

The process decay rate is given by

$$\Gamma_{J/\psi\to\eta_c\gamma} = \alpha_{QED}\frac{64|\vec{q}|^3}{27(m_{J/\psi} + m_{\eta_c})^2}|V(0)|^2. \tag{5.3}$$

The decay rate only depends on the form factor at $q^2 = 0$, $\alpha_{QED} = 1/137$ and $\vec{q}$ is the

spatial momentum of the η_c in the J/ψ rest frame.

The decay rate is calculated using $|\vec{q}| = 113.8(1.1)$ MeV, extracted from the continuum meson masses. The lattice input to the decay rate is the nonperturbative form factor $V(0)$.

Using the appropriate 2-point and 3-point functions for the η_c and J/ψ, mesons the quantity $V(0)/Z$ can be extracted, where Z is a renormalisation factor for the lattice vector current used. Z itself can also be calculated non-perturbatively using lattice 3-point correlators.

The first section of this chapter describes the sequential-source technique used to generate the extended propagators used to construct 3-point correlators on the lattice. Then the lattice calculations of the vector form factor, $V(0)/Z$, and the renormalisation factor, Z, are discussed before looking at the final decay rate obtained after extrapolating to the continuum.

5.1 Extended propagators

On the lattice, the correlation function for $J/\psi \to \eta_c\gamma$ is a 3-point correlation function, shown in Figure 5.1:

$$\langle\bar{\psi}(t_0)\gamma_5\psi(t_0)\bar{\psi}(t)\gamma_\mu\psi(t)\bar{\psi}(T)\gamma_\nu\psi(T)\rangle, \tag{5.4}$$

in which an η_c meson is created at the source time, t_0, there is an electromagnetic vector current inserted at t and the J/ψ is destroyed at T, where the timeslices on which each operator is placed satisfy $T > t > t_0$. For an operator at time t, there is an implicit sum over the spatial sites on that timeslice.

Converting to staggered fields and Wick contracting them in the correlation function gives it terms of propagators

$$\sum_{ijk} \mathrm{Tr}[\gamma_5\Omega(i)g(i,j')\Omega^\dagger(j')\gamma_\mu\Omega(j)g(j,k')\Omega^\dagger(k')\Omega(k)\gamma_\nu g(k,i')\Omega^\dagger(i')], \tag{5.5}$$

where lattice sites i and i' allow for some point-splitting and are on timeslice t_0, j and j' are at time T and k and k' at t.

To make a correlation function with three propagators, extended propagators are calculated using a sequential source technique.

Propagator 1 in Figure 5.1 is generated from a random wall source, $\eta(i)$, with non-zero values at t_0. The result of this inversion is $g(j) = \sum_i g(i,j)\eta(i)$. The extended propagator is generated from a source which is $g(j)$ with j on timeslice T. This inversion results in $g_{ext}(k) = \sum_{ij} g(j,k)\sum_i g(i,j)\eta(i)$, where site j is at time T and site i at t_0. $g_{ext}(k)$ is then the product of the two propagators $g(j,k)$ and $g(i,j)$ and describes a quark propagating from t_0 to T and then a propagation from T to t. By including the appropriate staggered operator, a Dirac γ operator can be placed at

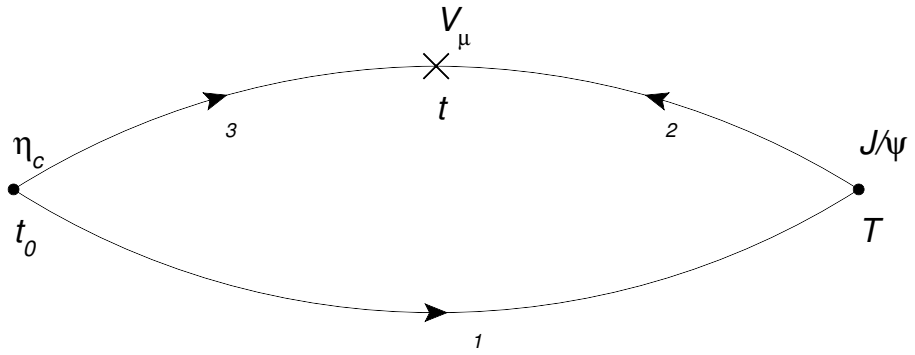

Figure 5.1: Diagram of the propagators in the charmonium 3-point decay correlator. The η_c and J/ψ mesons are created at times 0 and T and a vector current is inserted at an intermediate time t. In the simulation, an extended propagator is made using propagator 1 as the source for propagator 2.

Ensemble	N_{confs}	r_1/a	$\mu_0 am_l$	$\mu_0 am_s$	$L_s \times L_t$	δx_l	δx_s
1	2088	2.647(3)	0.005	0.05	24×64	0.11	0.43
2	2259	2.618(3)	0.01	0.05	20×64	0.25	0.43
3	1911	3.699(3)	0.0031	0.062	28×96	0.20	0.19

Table 5.1: MILC 2+1 asqtad ensembles used for the $J/\psi \to \eta_c\gamma$ calculation. The number of configurations is given in the 2nd column. The 3rd column quotes the MILC Collaboration's determination of r_1/a used to determine the lattice spacing. The other columns give the sea quark masses and the number of lattice sites for each ensembles. Ensembles 1 and 2 differ by the light sea quark mass and are called 'coarse' while ensemble 3 is 'fine'. For each configurations, 4 time sources are used.

T. Similarly, momentum can be carried by propagator 2 by implementing twisted boundary conditions in the conjugate gradient inversion used to obtain $g_{ext}(k)$.

5.2 Lattice calculation setup

The form factor, $V(q^2)$, for the decay $J/\psi \to \eta_c\gamma$ was calculated on three different ensembles of gauge configurations generated by the MILC Collaboration, which are in Table 5.1. These configurations include the effects of $N_f = 2 + 1$ dynamical sea quarks simulated with the asqtad staggered action. Ensembles 1 and 2 are 'coarse' and differ in the light sea quark mass and spatial volume, while ensemble 3 has a finer lattice spacing and approximately the same physical volume and strange to light sea quark ratio as ensemble 2. The quantity r_1/a has been measured by the MILC Collaboration [35] for these ensembles and is a measure of the lattice spacing. The valence quarks are simulated using the HISQ action which, as discussed in Chapter 2, has small discretisation effects for charm quarks.

5.2.1 Staggered operators

The 3-point correlation function contains a pseudoscalar and two vector operators, but there is some freedom over which lattice operators are used in the simulation. If staggered fermions are used, the overall taste of the correlation function must be $\Gamma = 1$. This rules out using local operators for all three operators in the 3-point function. It is desirable to use a little point-splitting as possible because point-split operators tend to be more noisy.

A possible choice is to use a local vector $\gamma_\mu \otimes \gamma_\mu$ for the electromagnetic vector current, a 1-link $\gamma_\nu \otimes \gamma_\nu\gamma_\rho$ vector for the J/ψ and a local $\gamma_t\gamma_5 \otimes \gamma_t\gamma_5$ for the η_c. This combination has the right overall taste if μ, ν and ρ are all orthogonal spatial directions. The 'non-Goldstone' $\gamma_t\gamma_5 \otimes \gamma_t\gamma_5$ operator couples to states with $J^{PC} = 0^{-+}$ so can be used for the η_c. The 3-point correlator with these operators only includes one link of point-splitting.

An alternative choice is to use $\gamma_5 \otimes \gamma_5$ for the η_c and $\gamma_t\gamma_\nu \otimes \gamma_t\gamma_\nu\gamma_\rho$ for the J/ψ. This setup uses the same local vector operator for the electromagnetic vector current, which is helpful because this is the operator whose normalisation matters for the transition matrix element $\langle J/\psi|V_\mu|\eta_c\rangle$. The same renormalisation factor, Z, is then required for either setup and both calculations can be made with the same Z.

The set of operators containing the $\gamma_5 \otimes \gamma_5$ pseudoscalar operator is called the Goldstone η_c setup and the one with $\gamma_t\gamma_5 \otimes \gamma_t\gamma_5$ for the η_c is the non-Goldstone η_c setup.

The first step is to calculate 2-point correlators for both the η_c and J/ψ and extract the mesons' masses. These masses are then used, along with Equation 5.1, to calculate the momentum needed to reach $q^2 = 0$.

The momentum is included in the η_c mesons by applying twisted boundary conditions to propagator 3 in Figure 5.1. The direction of the momentum is chosen orthogonal to the J/ψ polarisation and the vector current. This propagator is combined with the extended propagator and the 3-point correlator is fitted as a function of t and T.

Using the relativistic normalisation and remembering the J/ψ is at rest so its energy is just the particle mass, the matrix element $\langle\eta_c|V_\mu|J/\psi\rangle$ is related to the fit parameter V_{00} using Equation 4.20 by

$$\langle\eta_c|V_\mu|J/\psi\rangle = 4Z\sqrt{m_{J/\psi}E_{\eta_c}}V_{00}, \tag{5.6}$$

where the vector current renormalisation factor is also included. It follows from Equation 5.2 that

$$V(0)/Z = \frac{m_{J/\psi} + m_{\eta_c}}{2m_{J/\psi}p_{\eta_c}}4\sqrt{m_{J/\psi}E_{\eta_c}}V_{00}. \tag{5.7}$$

The form factor is obtained using a simultaneous fit to the 3-point correlator and the 2-point correlators for the J/ψ, η_c carrying momentum p_{η_c} given by Equation 5.1 and η_c at rest. The fit parameters for the η_c at rest are not shared with the 3-point function

at $q^2 = 0$ and it is only included in the simultaneous fit to extract m_{η_c} which is needed to extract the form factor for the matrix element.

5.3 Lattice results for $V(0)/Z$

As noted before, the lattice calculation can be done with either the Goldstone η_c or non-Goldstone η_c set of staggered operators. As the operators couple to the same states and only differ by taste, they should agree in the continuum limit. With HISQ, the taste splittings are small and the results with these sets of operators agree at the lattices spacings used in the simulations.

In the 3-point simulation, the J/ψ polarisation, V^μ direction and η_c momentum must all be in orthogonal spatial directions. Similarly, because the staggered action is used, the J/ψ polarisation, V^μ direction and point-split direction in the J/ψ operator must all be different spatial directions. It follows that the η_c momentum must be in the same direction as the point-split link in the J/ψ vector operator. In the simulations, the directions are chosen such that the J/ψ is polarised in the x direction, the η_c has momentum in the y direction and the electromagnetic vector current is in the z direction.

5.3.1 Goldstone η_c setup

For the Goldstone η_c setup, the η_c 2-point correlator is given by

$$C_{\eta_c,2pt}(0,t) = \sum_{i,j} \mathrm{Tr}\left[g(i,j)g_\theta^\dagger(i,j)\right]. \tag{5.8}$$

Including the explicit phase factor for the $\gamma_t\gamma_x \otimes \gamma_t\gamma_x\gamma_y$ operator, the J/ψ 2-point function is

$$C_{J/\psi,2pt}(0,t) = \sum_{i,j}(-1)^{i_y+i_t}(-1)^{j_y+j_t} \times \mathrm{Tr}\left[g(i,j)(g^\dagger(i\pm\hat{y},j\pm\hat{y})\right]. \tag{5.9}$$

In the 3-point correlator, the vector current must be in the z direction. It is

$$C_{3pt}(0,t,T) = \sum_{i,j,k}(-1)^{k_x+k_z}(-1)^{j_z} \times \mathrm{Tr}\left[g(k,j)g(i,k\pm\hat{y})g_\theta^\dagger(i,j)\right]. \tag{5.10}$$

In all of the above expressions, i is a site on the source timeslice ($i_t = 0$), j is a site at time $j_t = t$ and k a site at $k_t = T$. The point-split $i \pm \hat{y}$ implies an average over the forward and backward directions.

The lattice input parameters and fit outputs are tabulated in Tables 5.2 and 5.3, from fits with 6 non-oscillating and 5 oscillating exponential terms. The input parameters for the charm inversions, $m_c a$ and ε_N are given and θ is the twist angle needed for the η_c to tune the kinematics to $q^2 = 0$. Table 5.2 gives the ground state energies

Ens.	am_c	ε_N	$aM_{J/\psi}$	aM_{η_c}	θ	$aE^{\theta}_{\eta_c}$	a^2q^2
1	0.622	-0.221	1.86084(10)	1.79116(4)	1.6410	1.79243(4)	$1(4) \times 10^{-5}$
2	0.63	-0.226	1.87972(12)	1.80842(7)	1.4007	1.81023(5)	$-7(1) \times 10^{-5}$
	0.63	-0.226	1.87962(14)	1.80839(8)	1.3880	1.81019(4)	$1(5) \times 10^{-5}$
3	0.413	-0.107	1.32905(9)	1.28046(3)	1.3327	1.28133(3)	$6(4) \times 10^{-5}$

Table 5.2: Results from fits of the 2-point correlators using the Goldstone η_c set of lattice operators. The masses of the J/ψ and η_c mesons at rest are used to tune the value of θ such that $q^2 = 0$ for the decay. The energy of the η_c meson carrying this momentum is used to check how close a^2q^2 in the final column is to 0. Although all this data can be extracted from the 2-point correlators alone, the data is from a simultaneous fit to the 2-point and 3-point correlators.

Ensemble	m_ca	a^2q^2	T values	V^{nn}_{00}	$V(0)/Z$	Z
1	0.622	$1(4) \times 10^{-5}$	15,18,21	0.0362(2)	1.900(11)	0.9896(11)
2	0.63	$-7(1) \times 10^{-5}$	15,18,21	0.0368(2)	1.897(12)	0.9894(8)
	0.63	$1(5) \times 10^{-5}$	15,18,21	0.0362(4)	1.883(20)	0.9894(8)
3	0.413	$6(4) \times 10^{-5}$	20,23,26,29	0.0348(2)	1.876(8)	1.0049(10)

Table 5.3: Fit results for the $J/\psi \to \eta_c\gamma$ form factor using the Goldstone η_c setup of staggered operators. The data is obtained from a simultaneous fit to the 2-point and 3-point correlators, where the meson masses and η_c energy at finite momentum are needed to extracted $V(0)/Z$. The Z factor used is obtained from the non-perturbative 3-point method described later in this chapter. Two calculations were made on ensemble 2 to check the sensitivity of $V(0)/Z$ on mistunings of a^2q^2.

for the η_c with and without the tuned momentum and the J/ψ mesons. This data can be extracted from fitting just the 2-point correlators, but the results shown are taken from the full simultaneous fit to the 2-point and 3-point correlators. From the energies of the states in the 3-point correlator, the values of a^2q^2 can be calculated and are given in the final column of Table 5.2. This measures how close the kinematics are to the physical $q^2 = 0$.

The data for the 3-point amplitude is shown in Table 5.3, where $m_c a$ and a^2q^2 are repeated for comparison – the vector form factor calculated should be at $q^2 = 0$. Odd and even values of T are used to help fit the oscillating contributions. The Z factor corresponding to each ensemble is given in the last column of Table 5.3. Looking at the values of $V(0)/Z$ in Table 5.3 shows there is little dependence on lattice spacing or sea quark masses.

The two calculations on Ensemble 2 differ in the η_c momentum and can be compared to see the effect of mistunings away from $q^2 = 0$. The form factor results for these two cases agree within their statistical errors, so there is no problem caused by the tuning of q^2.

In the fits, the priors for the ground states are taken from the correlator effective masses. The priors for the splittings between successive excited states is equivalent to 600(300) MeV for each ensemble, although the values used differ on the coarse and fine ensembles because the fit is to aE. The priors for the 2-point and 3-point amplitudes (a_i and V_{ij}) are all taken to be zero with prior widths of 0.5 for the 2-point amplitudes and 0.25 for the 3-point. The 3-point amplitudes are expected to be lower than the 2-point amplitudes because their normalisation contains both meson masses.

To remove some of the effects from excited states at low t values, the 3-point correlator data is fitted in a range t_{min} to $T - t_{min}$ where $t_{min} = 6$. The 2-point data is fitted in the range t_{min} to $L_t - t_{min}$.

Ignoring the excited and oscillating states, the η_c 2-point correlator is dominated by

$$C_{\eta_c,2pt}(t) = a^2_{\eta_c} e^{-E_{\eta_c} t} \tag{5.11}$$

and the J/ψ by

$$C_{J/\psi_c,2pt}(t) = a^2_{J/\psi} e^{-E_{J/\psi} t} \tag{5.12}$$

while the 3-point correlator with just the ground states is

$$C_{3pt}(t,T) = a_{\eta_c} a_{J/\psi} V_{00} e^{-E_{\eta_c} t} e^{-E_{J/\psi}(T-t)}. \tag{5.13}$$

Far away from $t = 0$ and $t = T$, the ground state contributions will be dominant and the ratio

$$\frac{C_{3pt}(t,T)}{C_{\eta_c,2pt}(t) C_{J/\psi,2pt}(T-t)} \to \frac{V_{00}}{a_{\eta_c} a_{J/\psi}} \tag{5.14}$$

should plateau. This ratio is shown in Figure 5.2 for all T values calculated on the fine ensemble. The shaded band is the ratio of the fit parameters where the plateau is

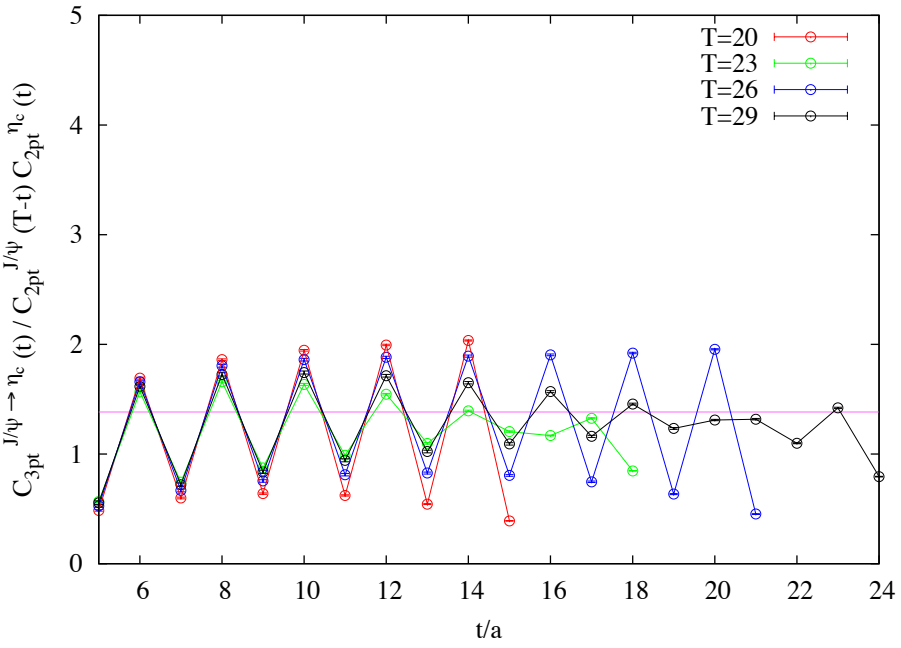

Figure 5.2: The ratio of the 3-point to 2-point correlators for ensemble 3. All values of $T = 20, 23, 26, 29$ are shown with the range t_{min} to $T - t_{min}$ used in the fit shown on the plot. The shaded band is the ratio of fitted parameters $V_{00}/a_0 b_0$ where the ratio should plateau. The oscillations for staggered quarks are clear. This data is for the Goldstone η_c set of staggered operators.

expected. On the plot, only the times included in the fit are shown – this is to remove the largest oscillations that appear at either end of the fitted range of t.

Despite the oscillations evident in Figure 5.2, a plateau can be seen in the data and the fit lies where the plot plateaus. The multiexponential fit is able to take account of the oscillations and excited states and accurately determines the fit parameter V_{00}.

5.3.2 Non-Goldstone η_c setup

In the non-Goldstone η_c setup, the 3-point correlator is given by

$$C_{3pt}(0,t,T) = \sum_{i,j,k} (-1)^{i_x+i_y+i_z} (-1)^{k_y} (-1)^{j_z} \times \mathrm{Tr}\left[g(k,j) g(i,k \pm \hat{y}) g_\theta^\dagger(i,j) \right], \quad (5.15)$$

with corresponding 2-point functions are

$$C_{\eta_c,2pt}(0,t) = \sum_{i,j} (-1)^{i_x+i_y+i_z} (-1)^{j_x+j_y+j_z} \times \mathrm{Tr}\left[g(i,j) g_\theta^\dagger(i,j) \right] \quad (5.16)$$

and

$$C_{J/\psi,2pt}(0,t) = \sum_{i,j} (-1)^{i_x+i_z+i_t} (-1)^{j_x+j_z+j_t} \times \mathrm{Tr}\left[g(i,j) (g^\dagger(i \pm \hat{y}, j \pm \hat{y}) \right]. \quad (5.17)$$

Again, the sites i, j and k are on timeslices such that $i_t = 0$, $j_t = t$ and $k_t = T$

Ens.	am_c	ε_N	$aM_{J/\psi}$	aM_{η_c}	θ	$aE^{\theta}_{\eta_c}$	a^2q^2
1	0.622	-0.221	1.86035(15)	1.79621(4)	1.5120	1.79725(4)	$3(5) \times 10^{-5}$
2	0.63	-0.226	1.87887(13)	1.81369(6)	1.2814	1.81480(5)	$0(4) \times 10^{-5}$
	0.66	-0.244	1.93604(15)	1.87254(6)	1.2490	1.87355(6)	$1(5) \times 10^{-5}$
3	0.413	-0.107	1.32904(11)	1.28160(4)	1.3116	1.28243(4)	$-2(1) \times 10^{-5}$

Table 5.4: Results from fits of the 2-point correlators using the non-Goldstone η_c set of lattice operators. The masses of the J/ψ and η_c mesons at rest are used to tune the value of θ such that $q^2 = 0$ for the decay. The energy of the η_c meson carrying this momentum is used to check how close a^2q^2 in the final column is to 0. Although all this data can be extracted from the 2-point correlators alone, the data is from a simultaneous fit to the 2-point and 3-point correlators.

Ensemble	m_ca	a^2q^2	T values	V^{nn}_{00}	$V(0)/Z$	Z
1	0.622	$3(5) \times 10^{-5}$	15,18,21	0.0338(6)	1.925(35)	0.9896(11)
2	0.63	$0(4) \times 10^{-5}$	15,18,21	0.0334(8)	1.896(45)	0.9894(8)
	0.66	$1(5) \times 10^{-5}$	15,18,21	0.0322(8)	1.934(42)	0.9863(17)
3	0.413	$-2(1) \times 10^{-5}$	19,20,23,26	0.0342(4)	1.872(21)	1.0049(10)

Table 5.5: Fit results for the $J/\psi \to \eta_c\gamma$ form factor using the Goldstone η_c setup of staggered operators. The data is obtained from a simultaneous fit to the 2-point and 3-point correlators, where the meson masses and η_c energy at finite momentum are needed to extracted $V(0)/Z$. The Z factor used is obtained from the non-perturbative 3-point method described later in this chapter. Two calculations were made on ensemble 2 to check the sensitivity of $V(0)/Z$ on mistunings of m_ca.

with $i \pm \hat{y}$ indicating an average over the forward and backward point-split directions.

Results for the non-Goldstone η_c setup are shown in Tables 5.4 and 5.5. As for the Goldstone η_c setup, the data is for a simultaneous multiexponential fit with 6 exponentials and 5 oscillating exponentials. For these fits, the oscillations and excited states were suppressed using $t_{min} = 4$ for the coarse ensembles and $t_{min} = 5$ for the fine. Note that the values of T used differ slightly.

The two sets of data for ensemble 2 differ by deliberate mistuning of the charm mass. The correctly tuned charm mass for this ensemble is 0.63, but the form factor agrees within the statistical errors for the two. This means that the lattice result of this calculation – the form factor at $q^2 = 0$ – is not hugely sensitive to the charm quark mass or the hyperfine splitting on the lattice.

Figure 5.3 shows the ratio of the 3-point correlator to the 2-point correlators. Again, a plateau is expected far from the ends of the time range where the η_c and J/ψ mesons are. The ratio of fit parameters is shown in the shaded band. Note that the value of the plateau is not the same as for Figure 5.2. Although the 3-point amplitude is roughly the same for the two setups, the 2-point amplitudes are not.

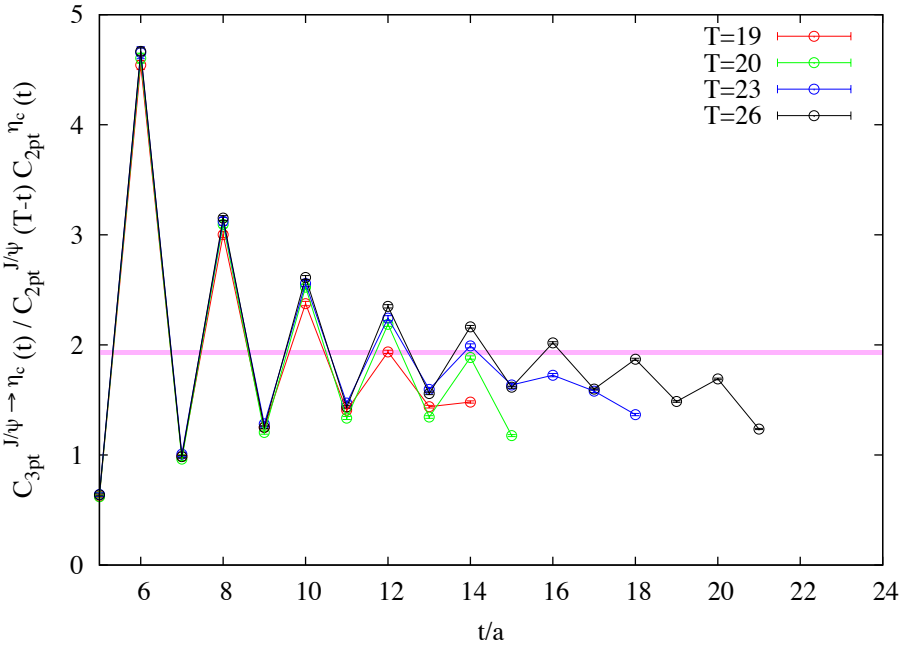

Figure 5.3: The ratio of the 3-point to 2-point correlators for ensemble 3. All values of $T = 19, 20, 23, 26$ are shown with the range t_{min} to $T - t_{min}$ used in the fit shown on the plot. The shaded band is the ratio of fitted parameters $V_{00}/a_0 b_0$ where the ratio should plateau. The oscillations for staggered quarks are clear. This data is for the non-Goldstone η_c set of staggered operators.

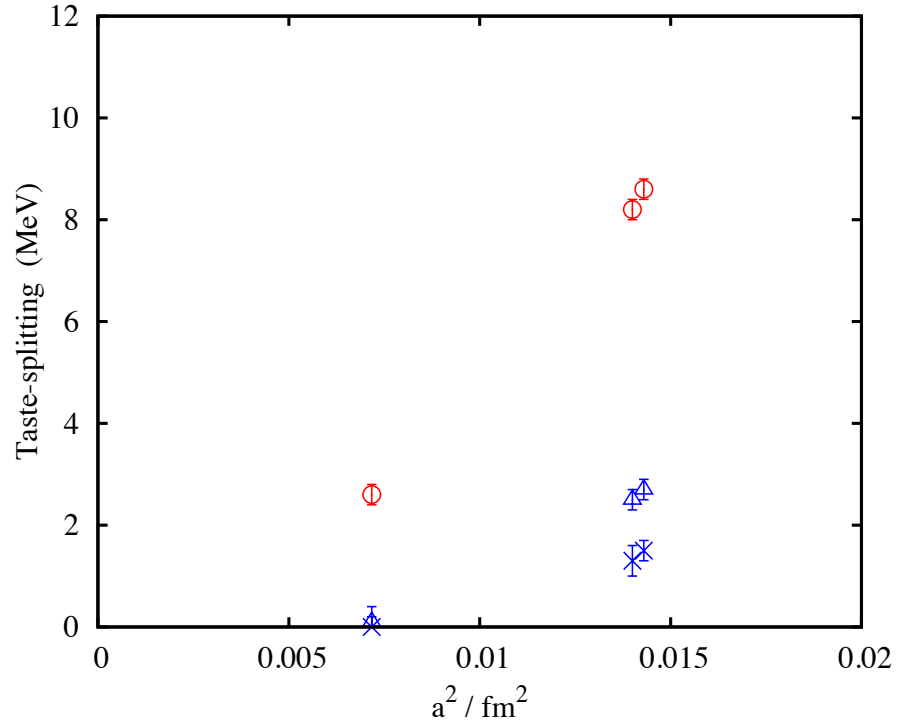

Figure 5.4: Taste-splittings for charmonium in MeV as a function of a^2. The red circles are the splitting between $\gamma_5 \otimes \gamma_5$ and $\gamma_5\gamma_t \otimes \gamma_5\gamma_t$ tastes of η_c mesons. The blue crosses are J/ψ splittings between the 1-link $\gamma_\mu \otimes \gamma_\mu\gamma_\nu$ and local $\gamma_\mu \otimes \gamma_\mu$ operators and the blue triangles between the $\gamma_\mu\gamma_t \otimes \gamma_\mu\gamma_\nu\gamma_t$ and $\gamma_\mu \otimes \gamma_\mu$ operators. The taste-splittings are very small (the charmonium mesons have masses $\simeq$ 3000MeV) and vanish with a^2.

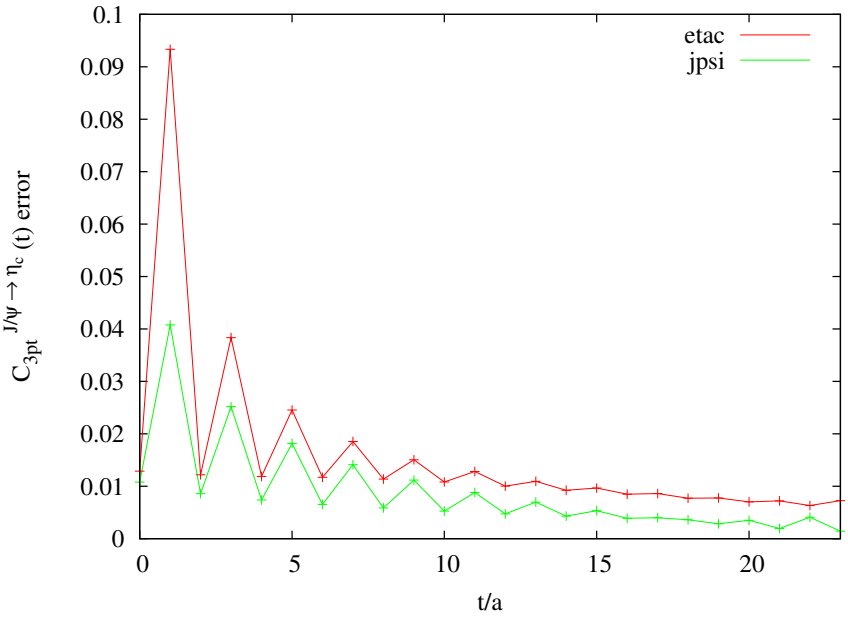

Figure 5.5: Comparison of statistical errors for the 2 staggered operator setups. The relative error of the averaged correlator for $T = 23$ on the fine ensemble is plotted against t. The labels 'etac' and 'jpsi' indicate which of the staggered operators contains a γ_t. The 'jpsi' (Goldstone η_c) data has smaller statistical errors in the 3-point correlator data. This is consistent with the smaller errors on the obtained $V(0)/Z$ for the Goldstone η_c data.

5.3.3 Charmonium taste splittings

Comparing the masses for the J/ψ and η_c mesons in Tables 5.2 and 5.4 shows the taste-splittings for charmonium. Figure 5.4 shows the taste-splittings in charmonium between the $\gamma_5 \otimes \gamma_5$ and $\gamma_5\gamma_t \otimes \gamma_5\gamma_t$ η_c mesons with red circles. The J/ψ splittings are between the $\gamma_\mu \otimes \gamma_\mu\gamma_\nu$ and local $\gamma_\mu \otimes \gamma_\mu$ operators, which are shown with blue crosses, and the $\gamma_\mu\gamma_t \otimes \gamma_\mu\gamma_\nu\gamma_t$ and $\gamma_\mu \otimes \gamma_\mu$, plotted with blue triangles. The local J/ψ is lighter than the 1-link mesons and was studied in [55].

The mass differences fall with a^2 and are less than 10 MeV even on the coarse ensembles.

From Tables 5.3 and 5.5, the errors for the Goldstone η_c setup are a little lower. This comes from the statistical errors for the 3-point correlator data. In Figure 5.5, the relative error of the 3-point correlator averaged over the fine ensemble is plotted as a function of t for the Goldstone η_c and non-Goldstone η_c setup. The data plotted is the 3-point correlator for $T = 23$ for each of the setups. The data points are labelled 'etac' and 'jpsi' to indicate which meson's operator contains the γ_t and the statistical errors are smaller for the Goldstone η_c setup in which the J/ψ operator contains γ_t.

At rest, the Goldstone η_c contains no oscillations, whilst the non-Goldstone does. In these kinematics, there is an oscillation in the Goldstone η_c but it is very small for this momentum.

5.4 Z factor

The other part of the calculation is to normalise the operator used for the $J/\psi \to \eta_c\gamma$ transition. The operator that needs to be normalised is the local vector. Vector operators can be normalised using a symmetric pseudoscalar to pseudoscalar 3-point function [56].

The general form for a decay from a pseudoscalar P' with momentum p' to a pseudoscalar P with momentum p is given by

$$\langle P(p)|V_\mu|P'(p')\rangle = f_+(q^2)\left[p_\mu + p'_\mu - \frac{m'^2_P - m^2_P}{q^2}q_\mu\right] + f_0(q^2)\frac{m'^2_P - m^2_P}{q^2}q_\mu, \qquad (5.18)$$

where $f_0(q^2)$ is the scalar form factor, $f_+(q^2)$ is the vector form factor and they obey $f_0(0) = f_+(0) = 1$.

For identical charmed pseudoscalar mesons, P_c at rest, Equation 5.18 simplifies considerably. The terms proportional to $m'^2_P - m^2_P$ vanish for identical mesons, as does $p_\mu + p'_\mu$ for $\mu \neq t$ if they are at rest. The temporal vector matrix element is then

$$\langle P_c|V_t|P_c\rangle = 2m_{P_c}f_+(0). \qquad (5.19)$$

This would be equal to $2m_{P_c}$ if the vector current V_t was a conserved current. The local vector used is not a conserved current, so it needs to be multiplied by a renormalisation factor, Z, such that

$$Z\langle P_c|V_t|P_c\rangle = 2m_{P_c}. \qquad (5.20)$$

To create identical mesons on either side of the 3-point function means using the same operator for both. Using only staggered quarks, these two operators will then have the same taste and the overall taste of the correlation function will be the taste of the vector operator. This means only the taste-singlet vector $\gamma_\mu \otimes 1$ can be normalised in this way using only staggered fermions.

The vector operator used for $J/\psi \to \eta_c\gamma$ is the local one $\gamma_\mu \otimes \gamma_\mu$ and this must be normalised using a non-staggered quark as the spectator quark. The aim of the calculation is to normalise the staggered-staggered current, so the details of the spectator quark are unimportant. Provided it retains spin components and has no doubling, the action and indeed the mass used for the spectator quark should not affect the normalisation beyond possible discretisation effects. Staggered currents are normalised in [59] using a clover spectator quark.

It is convenient to use non-relativistic QCD (NRQCD) for the spectator quark using the NRQCD evolution code used for B spectrum calculations in [60]. To combine staggered and NRQCD propagators, the staggered propagators have to be converted to naive 4-component quarks by the staggering transformation:

$$G(i,j) = \Omega(i)g(i,j)\Omega^\dagger(j), \qquad (5.21)$$

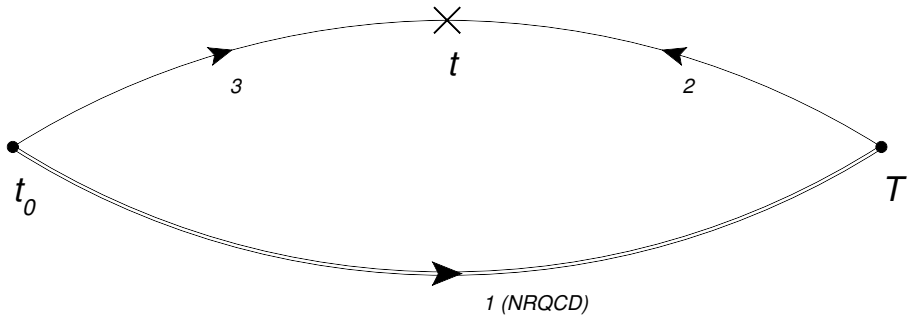

Figure 5.6: A 3-point correlator in which the spectator quark (labelled propagator 1) is a heavy NRQCD propagator. An NRQCD-HISQ meson is created at time $t_0 = 0$, there is a Dirac γ matrix inserted at t and the meson is destroyed at time T. The staggered propagators (2 and 3) have the same mass for the symmetric pseudoscalar to pseudoscalar transition.

where $G(i,j)$ is a 4-component naive propagator and $g(i,j)$ a staggered propagator.

A staggered-NRQCD 2-point correlator can be made as [61]

$$C_{2pt}(0,t) = \sum_{i,j} \mathrm{Tr}\left[G_{NRQCD}(i,j)\Omega(j)g^\dagger(i,j)\Omega^\dagger(i)\right], \tag{5.22}$$

where, as before, $i_t = 0$ and $j_t = t$. Now $G_{NRQCD}(i,j)$ is an NRQCD propagator and $g(i,j)$ a HISQ propagator. The trace is over colour and spin, but the HISQ propagator has no spin dependence and the Ω matrices no colour. It follows that $g^\dagger(i,j)$ commutes with $\Omega^\dagger(i)$ and can be taken out of the spin trace so

$$C_{2pt}(0,t) = \sum_{i,j} \mathrm{Tr_c}\left\{\mathrm{Tr_s}\left[G_{NRQCD}(i,j)\Omega(j)\Omega^\dagger(i)\right]g^\dagger(i,j)\right\}. \tag{5.23}$$

$\mathrm{Tr_c}$ denotes the trace over colours and $\mathrm{Tr_s}$ the trace over spins. In practice, this can be done by applying the Ω matrices at the source and sink of the NRQCD propagator.

This can be extended to 3-point functions, where there will be an NRQCD propagator and γ matrices in both the spin and colour traces and two staggered propagators which are only in the colour trace. The 3-point function needed to extract the local staggered $\gamma_\mu \otimes \gamma_\mu$ normalisation has the NRQCD spectator quark propagating between times $t = 0$ and $t = T$, a HISQ propagator from 0 to t, where there is a local vector current and another HISQ propagator from time t to T. The local $\gamma_t \otimes \gamma_t$ operator inserted at t has non-singlet taste γ_t, which also appears in the spin trace. The 3-point correlator for this is shown in Figure 5.6, where the double line for propagator 1 indicates a heavy NRQCD propagator. The correlator is given by

$$\begin{aligned} C_{3pt}(0,t,T) = &\sum_{i,j,k} (-1)^{k_x+k_y+k_z+k_t}(-1)^{j_t} \\ &\times \mathrm{Tr_c}\left\{\mathrm{Tr_s}\left[\gamma_t\Omega^\dagger(i)G_{NRQCD}(i,k)\Omega(k)\right]g(k,j)g^\dagger(i,j)\right\}, \end{aligned} \tag{5.24}$$

Ens.	N_{confs}	T values	am_h	am_c	ϵ	aE_{P_c}	V_{00}	Z
1	450	20,21	2.0	0.622	-0.221	0.9630(2)	1.0104(12)	0.9896(11)
2	408	20,21,24	2.8	0.63	-0.226	1.0239(2)	1.0220(10)	0.9784(9)
		20,21,24	2.0	0.63	-0.226	0.9719(2)	1.0106(8)	0.9894(8)
		20,21	1.5	0.63	-0.226	0.9311(3)	1.0026(14)	0.9974(14)
		20,21	2.0	0.66	-0.244	0.9994(3)	1.0138(18)	0.9863(17)
3	322	24,25,30	2.0	0.413	-0.107	0.6454(2)	0.9966(14)	1.0033(14)
		24,25,30	1.5	0.413	-0.107	0.5939(2)	0.9950(10)	1.0049(10)

Table 5.6: Simulation data for the local vector Z factor. The charm masses for each ensemble are the same ones as used in the $J/\psi \to \eta_c\gamma$ calculation, including the mistuned $am_c = 0.66$ on ensemble 2 used to test for the effects of slightly mistuning the charm quark mass. The number of configurations used is not the full ensemble used for $J/\psi \to \eta_c\gamma$ and 4 time sources were used for each configuration on all of these ensembles. The 3-point correlators are calculated for odd and even values of T to help separate the oscillating and non-oscillating states. The Z factor is obtained as the inverse of the fit parameter V_{00}, as $V_{00} = 1$ for the correctly normalised current.

with $i_t = 0$, $j_t = t$ and $k_t = T$. As NRQCD has spin, the trace over spin in the above equation is not trivial.

To make NRQCD-HISQ correlators, NRQCD propagators are generated with the same random noise vector at the source as for HISQ, $\eta(i)$ defined on the source timeslice. This wall source is multiplied by the staggering transformation $\Omega^\dagger(i)$ and the NRQCD evolution is done to obtain $\tilde{G}_{NRQCD}(k) = \sum_i G_{NRQCD}(i,k)\Omega^\dagger(i)\eta(i)$.

The source for the HISQ inversion to make the extended propagator between T and t is then

$$(-1)^{k_x+k_y+k_z+k_t} \times \mathrm{Tr_s}\left[\gamma_t \tilde{G}_{NRQCD}(k)\Omega(k)\right] \tag{5.25}$$

where the trace over spin is possible because all the quantities with spin dependence (the NRQCD propagator, the Ω transformations and the stray γ_t) can be included.

The sequential source technique can be checked by allowing the extended propagator to propagate back to the source timeslice and combining it with the random wall source. To return a pseudoscalar 2-point function, the factor of γ_t which is coming from the vector current insertion must be omitted, but this still serves as a useful check of doing the spin trace in the middle of the calculation.

The results for the vector current renormalisation are tabulated in Table 5.6. The ensembles of gauge configurations used were the same as for the $J/\psi \to \eta_c\gamma$ decay, but not as many configurations were used. The number N_{confs} is given in Table 5.6 along with the values of T and the input masses of the HISQ charm quark and the NRQCD heavy quark. The NRQCD masses need not, and do not, correspond to a physical heavy quark (NRQCD is usually used to simulate b quarks). On ensembles 2 and 3, the NRQCD quark mass, am_h, was varied to check for dependence of the Z factor on the spectator quark mass. Some dependence was observed on the coarse ensemble, but much less on the fine. This indicates a sensitivity to the NRQCD quark mass which is a

discretisation effect. The values of $am_h = 2.0$ on the coarse and $am_h = 1.5$ on the fine correspond to around the same physical quark mass and are used for Z. Systematic errors from the current normalisation can be checked by using the Z values obtained with heavier NRQCD quark masses, but they do not change the results for $V(0)$.

On ensemble 2, the effect of a slight mistuning of the charm mass was investigated, which makes a very small difference to Z. The Z factor is the same on ensemble 1 and 2 for the same NRQCD mass. These ensembles differ by the sea quark masses and this does not affect Z.

The energy of the NRQCD-HISQ meson, P_c, from the fit does not correspond to the meson mass because there is an energy offset with NRQCD. This does not matter because the P_c meson is only being simulated to investigate the local vector current normalisation. The fit outputs in Table 5.6 are taken from a simultaneous fit to the 3-point correlators with different T and the NRQCD-charm 2-point correlator with 5 exponentials and 4 oscillating exponentials. The 3-point correlators have the same meson at 0 and T, so the fit has the additional constraints $a_i = b_i$ and $V_{ij}^{on} = V_{ji}^{no}$. As before, the ground state energy prior is from the 2-point effective mass and the priors for the splittings between successive excited states and between the ground state and the lowest oscillating state are taken to be 600(300) MeV. The priors widths for the 2-point and 3-point amplitudes are 0.5 and 0.25 respectively.

As before, the fit parameter V_{00} is related to the matrix element by

$$\langle P_c|V_t|P_c\rangle = 2m_{P_c}V_{00} \tag{5.26}$$

so comparison with Equation 5.19 reveals that V_{00} is expected to be 1 up to the Z factor and

$$Z = \frac{1}{V_{00}}. \tag{5.27}$$

The results are most clearly shown in a plot by plotting the ratio of the 3-point function to the 2-point function. Now the simplification that the P_c meson on both sides of the 3-point correlator is the same helps because the product of 2-point functions in the ratio is just $C_{2pt}(T)$.

Figures 5.7 and 5.8 show the ensemble average of the ratio

$$\frac{C_{3pt}(t,T)}{C_{2pt}(T)} \tag{5.28}$$

for varying am_h and T on the finest ensemble 3. Figure 5.7 shows data for $T = 24, 25, 30$ with $am_h = 2.0$. The shaded band is V_{00} obtained through the simultaneous multiexponential fit to all values of T. There are oscillations in the correlator, but the plateau lies near $V_{00} = 1$ as expected.

Figure 5.8 compares the correlator ratio for the two different heavy quark masses on the fine ensemble at $T = 30$. The shaded bands are the fitted values for V_{00} for the simulations with $am_h = 1.5$ and $am_h = 2.0$ and they overlap, which shows the small

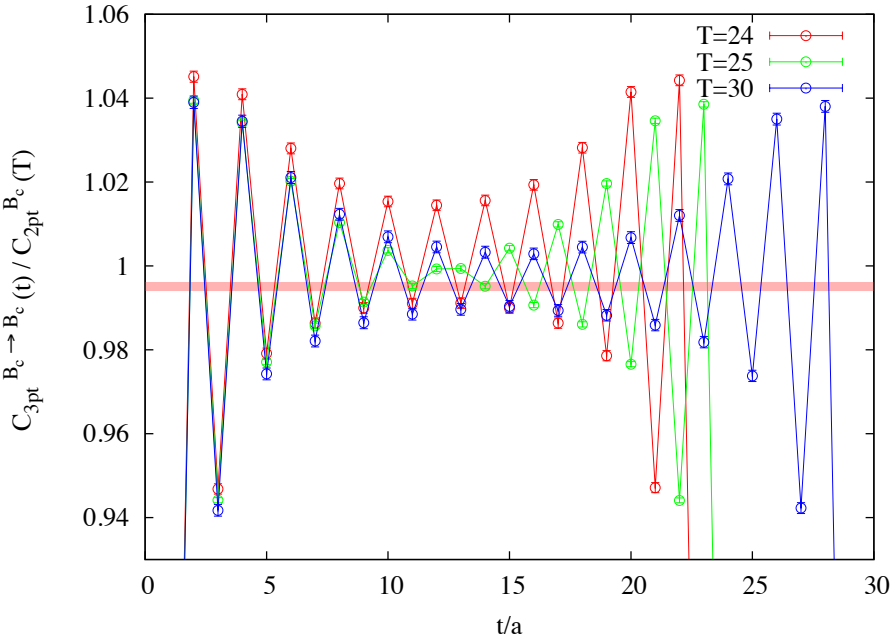

Figure 5.7: The correlator ratio $\frac{C_{3pt}(t,T)}{C_{2pt}(T)}$ on ensemble 3 for $am_h = 2.0$ and time lengths $T = 24, 25, 30$. The shaded band is the fitted $V_{00} \simeq 1$ obtained through a simultaneous fit to all T values. The plateau is clear despite the oscillations from staggered fermions.

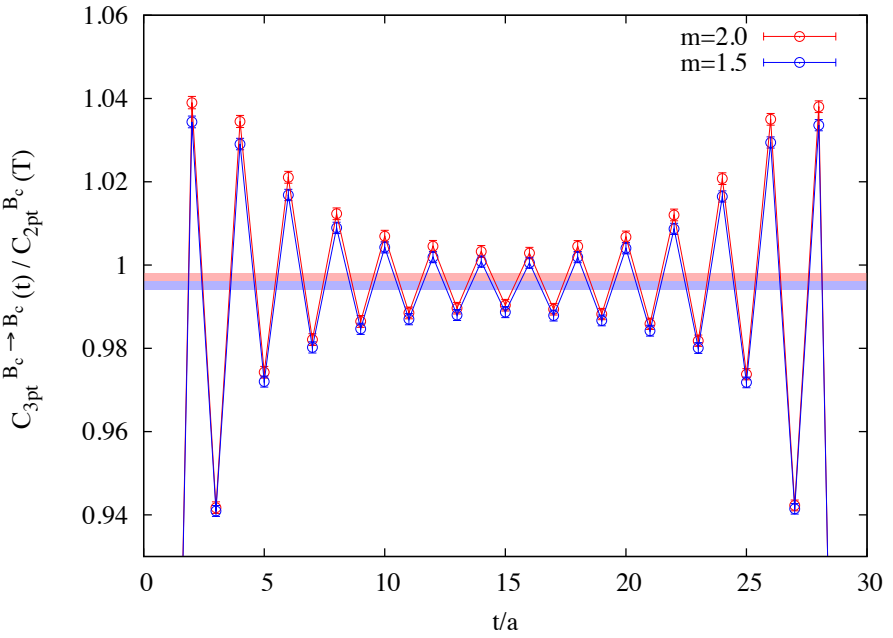

Figure 5.8: The correlator ratio $\frac{C_{3pt}(t,T)}{C_{2pt}(t)}$ on ensemble 3 for $T = 30$ and comparing different NRQCD heavy quark masses $am_b = 1.5, 2.0$. The shaded bands (which overlap) correspond to the fitted V_{00} obtained by a simultaneous fit to all T values at that mass. The plateaux are clear through the staggered oscillations and agree between the two NRQCD masses for this ensemble.

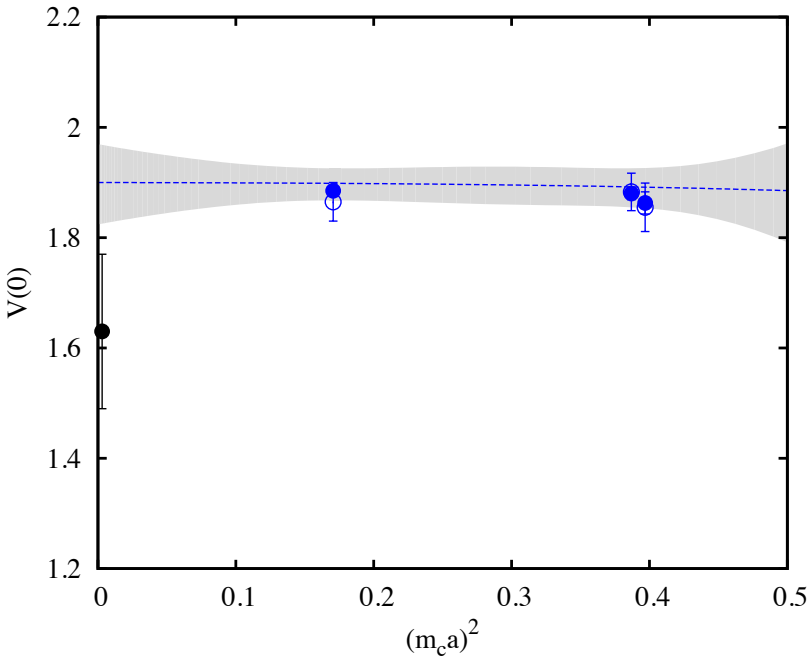

Figure 5.9: The continuum extrapolation of $V(0)$. The lattice data is shown is blue. The filled circles are from the Goldstone η_c set of operator used in the fit, but they are in agreement with the results using the non-Goldstone operators, shown with unfilled circles. The experimental data, extracted from [62] is offset slightly from zero. The grey shaded band is the fit.

effect am_h has on Z at this lattice spacing.

5.5 Continuum extrapolated decay rate

The lattice data is fitted to

$$V(0, a^2, \delta m) = V(0,0,0) \times (1 + \sum_{A=1}^{7} c_A (am_c)^{2A} + \chi_1 \delta m + \chi_2 (\delta m)^2). \tag{5.29}$$

Chiral effects are included with

$$\delta m_q = \frac{m_{q,sea} - m_{q,phys}}{m_{s,phys}} \tag{5.30}$$

and the sea quark mass dependence for the $J/\psi \to \eta_c\gamma$ form factor is in terms of

$$\delta m = 2\delta m_l + \delta m_s, \tag{5.31}$$

so $\delta m = 0$ is the physical limit.

The values for δm_l and δm_s for these ensembles are from Appendix A of [63]. The co-efficients of the chiral terms are consistent with zero in the fit.

The extrapolation is plotted in Figure 5.9 as a function of $(m_c a)^2$. There is very little lattice spacing dependence and only first two terms, proportional to $(m_c a)^2$ and

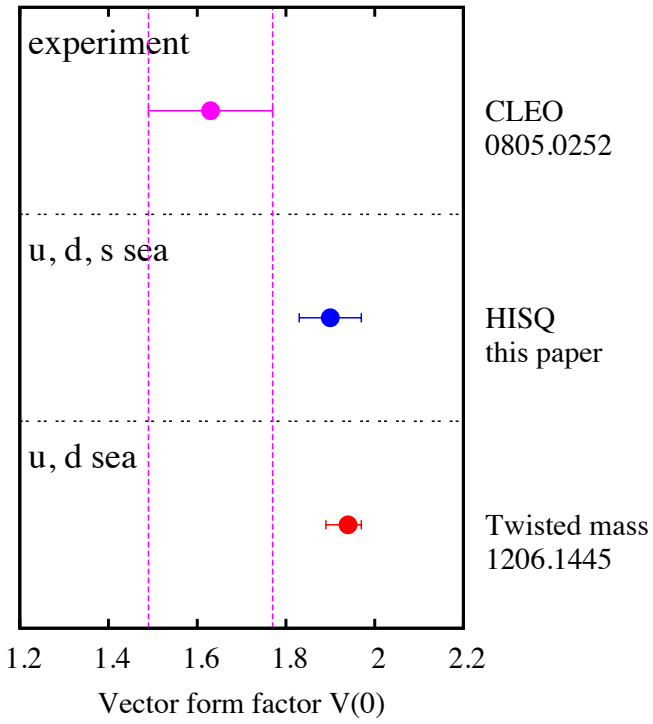

Figure 5.10: A comparison of the final result obtained for $V(0)$ with experimental data [62] and the other unquenched lattice QCD calculation [64], using $N_f = 2$ flavours of twisted mass sea quarks.

$(m_c a)^4$, contribute. A good fit is found including only the $(m_c a)^2$ in Equation 5.29, but multiple powers are allowed in the fit.

The physical value for $V(0)$ obtained is

$$V(0) = 1.90(7). \tag{5.32}$$

The data fitted is for the Goldstone η_c set of staggered operators, which has smaller statistical errors. The filled circles in Figure 5.9 are the Goldstone η_c data. The open circles are the lattice data from the non-Goldstone η_c set of operators. An extrapolation using the non-Goldstone η_c data gives $V(0)$ consistent with the Goldstone η_c.

In Figure 5.10, the value of $V(0)$ is compared to those extracted from the experimental data of [62] and calculated in a lattice calculation using twisted mass charm quarks [64]. The two lattice numbers agree and are slightly above the experimental number. Previous lattice calculations of the $J/\psi \to \eta_c\gamma$ transition were done in the quenched approximation [65, 66].

The lattice data is compared to the twisted mass data from Ref. [64] in Figure 5.11, where the blue circles are the HISQ data and the red sqaures the twisted mass. The HISQ calculation has much smaller discretisation errors, which can be seen from the dependence of the lattice data on a^2.

Systematic errors in the form factor $V(0)$ for the $J/\psi \to \eta_c\gamma$ transition are considered in Ref. [55] and are small. Possibles sources of systematic error are missing

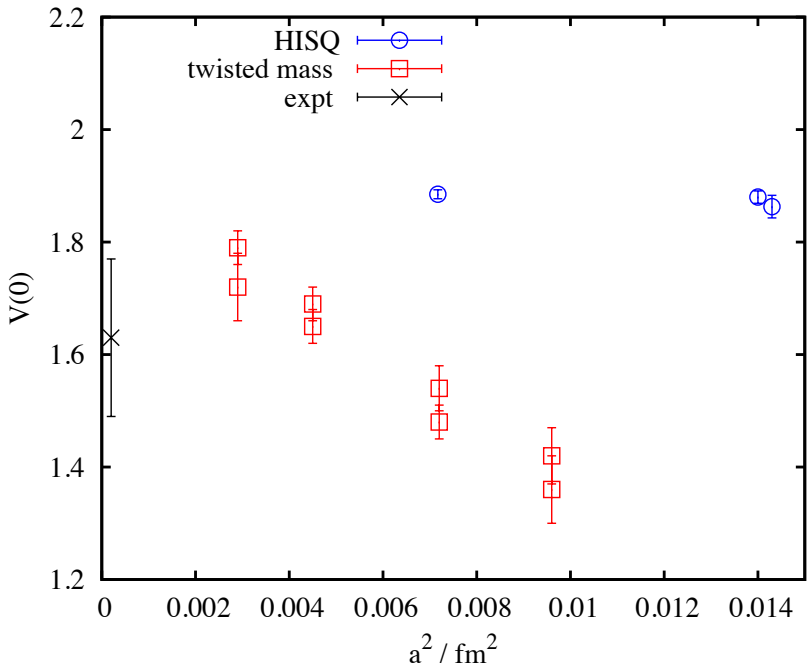

Figure 5.11: A direct comparison of the HISQ lattice data for $V(0)$ and the twisted mass data from [64]. The two lattice results agree in the continuum limit. The HISQ data is shown in blue and uses the Goldstone η_c operators.

electromagnetic effects, the lack of charm quarks in the sea and disconnected diagrams for the η_c. A systematic error of 0.5% is allowed for electromagnetism, whilst the absence of sea charm quarks is expected to be negligible. The $N_f = 2 + 1$ results is in agreement with ETMC's $N_f = 2$ calculation [64] and with Dudek et al's quenched result [65]. Disconnected diagrams are difficult to compute, so are not included. There are two types of disconnected contributions, both of which it is reasonable to neglect for charmonium decays [67]. Charm quark loops are suppressed by the large charm mass. The other type of disconnected diagram is for a photon coupling to a virtual light quark loop. This contribution should be small because the sum of the light quark charges $Q_u + Q_d + Q_s = 0$. η_c annihilation would shift the mass difference between the J/ψ and η_c mesons, and hence change the η_c momentum required to simulate at $q^2 = 0$. In Table 5.3, the effect of mistuning the kinematics away from $q^2 = 0$ does not produce a statistically significant change in $V(0)$. An uncertainty of 2.4 MeV in m_{η_c} corresponds to an uncertainty of 6×10^{-6} GeV^2 in q^2, which means that η_c annihilation is negligible.

Including the systematic error, the final result for $V(0)$ is

$$V(0) = 1.90(7)(1) \tag{5.33}$$

where the first error is a combined error from statistics and fitting and the second from other systematics. The dominant source of error is the final extracted value of $V(0)$ is from the continuum extrapolation.

Using Equation 5.3, this corresponds to $\Gamma_{J/\psi\to\eta_c\gamma} = 2.49(18)(7)$ keV.

Chapter 6

The radiative decay $\eta_C \to 2\gamma$

The decay $\eta_c \to 2\gamma$ is a radiative charmonium decay. It has been measured experimentally and the PDG average for the decay width is $\Gamma(\eta_c \to 2\gamma) = 5.3(3)$ keV, which is $(1.78 \pm 0.16) \times 10^{-4}$ of the total η_c decay width [5].

In a lattice calculation, $\eta_c \to 2\gamma$ can be simulated as the 3-point function shown in Figure 6.1, in which an η_c meson is created at time t_0 and there are two vector currents for the photons at later times t and T.

The operators resemble those used for $J/\psi \to \eta_c\gamma$, because the η_c is created with a pseudoscalar operator and there are two vectors. For $\eta_c \to 2\gamma$, the matrix element for the transition is $\langle \eta_c | V_\mu V_\nu | 2\gamma \rangle$, which contains both vector currents.

If the initial η_c is assumed to be at rest, the final state photons must each have energy $\omega_\gamma = \frac{m_{\eta_c}}{2}$ and carry momenta $p_\gamma = \frac{m_{\eta_c}}{2}$ in opposite directions.

The matrix element for $\eta_c \to 2\gamma$ is [68]

$$\langle \eta_c | V_\mu V_\nu | \gamma_1 \gamma_2 \rangle = 2 \left(\frac{2}{3} e \right)^2 m_{\eta_c}^{-1} F(q_1^2, q_2^2) \epsilon_{\mu\nu\sigma\rho} \varepsilon_1^\mu \varepsilon_2^\nu q_1^\sigma q_2^\rho, \tag{6.1}$$

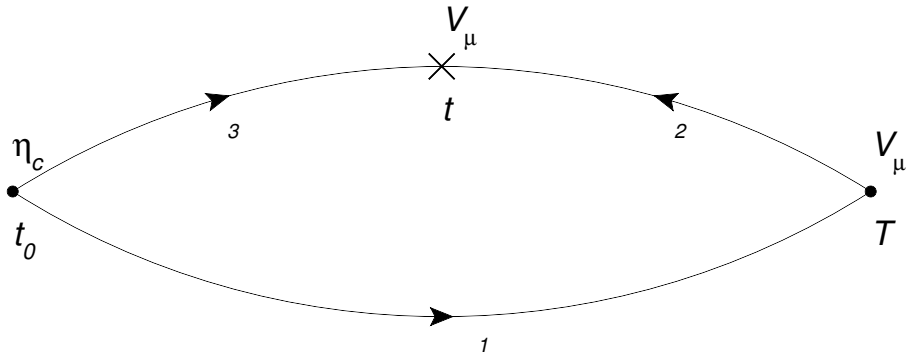

Figure 6.1: A diagram of the propagators in the correlation function used to simulate $\eta_c \to 2\gamma$ on the lattice. An η_c meson is created at t_0 and there are electromagnetic vector currents at later times t and T. The vector current at T is integrated over all timeslices on the lattice, so the correlation function looks like a 2-point correlator.

where the $\frac{2}{3}$ electric charge of the charm quark is missing in lattice simulations. It contains a nonperturbative QCD form factor, $F(q_1^2, q_2^2)$, where q_1 and q_2 are the momenta of the two photons. For physical photons, $q_1^2 = q_2^2 = 0$, so only the form factor at these kinematics is related to the decay rate by

$$\Gamma(\eta_c \to \gamma\gamma) = \pi\alpha_{em}^2 \frac{16}{81} m_{\eta_c} |F(0,0)|^2. \tag{6.2}$$

6.1 Method

The lattice calculation of $\eta_c \to 2\gamma$ is complicated by the final state containing only photons which do not interact with the strong force. However, matrix elements involving photons can be calculated in lattice QCD by expressing the photon as a superposition of QCD eigenstates [69]. The matrix element $\langle \eta_c | V_\mu V_\nu | 2\gamma \rangle$ was extracted from lattice QCD in [68] in the quenched approximation. The same correlation functions as used in [68] can be used to calculate the $\eta_c \to 2\gamma$ decay width using unquenched lattice configurations.

The starting point is the Green's function in Minkowski space for an η_c meson decaying to two photons with momenta q_i and helicities λ_i.

$$\begin{aligned} \langle \gamma(q_1,\lambda_1)\gamma(q_2,\lambda_2)|A_\mu A_\nu|\eta_c\rangle = &\lim_{q_i' \to q_i} \varepsilon_\mu(q_1,\lambda_1)\varepsilon_\nu(q_2,\lambda_2) q_1'^2 q_2'^2 \\ &\times \int d^4x d^4y e^{iq_1'y - iq_2'x} \langle 0|T\{A^\mu(y)A^\nu(x)\}|\eta_c\rangle, \end{aligned} \tag{6.3}$$

where $T\{A^\mu(y)A^\nu(x)\}$ is the time-ordered product of photon fields at points x and y in continuum spacetime. The photon fields do not couple to the $SU(3)$ gauge fields, U_μ, and can be integrated out of the path integral used to compute the matrix element by perturbatively expanding the QED action.

The photon fields in Equation 6.3 are included in the path integral

$$\int \mathcal{D}A\mathcal{D}U\mathcal{D}\bar{\psi}\mathcal{D}\psi e^{iS_{QCD}[U,\bar{\psi},\psi]} e^{iS_{QED}[A,\bar{\psi},\psi]} A^\mu(y)A^\nu(x), \tag{6.4}$$

where the QCD action does not contain photon fields.

Perturbatively expanding the QED action gives

$$e^{iS_{QED}} = (... + \left(\frac{e^2}{2}\int d^4w d^4z j_\rho(w) A^\rho(w) j_\sigma(z) A^\sigma(z)\right) + ...) \tag{6.5}$$

and is allowed because the electromagnetic coupling constant is small. Substituting the perturbatively expanded QED action into the path integral in Equation 6.4 gives

$$\int \mathcal{D}A\mathcal{D}\bar{\psi}\mathcal{D}\psi e^{iS_{QCD}[U,\bar{\psi},\psi]} \left(\frac{e^2}{2}\int d^4w d^4z j_\rho(w) A^\rho(w) j_\sigma(z) A^\sigma(z)\right) A^\mu(y)A^\nu(x). \tag{6.6}$$

The A^μ terms can be Wick contracted to give photon propagators. Neglecting disconnected pieces, as was done in Chapter 5 for the $J/\psi \to \eta_c\gamma$ transition, the full matrix element can be written as

$$\begin{aligned}\langle\gamma(q_1,\lambda_1)\gamma(q_2,\lambda_2)|A_\mu A_\nu|\eta_c\rangle = \lim_{q_i'\to q_i} e^2\varepsilon_\mu(q_1,\lambda_1)\varepsilon_\nu(q_2,\lambda_2)q_1^{'2}q_2^{'2} \\ \times\int d^4x d^4y d^4w d^4z\Big(e^{iq_1'\cdot y - iq_2'\cdot x}D^{\mu\rho}(y,z)D^{\nu\sigma}(x,w) \\ \times\langle 0|T\{j_\rho(z)j_\sigma(w)\}|\eta_c\rangle.\Big)\end{aligned} \tag{6.7}$$

The next step is to substitute in the photon propagator:

$$D^{\mu\rho}(y,z) = -ig^{\mu\rho}\int\frac{d^4k}{(2\pi)^4}\frac{e^{ik(z-y)}}{k^2+i\varepsilon}. \tag{6.8}$$

Written out explicitly, this is

$$\begin{aligned}\langle\gamma(q_1,\lambda_1)\gamma(q_2,\lambda_2)|A_\mu A_\nu|\eta_c\rangle = \lim_{q_i'\to q_i} e^2\varepsilon_\mu(q_1,\lambda_1)\varepsilon_\nu(q_2,\lambda_2)q_1^{'2}q_2^{'2} \\ \times\int d^4x d^4y d^4w d^4z e^{iq_1'y - iq_2'x}\Bigg\{\langle 0|T\{j_\rho(z)j_\sigma(w)\}|\eta_c\rangle \\ \times\left(-ig^{\mu\rho}\int\frac{d^4k}{(2\pi)^4}\frac{e^{ik(z-y)}}{k^2+i\varepsilon}\right)\left(-ig^{\nu\sigma}\int\frac{d^4k'}{(2\pi)^4}\frac{e^{ik'(w-x)}}{k'^2+i\varepsilon}\right)\Bigg\}.\end{aligned} \tag{6.9}$$

The integrals over x and y are straightforward:

$$\int\frac{d^4x}{(2\pi)^4}e^{i(-q_2'-k')x} = \delta(q_2'+k'), \tag{6.10}$$

$$\int\frac{d^4y}{(2\pi)^4}e^{i(q_1'-k)y} = \delta(-q_1'-k). \tag{6.11}$$

The integrals over k and k' are simple using these delta functions and the k^2 and k'^2 appearing in the denominators cancel with those outside the integral.

The right hand side of Equation 6.9 is then

$$e^2\varepsilon_\mu(q_1,\lambda_1)\varepsilon_\nu(q_2,\lambda_2)\int d^4w d^4z e^{iq_1z}e^{-iq_2w}\langle 0|T\{j_\rho(z)j_\sigma(w)\}|\eta_c\rangle. \tag{6.12}$$

To simulate on the lattice, the time coordinate must be rotated from Minkowski to Euclidean space. The time component picks up a factor of i in the rotation to Euclidean space. To get a correlation function that depends on one of the times, it is integrated over all the spatial coordinates and one time coordinate. Separating out the space and time coordinates of spacetime points w and z and making the simplification

that the photons have the same energy and carry the same momentum, this gives

$$\langle\gamma\gamma|A_\mu A_\nu|\eta_c\rangle(z_t) = e^2\varepsilon_\mu\varepsilon_\nu e^{q_t z_t}\int d^3w d^3z dw_t e^{-q_t w_t} e^{i\vec{q}\cdot\vec{z}} e^{-i\vec{q}\cdot\vec{w}}\langle 0|T\{j_\rho(z)j_\sigma(w)\}|\eta_c\rangle. \tag{6.13}$$

Referring to Figure 6.1, the point z is at time t and w is at time T, where T is integrated over all time. Including the creation of the initial η_c at t_0, the quantity to be calculated is

$$\langle\bar{\psi}(t_0)\gamma_5\psi(t_0)e^{-q_t t - i\vec{q}\cdot\vec{z}}\bar{\psi}(t)\gamma_\mu\psi(t)\int dT e^{q_t T + i\vec{q}\cdot\vec{w}}\bar{\psi}(T)\gamma_\nu\psi(T)\rangle. \tag{6.14}$$

An integration of the spatial coordinates is assumed, but the integration over T remains explicit.

6.2 Lattice implementation

On the lattice, the integrals are replaced with sums over lattice sites. The spacetime points w and z are replaced by lattice sites j and k respectively and the initial η_c is created on a site i at the source time t_0. The staggered operators needed for the $\eta_c \to 2\gamma$ are the same as for the $J/\psi \to \eta_c\gamma$ in Chapter 5 – one pseudoscalar and two vectors. It is preferable to use a Goldstone $(\gamma_5 \otimes \gamma_5)$ η_c, so the vectors are a local $\gamma_\nu \otimes \gamma_\nu$ and 1-link $\gamma_t\gamma_\mu \otimes \gamma_t\gamma_\mu\gamma_\rho$, where μ, ν and ρ are the three spatial directions. It does not matter which vector operator is placed at t and T, but in the following discussion, the local vector is at T. In the $\eta_c \to 2\gamma$ calculation, the vector directions were chosen so that the local vector was $\gamma_z \otimes \gamma_z$ and the 1-link vector $\gamma_t\gamma_x \otimes \gamma_t\gamma_x\gamma_y$. The staggered correlation function calculated on the lattice is

$$C_{\eta_c\to 2\gamma}(0,t) = \sum_{i,j}\sum_k (-1)^{j_y}\varepsilon(k)(-1)^{k_z}(e^{-q_t j_t - i\vec{q}\cdot\vec{j}}e^{q_t k_t + i\vec{q}\cdot\vec{k}})\mathrm{Tr}\left[g(k, j\pm\hat{y})g(i,k)g^\dagger(i,j)\right], \tag{6.15}$$

where the sum is over sites i and j on timeslices $i_t = 0$ and $j_t = t$ and the separate sum over k is over sites on all timeslices, which implements the integral over T in Equation 6.14.

To obtain physical kinematics, the photons must have $q^2 = 0$, which means $q_t = \frac{m_{\eta_c}}{2}$ and $\vec{q}^2 = \left(\frac{m_{\eta_c}}{2}\right)^2$. The source for the extended propagator from T to t is based on $g_c(k) = \sum_i (\not{D} + m_c)(i,k)\eta(i)$, a charm propagator with no momentum and no phase at the source. The right kinematics are achieved by multiplying $g_c(k)$ by $e^{q_t\tilde{k}_t}$ in the time direction, where $q_t = \frac{m_{\eta_c}}{2}$ and $\tilde{k}_t$ is the time distance from the source t_0 using in the original inversion. Note that $\tilde{k}_t \in [0, L_t/2)$ is the shortest distance between T and t_0, where periodic boundary conditions are used. Twisted boundary conditions are applied in the extended propagator inversion to implement momentum q with $\vec{q}^2 = \left(\frac{m_{\eta_c}}{2}\right)^2$. The source vector includes the staggered phase at k, so it is $e^{q_t\tilde{k}_t}\varepsilon(k)(-1)^{k_z}g_c(k)$. This is a 4-dimensional source, which means it is non-zero on all timeslices on the lattice.

Ens.	N_{cfgs}	r_1/a	am_l^{sea}	am_s^{sea}	am_c^{sea}	$L_s \times L_t$	δm_l	δm_s
1	567	2.647(3)	0.005	0.05	–	24×64	0.11	0.43
2	2259	2.618(3)	0.01	0.05	–	20×64	0.25	0.43
3	260	2.618(3)	0.01	0.05	–	28×64	0.25	0.43
4	500	2.644(3)	0.02	0.05	–	20×64	0.53	0.43
5	323	2.658(3)	0.01	0.03	–	20×64	0.25	-0.14
6	1911	3.699(3)	0.0062	0.031	–	28×96	0.20	0.19
7	309	3.695(4)	0.0031	0.031	–	40×96	0.08	0.19
8	98	5.296(7)	0.0036	0.018	–	48×144	0.16	-0.03
9	201	2.598(13)	0.00184	0.0507	0.628	48×64	–	–
10	203	3.581(28)	0.0012	0.0363	0.432	64×96	–	–

Table 6.1: The ensembles used for the $\eta_c \to 2\gamma$ calculation. The configurations in the top part of the Table contain $2+1$ flavour of asqtad sea quarks, so there are not charm quarks in the sea. The difference between the simulated and physical sea quark masses are given by δm_q, which is defined in Equation 5.30. Ensembles 9 and 10 include $2+1+1$ flavours of HISQ sea quarks, where the light quarks are simulated close to their physical masses.

The result, $\tilde{g}_{ext}(j)$, is modified by $g_{ext}(j) = \tilde{g}_{ext}(j)e^{-q_t j_t}$ to put the rest of the necessary exponential in the correlator. The correlation function is found by combining $g_{ext}(j)$ and $g_c(j)$, including the phase factor $(-1)^{j_y}$.

The configurations used are listed in Table 6.1, with the number of configurations used and information about the lattice spacing, size and sea quarks. Ensembles 1,2 and 6 are the same ensembles used in Chapter 5. Ensembles 1-8 include $N_f = 2+1$ flavours of sea quark, which are simulated with the asqtad action. Ensembles 9 and 10 in the lower part of Table 6.1 have $N_f = 2+1+1$ flavours of HISQ sea quark, where the charm quark has been included in the sea. The light sea quarks in these ensembles are simulated at their physical values.

The $\eta_c \to 2\gamma$ correlation function, $C_{\eta_c \to 2\gamma}(t)$, defined in Equation 6.15 is fitted to

$$\sum_A a_A a_{\gamma A} e^{-E_A t}. \tag{6.16}$$

The fit is done simultaneously with the $\eta_c \to \eta_c$ 2-point correlator, which is fitted to

$$\sum_A a_A^2 e^{-E_A t}, \tag{6.17}$$

where a_A and E_A are shared parameters. This fit extracts the matrix element, which is proportional to $a_{\gamma i}$.

As discussed in Section 4.2, the ground state amplitude from the $\eta_c \to \eta_c$ 2-point correlator fit is

$$a_0^2 e^{-E_{\eta_c} t} = \frac{\langle 0|V_\mu V_\nu|\eta_c\rangle^2}{2E_{\eta_c}} e^{-E_{\eta_c} t}, \tag{6.18}$$

so the amplitude is normalised as

$$a_0 = \frac{\langle 0|\gamma_5|\eta_c\rangle}{\sqrt{2E_{\eta_c}}}. \tag{6.19}$$

This includes the cancelling factors for 4 from the tastes and the lattice derivative in the code. Considering only the ground state for simplicity, the normalisation for $C_{\eta_c\to 2\gamma}(t)$ is

$$\frac{\langle 0|\gamma_5|\eta_c\rangle\langle\eta_c|V_\mu V_\nu|\gamma\gamma\rangle}{2E_{\eta_c}}\frac{4}{2^3}, \tag{6.20}$$

where the 4 comes from 4 staggered tastes in the loop and there is a factor of 2 included in the normalisation for each inversion. This means that the fit parameter $a_{\gamma 0}$ is related to the matrix element by

$$a_{\gamma 0} = \frac{1}{2\sqrt{2E_{\eta_c}}}\langle\eta_c|V_\mu V_\nu|\gamma\gamma\rangle. \tag{6.21}$$

The dimensionless form factor $F(q_1^2, q_2^2)$ appears in the matrix element as in Equation 6.1 and is related to the matrix element by Equation 6.2.

In the lattice calculation, the photon polarisations are chosen as ε_1 in the z direction, ε_2 in the x direction and both photons' momentum are in the y direction. As the two photons are tuned to the right kinematics, $|q_1^y| = q_1^t = |q_2^y| = q_2^t = \frac{m_{\eta_c}}{2}$,

$$\epsilon_{\mu\nu\sigma\rho}\varepsilon_1^\mu\varepsilon_2^\nu q_1^\sigma q_2^\rho = \frac{m_{\eta_c}^2}{2}, \tag{6.22}$$

where there are two contributions (both $\sigma = y, \rho = t$ and $\sigma = t, \rho = y$). Note that the two contributions get opposite signs from the antisymmetric $\epsilon_{\mu\nu\sigma\rho}$ symbol, but are still added because the spatial momenta of the photons are in opposite directions. Therefore, $F(0,0)$ is extracted using

$$F(0,0) = 2a_{\gamma 0}\sqrt{\frac{2}{m_{\eta_c}}}. \tag{6.23}$$

The lattice calculation results are shown in Table 6.2. For the larger gauge configurations, the MILC code was used for the inversions. Larger lattices require more computer memory to invert, so need multiple cores running in parallel. In the calculations with the MILC code, the gauge links are included in the point-split vector operator. The normalisation of the 1-link vector operator depends on whether or not the gauge links are included in the operator. In Table 6.2, column 4 indicates whether or not there are gauge links in the 1-link operator. When they are included in the $\eta_c \to 2\gamma$ correlation function, they are also included in the Z factor. There are 2 calculations on ensemble 2, with and without the gauge links included. The unnormalised $F(0,0)$ and Z_{1link} both differ, but the normalised $F(0,0)$ agree.

The local vector current is normalised using current correlators; $Z(4)$ and $Z(6)$ are

Ens.	am_c	ε_N	U_μ?	$Z(4)$	$Z(6)$	Z_{1link}	$F(0,0)$
1	0.622	-0.221	Yes	1.068(11)	0.9429(95)	1.390(15)	0.25489(17)
2	0.630	-0.226	Yes	1.073(10)	0.9459(92)	1.385(15)	0.25507(15)
	0.630	-0.226	No	1.073(10)	0.9459(92)	1.289(13)	0.27461(8)
3	0.630	-0.226	No	1.073(10)	0.9459(92)	1.289(13)	0.27428(20)
4	0.625	-0.223	No	1.073(10)	0.9459(92)	1.280(13)	0.27476(14)
5	0.617	-0.218	No	1.073(10)	0.9459(92)	1.291(13)	0.27487(18)
6	0.413	-0.107	No	0.994(14)	0.929(12)	1.177(15)	0.27514(8)
7	0.413	-0.107	Yes	0.994(14)	0.929(12)	1.283(17)	0.25119(12)
8	0.273	-0.049	Yes	0.982(12)	0.959(12)	1.296(17)	0.24978(25)
9	0.637	-0.230	Yes	1.0732(91)	0.9463(83)	1.389(12)	0.25080(10)
10	0.432	-0.116	Yes	0.995(12)	0.926(11)	1.285(15)	0.25065(11)

Table 6.2: The lattice results for the unnormalised $\eta_c \to 2\gamma$ form factor $F(0,0)$ and the Z factors for the vector currents in the calculation. The local Z factor is calculated using the current correlator method. $Z(4)$ and $Z(6)$ are the Z factors extracted using either the 4th or 6th time moments. Z_{1link} is computed by comparing 1-link J/ψ meson correlators to local J/ψ correlators which have been normalised using $Z(6)$. The normalisation of the 1-link vector current depends on whether or not gauge links are used in the point-split operator, which is given in column 4.

the normalisations obtained using the 4th and 6th time moments respectively. Z_{1link} is the normalisation for the 1-link vector and is obtained by comparing local and 1-link vector meson correlators. The methods used for the current normalisation are explained in the next section.

The lattice data is shown in Figure 6.2 against a^2. The values of $F(0,0)$ shown in this plot include the renormalisation factors for both vector currents. The $N_f = 2+1$ numbers are plotted with triangles and the $N_f = 2+1+1$ with squares. It is clear in Figure 6.2 that $F(0,0)$ agrees on the $N_f = 2+1$ and $N_f = 2+1+1$ ensembles.

6.3 Z factors

The matrix element $\langle \eta_c | V_\mu V_\nu | \gamma\gamma \rangle$ contains two insertions of a vector operator. In the staggered calculation, the two vector operators used must be different for the correlator to have the right taste and therefore have different renormalisation factors. To get the correctly normalised $F(0,0)$, the lattice results for $F(0,0)$ need to be multiplied by $Z_{local} Z_{1link}$.

6.3.1 Local V_μ from current correlators

The current correlator method for normalising charm vector currents was used in [55] to extract $f_{J/\psi}$. The Z factor is extracted from the low t behaviour of meson 2-point correlators, so is computationally cheaper than the vector form factor method described in Section 5.4. The Z factors using the current correlator method were calculated by Peter Lepage.

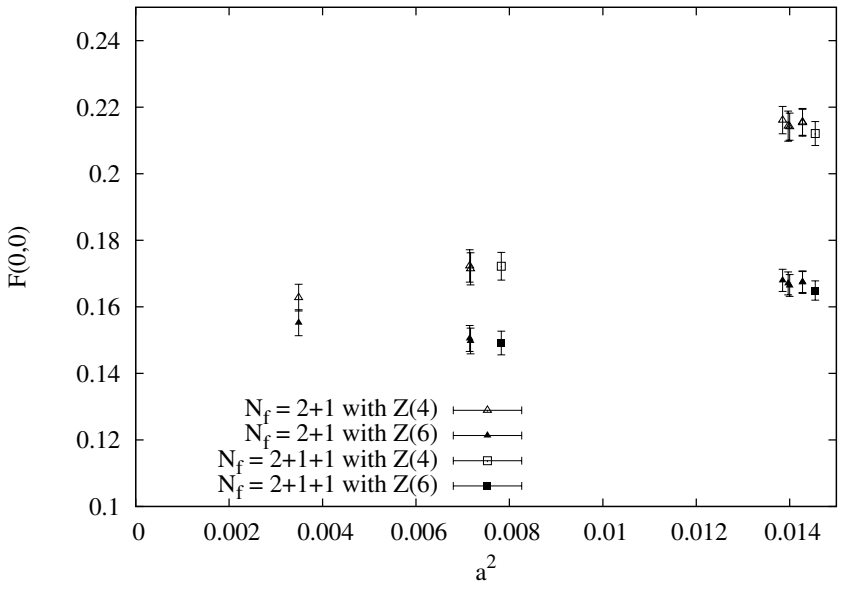

Figure 6.2: The normalised lattice data for $F(0,0)$. The data from $N_f = 2+1$ (triangles) and $N_f = 2+1+1$ (squares) agree. Data normalised using $Z(4)$ for the local vector normalisation is shown with open symbols and data normalised using $Z(6)$ with closed symbols. The continuum extrapolated results for $F(0,0)$ are the same whether $Z(4)$ or $Z(6)$ is used for the local vector normalisation.

The Z factor is calculated by comparing time moments of 2-point correlators calculated in lattice QCD to continuum perturbation theory [70, 71, 72, 73]. Time moments for heavyonium mesons at rest can be computed very accurately in lattice QCD [70] and comparisons of pseudoscalar time moments with continuum perturbation theory have been used to extract quark masses and α_s [74].

For charmonium, the vector and pseudoscalar time moments are defined respectively as

$$C_n^V = \sum_{\tilde{t}} \tilde{t}^n \bar{C}_{J/\psi}(\tilde{t}) \text{ and } C_n^P = \sum_{\tilde{t}} \tilde{t}^n (am_c)^2 \bar{C}_{\eta_c}(\tilde{t}), \tag{6.24}$$

where $\tilde{t}$ is symmetrised around $L_t/2$. For small n, the moments probe short times and are expected to match perturbation theory as

$$C_n^P = \frac{g_n^P(\alpha_{\overline{MS}}(\mu), \mu/m_c)}{(am_c(\mu))^{n-4}} + \mathcal{O}((am_c)^m) \tag{6.25}$$

for the pseudoscalar and

$$C_n^V = \frac{1}{Z^2} \frac{g_n^V(\alpha_{\overline{MS}}(\mu), \mu/m_c)}{(am_c(\mu))^{n-2}} + \mathcal{O}((am_c)^m) \tag{6.26}$$

for the vector, where g_n is the $\overline{MS}$ continuum perturbation series. The pseudoscalar time moments are normalised because of the HISQ PCAC relation and Z is the renormalisation factor for the vector current. Taking the ratio of the pseudoscalar and vector

moments cancels powers of the charm mass, so Z is given by

$$Z(n) = \sqrt{\frac{C^P_{n+2}/C^V_n}{c^P_{n+2}/c^V_n}}, \tag{6.27}$$

where C^P_n and C^V_n are the lattice time moments and c^P_n and c^V_n are the moments from continuum perturbation theory. The $Z(n)$ calculated for different n can differ by discretisation effects at finite lattice spacing, but agree in the continuum limit.

For the coarse ensembles 3, 4 and 5, the local Z factors were taken to be the same as ensemble 2. These ensembles only differ by the sea quark masses and number of sites (ensembles 2 and 3 only differ by spatial volume). The Z factors were calculated for ensembles 1 and 2, which have the same lattice spacing, and were found not to depend on the sea quark masses. Similarly, the local Z factor for ensemble 7 was taken to be the same as calculated for ensemble 6.

The $F(0,0)$ data, normalised using either $Z(4)$ or $Z(6)$ for the local vector normalisation, is shown in Figure 6.2. The filled symbols are normalised using $Z(6)$ and the open symbols using $Z(4)$. There are larger discretisation effects for $Z(4)$, but they agree in the $a \to 0$ limit. Results for both $Z(4)$ and $Z(6)$ are given in Table 6.2. For the final results for $F(0,0)$, the current correlator normalisation is taken as $Z_{local} = Z(6)$.

6.3.2 1-link V_μ

Once the local vector operator has been normalised, the 1-link vector can be normalised by comparing J/ψ 2-point functions with the local and 1-link operators used for the J/ψ. The correlators are

$$C^{local}_{J/\psi}(t) = \sum_{i,j}(-1)^{i_z}(-1)^{j_z} \times \mathrm{Tr}\left[g(i,j)(g^\dagger(i,j)\right] \tag{6.28}$$

$$C^{1link}_{J/\psi}(t) = \sum_{i,j}(-1)^{i_x+i_z+i_t}(-1)^{j_x+j_z+j_t} \times \mathrm{Tr}\left[g(i,j)(g^\dagger(i \pm \hat{y}, j \pm \hat{y})\right]. \tag{6.29}$$

They are fitted to

$$C_{J/\psi}(t) = \sum_{AA_o} a_A e^{-m_A t} + (-1)^t a_{A_o} e^{-m_{A_o} t}. \tag{6.30}$$

The ground state fit amplitude is related to the decay constant by

$$a_0 = \frac{f_{J/\psi}}{Z}\sqrt{\frac{m_{J/\psi}}{2}} \tag{6.31}$$

because the decay constant is defined as

$$\langle 0|V_\mu|J/\psi\rangle = f_{J/\psi} m_{J/\psi}. \tag{6.32}$$

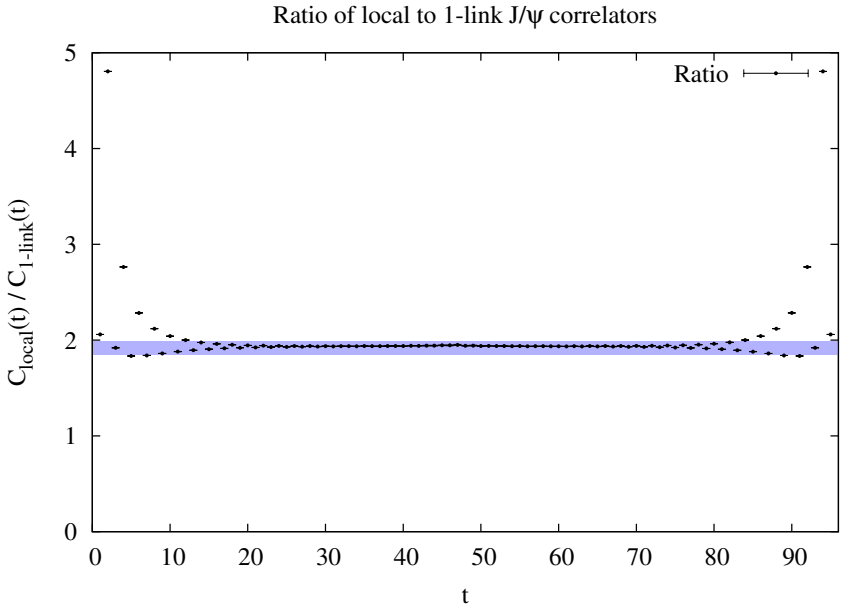

Figure 6.3: The ratio of correlators shows Z factors, averaged over ensemble 10. The shaded band shows $\left(\frac{Z_{1link}}{Z_{local}}\right)^2$ where the ratio should plateau for large t.

Up to the normalisation, the decay constants obtained with either vector operator are the same. Therefore

$$Z_{1link} = Z_{local}\frac{f_{J/\psi}/Z_{local}}{f_{J/\psi}/Z_{1link}}. \tag{6.33}$$

In Figure 6.3, the ratio of the local to 1-link J/ψ 2-point correlators calculated on ensemble 10 is plotted. The shaded band indicates where the ratio is expected to plateau away from the contributions from excited states

$$\frac{C^{local}_{J/\psi}(t)}{C^{1link}_{J/\psi}(t)} \to \left(\frac{Z_{1link}}{Z_{local}}\right)^2. \tag{6.34}$$

The error in Z_{1link} is dominated by the error coming from Z_{local} determined from the current correlators. These Z factors are given in Table 6.2.

6.4 Results

The lattice data is extrapolated to the physical limit in the same way as the $V(0)$ form factor for $J/\psi \to \eta_c\gamma$, given by Equation 5.29. The lattice $\eta_c \to 2\gamma$ form factor $F(0,0,a^2,\delta m)$ is fitted to

$$F(0,0,a^2,\delta m) = F(0,0,a^2=0,\delta m=0) \times (1 + \sum_{A=1}^{7} c_A (am_c)^{2A} + \chi_1 \delta m + \chi_2 (\delta m)^2). \tag{6.35}$$

The result of the extrapolation is

$$F(0,0) = 0.154(7). \tag{6.36}$$

Replacing $Z(6)$ with $Z(4)$ for the local current normalisation factor does not change the physically extrapolated result. Fitting only the $N_f = 2+1$ data gives the same result as fitting both the $N_f = 2+1$ and $N_f = 2+1+1$ data together. The terms beyond a^6 in the continuum extrapolation are not needed by the fit. The coefficients for the chiral terms are consistent with zero and the fit is unaffected if they are removed entirely.

This corresponds to a decay rate of 2.44(22) keV, which is in agreement with the previous quenched lattice QCD calculation [68]. The most recent experimental results for the decay rate are 5.2(1.2) keV from BaBar [75] and 5.5(1.2)(1.8) keV from Belle [76]. The agreement between the experimental results and the lattice calculations is poor. Disconnected diagrams are neglected in the lattice simulation because they are expensive to compute. It is not clear how big an effect the disconnected diagrams have on this process, but may be worth investigating.

Chapter 7

The semileptonic decay $D_s \to \phi\ell\nu$

The decay $D_s \to \phi\ell\nu$ is a semileptonic decay involving a quark level $c \to s$ decay via the emission of a W boson. Correspondingly, the decay rate depends on the CKM matrix element V_{cs}, which can be extracted from a comparison of experimental measurements of the decay rate and theoretical calculations. The decay rate is a combination of the CKM matrix element and nonperturbative QCD form factors, which can be calculated in a lattice simulation. The D_s meson is a charged pseudoscalar containing a charm and strange quark antiquark pair. On the lattice the effects of QED are neglected so there is no distinction between $D_s^{\pm}$. The ϕ is a vector meson which predominantly has quark content $s\bar{s}$.

The quark level decay is mediated by the weak interaction and proceeds through both vector and axial vector currents. It is convenient to consider the case where the $W^{\pm}$ boson from the weak interaction decays leptonically. On the lattice, this means that there is only one strongly interacting particle (the ϕ) in the final state and the leptons can be ignored as they do not have QCD interactions. In a collider experiment, the lepton in the final state gives a clean signature for the decay. The most precise experimental measurement of the $D_s \to \phi$ form factor is from BaBar [77], in which the final state is $e^{\pm}\nu_e K^+ K^-$, so the $W^{\pm}$ boson decays to an electron and a neutrino and the unstable ϕ mesons to charged kaons. The $D_s \to \phi$ decay was previously measured by FOCUS [78] with muons in the final state. Previous lattice calculations of the form factors were in the quenched approximation [79].

Taking the general form of the matrix element for a pseudoscalar to vector meson transition and labelling the pseudoscalar meson D_s with momentum p and the vector

ϕ with polarisation vector ε and momentum p' gives [80]

$$\begin{aligned}\langle\phi(p',\varepsilon)|V^\mu - A^\mu|D_s(p)\rangle = &\frac{2i\epsilon^{\mu\nu\alpha\beta}}{m_{D_s}+m_\phi}\varepsilon_\nu p_\alpha p'_\beta V(q^2) \\ &- (m_{D_s}+m_\phi)\varepsilon^\mu A_1(q^2) \\ &+ \frac{\varepsilon\cdot q}{m_{D_s}+m_\phi}(p+p')^\mu A_2(q^2) \\ &+ 2m_\phi\frac{\varepsilon\cdot q}{q^2}q^\mu A_3(q^2) \\ &- 2m_\phi\frac{\varepsilon\cdot q}{q^2}q^\mu A_0(q^2).\end{aligned} \tag{7.1}$$

The form factor $A_3(q^2)$ is defined as

$$A_3(q^2) = \frac{m_{D_s}+m_\phi}{2m_\phi}A_1(q^2) - \frac{m_{D_s}-m_\phi}{2m_\phi}A_2(q^2) \tag{7.2}$$

and, at $q^2 = 0$, it is related to $A_0(q^2)$ by

$$A_3(0) = A_0(0). \tag{7.3}$$

There are then three independent axial vector form factors, $A_1(q^2)$, $A_2(q^2)$ and $A_0(q^2)$, although only 2 are independent at $q^2 = 0$. There is one vector form factor, which is the same form factor that appears for electromagnetically mediated transitions between vector and pseudoscalar mesons. The form factors are functions of $q^2 = (p_{D_s} - p_\phi)^2$ and the lepton-neutrino pair have a continuous energy spectrum, so the decay rate depends on all values of q^2 from zero up to the maximum, $q^2_{max} = (m_{D_s} - m_\phi)^2$. The kinematics for which $q^2 = q^2_{max}$ are when the charged lepton and neutrino are emitted back to back. This can be simulated with both the initial state D_s and the ϕ in the final state at rest. $q^2 = 0$ corresponds to the maximum kinematically allowed ϕ recoil.

If the leptons can be assumed to be massless (they can for electrons and muons), the terms in the matrix element proportional to q^μ can be ignored. In the decay rate, these terms are proportional to m^2_ℓ. This means that $A_3(q^2)$ and $A_0(q^2)$ do not contribute to the decay rate and are experimentally inaccessible.

The form factor can be calculated on the lattice by setting up the 3-point calculations such that only one form factor contributes at a time. To extract all the form factors requires both vector and axial vector staggered currents. Various different combinations of staggered operators are possible for the $D_s \to \phi$ decay and require current renormalisation factors, which are calculated non-perturbatively.

The gauge configurations used for the calculation are the same MILC configurations as used for the $J/\psi \to \eta_c\gamma$ decay. These contain $N_f = 2+1$ flavour of sea quarks with the asqtad action. The parameters are listed in Table 7.1, which gives r_1/a from [35] for each ensemble, the sea quark masses, lattice size, number of configurations and the valence (HISQ) strange and charm quark masses.

Ensemble	r_1/a	$\mu_0 am_l^{sea}$	$\mu_0 am_s^{sea}$	L_s	L_t	N_{confs}	am_s	am_c	ϵ_N
1	2.647(3)	0.005	0.05	24	64	2088	0.0489	0.622	-0.221
2	2.618(3)	0.01	0.05	20	64	2259	0.0496	0.630	-0.226
3	3.699(3)	0.0062	0.031	28	96	1911	0.0337	0.413	-0.107

Table 7.1: Ensembles of MILC configurations used for this analysis, which are the same ensembles as used for $J/\psi \to \eta_c\gamma$. The charm mass is the same as before and the valence strange quark mass is also quoted. 4 time sources per configuration were used.

The D_s meson has been previously studied [63, 81, 59, 82], including simulations using HISQ valence quarks. The ϕ meson is less well-studied, so this chapter begins with results for the ϕ meson to check that the lattice simulation agrees with the physical ϕ. Then the calculations for the form factor and the required current normalisations are described. These give the lattice data used to extrapolate to the continuum and obtain the decay rates that can be compared with experimental results.

7.1 Checks of the ϕ meson

It is easiest to study mesons that do not decay strongly in lattice QCD. The ϕ meson has a mass of 1020 MeV [5] and is above the threshold to decay to $K\bar{K}$. This makes it more challenging to study in lattice QCD because the ϕ meson can mix with $K\bar{K}$ states. The light sea quarks in a lattice simulation are heavier than in the continuum. This means that m_K is higher and the ϕ meson is actually below the $K\bar{K}$ threshold. It is important to check that the ϕ mesons used in the simulations of the $D_s \to \phi\ell\nu$ semileptonic decay resemble the continuum ϕ, i.e. that the coupling to real or virtual $K\bar{K}$ states does not significantly change the mass.

The ϕ mesons simulated on the lattice are pure $s\bar{s}$ states. Any taste of vector meson operator can be used for the ϕ and all should agree up to small taste-splittings, proportional to a^2. It is useful to consider ϕ mesons made with the local $(\gamma_\mu \otimes \gamma_\mu)$ and taste-singlet $(\gamma_\mu \otimes 1)$ vector operators.

The local ϕ correlator is

$$C_{2pt}^{local}(0,t) = \sum_{i,j} (-1)^{i_\mu}(-1)^{j_\nu} \times \mathrm{Tr}\left[g_s(i,j)g_s^\dagger(i,j)\right], \tag{7.4}$$

where the sums over i and j are over timeslices and $j_t - i_t = t$.

The taste-singlet operator is a 1-link point-split operator with the link in the same direction as the vector current. The taste-singlet ϕ correlator is

$$C_{2pt}^{1link}(0,t) = \sum_{i,j} (-1)^{i_\mu^<}\varepsilon(i)(-1)^{j_\nu^<}\varepsilon(j) \times \mathrm{Tr}\left[g_s(i,j)g_s^\dagger(i \pm \hat{\mu}, j \pm \hat{\mu})\right]. \tag{7.5}$$

The mass and decay constant can be extracted from a fit to the 2-point correlators

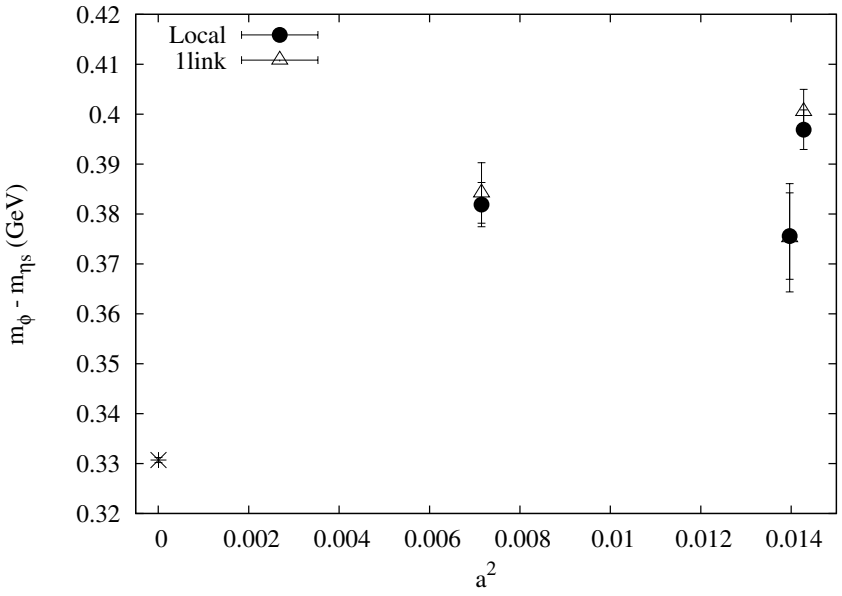

Figure 7.1: A plot of $m_\phi - m_{\eta_s}$ against a^2. The physical m_{η_s} is from [60]. Filled circles indicate ϕ mesons simulated with the local vector operator and unfilled triangles indicates ϕ mesons simulated with the taste-singlet vector. The mass difference is also affected by the sea quark masses which differ for the two coarsest ensembles.

as

$$\langle 0|V_\mu|\phi\rangle = f_\phi m_\phi. \tag{7.6}$$

The results are taken from a fit with 6 exponential and 5 oscillating exponential terms.

7.1.1 Mass, m_ϕ

Figure 7.1 shows $m_\phi - m_{\eta_s}$, the vector-pseudoscalar mass splitting for $s\bar{s}$ mesons for the local and 1-link ϕ. The continuum value is plotted at $a^2 = 0$. Ensemble 1 has a slightly smaller lattice spacing than ensemble 2 and has lighter sea quark masses for the up and down quarks. The mass difference $m_\phi - m_{\eta_s}$ is also affected by the sea quark masses. The ϕ mass on these ensembles is $40 - 60$ MeV higher than the physical ϕ mass and is closer to the physical for ensembles with finer lattice spacings and with lighter sea quarks. This sea quark mass dependence is consistent with coupling to $K\bar{K}$.

The difference in mass of the local and 1-link ϕ mesons is less than the statistical errors on all ensembles.

7.1.2 Decay constant, f_ϕ

The ground state in the fit to the 2-point correlators is

$$a_\phi^2 e^{-m_\phi t}. \tag{7.7}$$

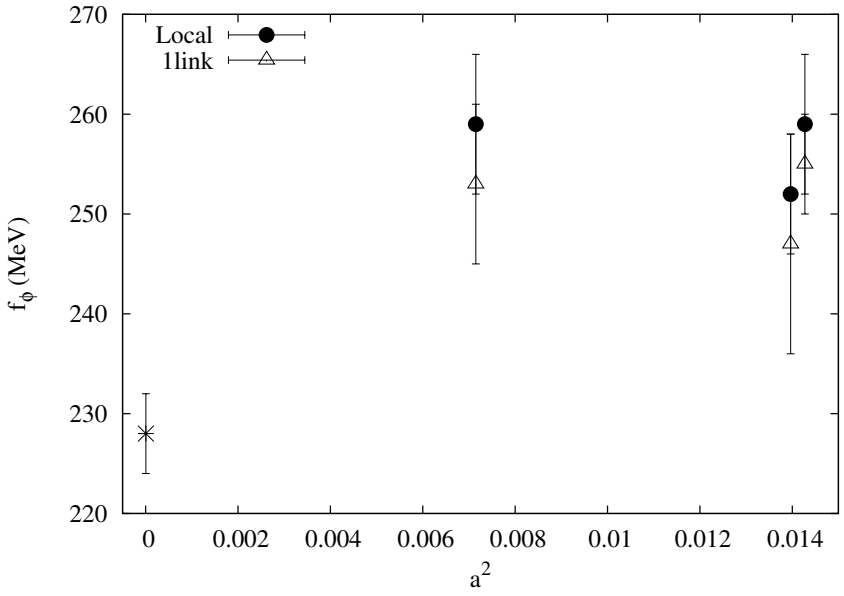

Figure 7.2: The ϕ meson decay constant, f_ϕ, plotted against a^2. Filled circles indicate ϕ mesons simulated with the local vector operator and unfilled triangles indicates ϕ mesons simulated with the taste-singlet vector.

Ensemble	$a_{\phi,\gamma_\mu\otimes 1}$	$Z_{\gamma_\mu\otimes 1}$	$a_{\phi,\gamma_\mu\otimes\gamma_\mu}$	$Z_{\gamma_\mu\otimes\gamma_\mu}$
1	0.0755(33)	1.109(10)	0.0849(20)	1.007(12)
2	0.0803(17)	1.109(10)	0.0899(23)	1.003(9)
3	0.0490(16)	1.064(5)	0.0527(14)	1.009(11)

Table 7.2: A table of the fit amplitudes, a_ϕ, and normalisation factors, Z, calculated on the lattice and used to extract f_ϕ. The data for the 1-link vector is on the left and the data for the local vector on the right.

The decay constant, f_ϕ, is extracted from the fit by

$$\frac{f_\phi}{Z} = \sqrt{\frac{2}{m_\phi}} a_\phi. \tag{7.8}$$

The decay constant is related to $\Gamma_{\phi\to e^+e^-}$ by

$$\Gamma_{\phi\to e^+e^-} = \frac{4\pi}{3}\alpha_{QED}^2 e_Q^2 \frac{f_\phi^2}{m_\phi} \tag{7.9}$$

and $\Gamma_{\phi\to e^+e^-} = 1.27(4)$ keV in the PDG [5], which can be used to find the continuum $f_\phi = 227(4)$ MeV.

The fit amplitudes, a_ϕ, to the lattice data are in Table 7.2 along with the Z factors needed to normalise the local and 1-link vector currents. The amplitudes and normalisation factors for the 1-link operator are in columns 2 and 3 and the number for the local operator are in columns 4 and 5. Both the 1-link and local Z factors are calculated nonperturbatively using pseudoscalar to pseudoscalar meson transitions. These

calculations are discussed in Section 7.2.

The lattice results for f_ϕ are plotted in Figure 7.2, along with the continuum value. The decay constants extracted using the local and 1-link ϕ mesons agree after being normalised. The values of f_ϕ on all the ensembles are 10% higher than the continuum. In the decay $\phi \to e^+e^-$, the ϕ meson's valence $s\bar{s}$ quarks annihilate. This process is affected by coupling to $K\bar{K}$ states, which is suppressed in the lattice calculation by the large K mass.

7.2 Z factors for f_ϕ

To extract the correctly normalised decay constant from the local and 1-link ϕ meson correlators, the $s\bar{s}$ vector operators used in the calculations need to be renormalised. The methods used to normalise them are similar as both are based on symmetric pseudoscalar to pseudoscalar meson transitions and closely resemble the calculation of the $c\bar{c}$ local vector normalisation in Section 5.4.

7.2.1 1-link vector, $\gamma_\mu \otimes 1$

The matrix element for a general pseudoscalar to pseudoscalar meson transition between mesons P and P' with respective momenta p and p' can be written as

$$\langle P(p)|V_\mu|P'(p')\rangle = f_+(q^2)\left[p^\mu + p'^\mu - \frac{m_P^2 - m_{P'}^2}{q^2}q^\mu\right] + f_0(q^2)\frac{m_P^2 - m_{P'}^2}{q^2}q^\mu, \quad (7.10)$$

where P and P' are pseudoscalar mesons with momenta p and p' and masses M_P and M'_P respectively and $q^\mu = p'^\mu - p^\mu$.

When $q^2 = 0$, the form factors $f_+(0)$ and $f_0(0)$ are equal. This can be used to normalise the vector current by making a 3-point function with identical mesons at the source and sink. Equation 7.10 reduces to

$$\langle P(p)|V_\mu|P(p)\rangle = 2p^\mu f_+(0) = 2p^\mu, \quad (7.11)$$

where $f_+(0) = f_0(0) = 1$ for identical mesons at each end of the 3-point function.

It is particularly easy to normalise the taste-singlet vector operator in this way because a staggered propagator can be used as the spectator quark in the 3-point correlator. The taste-singlet Z factors were calculated by Jonna Koponen using a symmetric $D_s \to D_s$ 3-point function [56] and are given in Table 7.2 as $Z_{\gamma_\mu\otimes 1}$.

7.2.2 Local vector, $\gamma_\mu \otimes \gamma_\mu$

As the local vector operator is not a taste-singlet, it cannot simply be inserted into a pseudoscalar to pseudoscalar symmetric 3-point function where staggered quarks are used for each of the propagators. However, as in Section 5.4, it can be normalised using

Ensemble	am_h	T values	V_{00}	Z
1	2.0	15,16,20,21	0.992(12)	1.007(12)
2	2.0	15,16,20,21	0.996(10)	1.003(9)
	2.8	15,16,20,21	1.003(14)	0.996(13)
3	1.5	24,25,30,31	0.990(11)	1.009(11)

Table 7.3: The Z factors on each ensemble for the local $\bar{s}(\gamma_\mu \otimes \gamma_\mu)s$ operator. 4 time sources were used per configuration. The NRQCD masses used are given in column 2. For ensemble 2, two masses were used for the NRQCD spectator quark. Column 3 gives the values of T used for the 3-point correlators and columns 4 and 5 give the fit parameter V_{00} and Z factor which are related by $V_{00} = Z^{-1}$.

a 3-point function where the spectator quark retains 4 spin components. As before, NRQCD is used for the spectator quark.

It is simplest to normalise the temporal vector current, as for charm. As before, the 3-point correlation function used is

$$C_{3pt}(0,t,T) = \sum_{i,j,k} (-1)^{k_x+k_y+k_z+k_t}(-1)^{j_t} \times \mathrm{Tr_c}\left\{\mathrm{Tr_s}\left[\gamma_t \Omega^\dagger(i) G_{NRQCD}(i,k)\Omega(k)\right] g(k,j) g^\dagger(i,j)\right\}, \tag{7.12}$$

where $i_t = 0$, $j_t = t$ and $k_t = T$, $\mathrm{Tr_c}$ indicates a trace over colour indices and $\mathrm{Tr_s}$ a trace over spin. Note that Equation 7.12 is the same as Equation 5.24, except that the staggered propagators are now strange propagators rather than charm.

The results are given in Table 7.3. Up to discretisation effects, Z does not depend on the details of the spectator quark. On ensemble 2, the Z factor was calculated using two values of the heavy NRQCD quark mass, am_h, and the results agree within the statistical errors. The Z factors used to normalise the current for f_ϕ are the ones obtained with $am_h = 2.0$ for the coarse ensembles 1 and 2 and $am_h = 1.5$ for the fine ensemble 3. These NRQCD masses correspond to approximately the same physical quark mass.

7.3 Form factor calculations

The $D_s \to \phi$ form factors are calculated on the lattice using 3-point correlation functions set up as in Figure 7.3. The operators used in the calculation are chosen so they contain at most one link of point splitting. Each independent form factor is calculated in turn by choosing the kinematics such that Equation 7.1 simplifies. The D_s meson was kept at rest for all the form factor calculations and was a time distance T from the source, as in Figure 7.3. Propagators 1 and 3 in Figure 7.3 are strange quark propagators and propagator 2 a charm propagator. The kinematics were adjusted by using twisted boundary conditions with different twists, θ, applied to propagator 3, so only the ϕ meson carries spatial momentum.

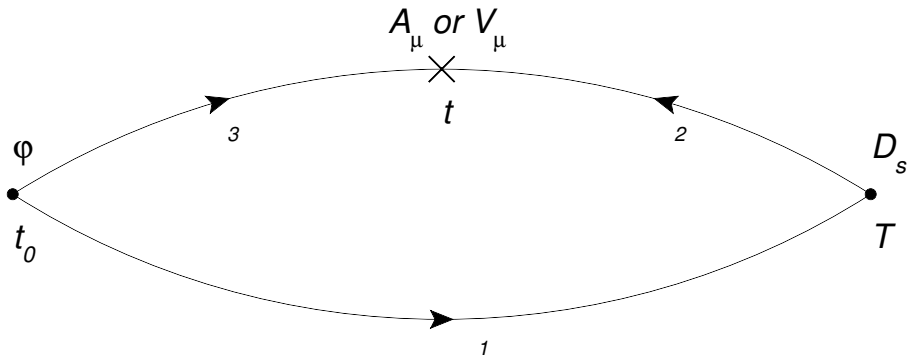

Figure 7.3: The propagators in the 3-point correlators used to calculate the form factors for $D_s \to \phi\ell\nu$. A ϕ meson is created at time t_0 and a D_s is destroyed at time T. At time t satisfying $t_0 < t < T$, there is a weak flavour-changing vector or axial vector current.

7.3.1 $A_1(q^2)$

At rest, $A_1(q^2)$ is the only term that remains and it can be isolated at any q^2 by ensuring $\varepsilon \cdot q = 0$. This is the physical form factor which dominates the decay rate, so it important to achieve good statistical errors in the lattice calculation.

When the kinematics are set up such that $\varepsilon \cdot q = 0$, the transition matrix element becomes

$$\langle \phi(p', \varepsilon) | A^\mu | D_s(p) \rangle = (m_{D_s} + m_\phi) \varepsilon^\mu A_1(q^2). \tag{7.13}$$

There is a choice of operators that can be used to extract $A_1(q^2)$; either using a local vector operator for the ϕ and local axial vector for the current or a 1-link vector and 1-link axial vector. Using the 1-link ϕ and axial vector, in which the vector has spin-taste $\gamma_\mu \otimes 1$ and the axial vector has spin-taste $\gamma_5\gamma_\mu \otimes \gamma_5$,

$$\langle \bar{\psi}(i)\gamma_\mu \psi(i + \hat{\mu})\ \bar{\psi}(j)\gamma_5\gamma_\nu \psi(j + \hat{\nu})\ \bar{\psi}(k)\gamma_5 \psi(k) \rangle \tag{7.14}$$

gives a staggered 3-point correlator

$$C_{3pt}(0, t, T) = \sum_{i,j,k} (-1)^{i_\mu^< + j_\nu^-} \varepsilon(i)\varepsilon(k) \times \mathrm{Tr}\left[g_s(i,k) g_c(k,j) g_s^{\theta\dagger}(i \pm \hat{\mu}, j \pm \hat{\nu}) \right]. \tag{7.15}$$

In the above, the points i, j, k are on timeslices $i_t = 0$, $j_t = t$ and $k_t = T$ and $i \pm \hat{\mu}$ indicates an average over the forward and backwards links in the μ direction. The ϕ polarisation vector and the axial vector current must be in the same direction. Unlike the $J/\psi \to \eta_c\gamma$ calculation, the directions for the momenta and polarisation vectors have not been chosen explicitly as different directions are averaged over in the analysis.

Using only local operators

$$\langle \bar{\psi}(i)\gamma_\mu \psi(i)\ \bar{\psi}(j)\gamma_5\gamma_\nu \psi(j)\ \bar{\psi}(k)\gamma_5 \psi(k) \rangle \tag{7.16}$$

has the staggered 3-point correlation function

$$C_{3pt}(0,t,T) = \sum_{i,j,k} (-1)^{i_\mu + j_\nu^<} \varepsilon(k) \times \mathrm{Tr}\left[g_s(i,k) g_c(k,j) g_s^{\theta\dagger}(i,j)\right]. \tag{7.17}$$

Again the sites i, j, k are on timeslices $i_t = 0$, $j_t = t$ and $k_t = T$.

The two determinations of $A_1(q^2)$ should agree with one another, as the current operators only differ by taste and the different ϕ mesons also agree.

The 1-link determination of $A_1(q^2)$ uses the 1-link axial vector operator, $\gamma_5\gamma_\mu \otimes \gamma_5$, for the weak current so it must be normalised to complete the calculation. The local axial vector, $\gamma_5\gamma_\mu \otimes \gamma_5\gamma_\mu$, also needs to be normalised for the calculation of $A_1(q^2)$ using local operators. The methods used to normalise the currents are described in Section 7.4.

All the form factors are plotted for ensemble 1 in Figure 7.4, with the 1-link and local determinations of $A_1(q^2)$ plotted separately. This plot includes the Z factors required for each form factor. The two lattice results agree, but the local method is preferable as it has smaller statistical errors. The lattice data for all the ensembles in plotted in Figure 7.8 in z-space.

7.3.2 $A_0(q^2)$

The $A_0(q^2)$ form factor can be related to the pseudoscalar density using the PCAC relation. The PCAC relation applied to Equation 7.1 gives

$$\begin{aligned} q_\mu \langle \phi(p',\varepsilon)|A^\mu|D_s(p)\rangle &= 2m_\phi \varepsilon \cdot q A_0(q^2) \\ &= (m_c + m_s)\langle \phi(p',\varepsilon)|\gamma_5|D_s(p)\rangle. \end{aligned} \tag{7.18}$$

$A_0(q^2)$ is then easily extracted from Equation 7.18. It cannot be calculated at rest because $\varepsilon \cdot q$ must be non-zero for the matrix element to be non-zero. In the matrix element for $D_s \to \phi$, the term containing $A_0(q^2)$ is proportional to q^μ, so it isn't experimentally accessible. However, calculating both $A_0(q^2)$ and $A_1(q^2)$ is the easiest way to extract $A_2(q^2)$.

The staggered 3-point correlator simulated on the lattice is

$$C_{3pt}(0,t,T) = \sum_{i,j,k} (-1)^{i_\mu^<} \varepsilon(i)\varepsilon(j)\varepsilon(k) \times \mathrm{Tr}\left[g_s(i,k) g_c(k,j) g_s^{\theta\dagger}(i \pm \hat{\mu}, j)\right]. \tag{7.19}$$

As before the sum of i, j and k is over space, but not time.

The $A_0(q^2)$ form factor is plotted in Figure 7.4 for ensemble 1 and for all ensembles in z-space in Figure 7.8. No normalisation factor is needed for $A_0(q^2)$ because the local pseudoscalar operator is used to extract it and that operator is absolutely normalised for staggered quarks.

7.3.3 $A_2(q^2)$

It is difficult to isolate $A_2(q^2)$, but it can be extracted using a combination of $A_1(q^2)$ and $A_0(q^2)$.

At $q^2 = 0$, the relation $A_3(0) = A_0(0)$ can be used to extract $A_2(0)$ from $A_0(0)$ and $A_1(0)$. The relations between $A_0(q^2)$, $A_1(q^2)$ and $A_2(q^2)$ at non-zero q^2 are more complicated but can be applied to get $A_2(q^2)$ using knowledge of $A_0(q^2)$ and $A_1(q^2)$ by calculating

$$\langle\bar{\psi}(i)\gamma_\mu\psi(i+\hat{\mu})\ \bar{\psi}(j)\gamma_5\gamma_\nu\psi(j+\hat{\nu})\ \bar{\psi}(k)\gamma_5\psi(k)\rangle \tag{7.20}$$

without the kinematic constraint $\varepsilon \cdot q = 0$. The corresponding expression in term of staggered propagators and phases is

$$C_{3pt}(0,t,T) = \sum_{i,j,k}(-1)^{i_\mu^< + j_\nu^-}\varepsilon(i)\varepsilon(k) \times \mathrm{Tr}\left[g_s(i,k)g_c(k,j)g_s^{\theta\dagger}(i \pm \hat{\mu}, j \pm \hat{\nu})\right], \tag{7.21}$$

with the sum over space. This is the same calculation as for the 1-link determination of $A_1(q^2)$, except without choosing the ϕ polarisation and momentum to ensure $\varepsilon \cdot q = 0$ Then all the form factors will contribute to the matrix element and a value for $A_2(q^2)$ can be calculated.

The operator used for the weak current in the $A_2(q^2)$ calculation is the 1-link $\gamma_5\gamma_\mu \otimes \gamma_5$, which is the same operator that needs to be normalised for the 1-link determination of $A_1(q^2)$.

Along with the other form factors, the normalised $A_2(q^2)$ is shown in Figure 7.4 for ensemble 1 and in Figure 7.8 for all ensembles in z-space.

7.3.4 $V(q^2)$

The vector form factor is calculated by putting in a V_μ current and setting up the right kinematics. The matrix element and form factor (between a pseudoscalar and vector state) are defined the same way as for $J/\psi \to \eta_c\gamma$.

$V(q^2)$ is calculated using the non-Goldstone D_s and a 1-link vector operator for the ϕ where the point-splitting is in a different spatial direction to the vector. In spin-taste notation, this operator is $\gamma_\mu \otimes \gamma_\mu\gamma_\nu$. The 3-point function has the D_s at rest and becomes

$$\langle\bar{\psi}(i)\gamma_\mu\psi(i+\hat{\nu})\ \bar{\psi}(j)\gamma_\alpha\psi(j)\ \bar{\psi}(k)\gamma_5\gamma_t\psi(k)\rangle \tag{7.22}$$

With staggered propagators and phase factors this is

$$C_{3pt}(0,t,T) = \sum_{i,j,k}(-1)^{i_\nu^> + i_\mu + j_\alpha + k_t} \times \mathrm{Tr}\left[g_s(i,k)g_c(k,j)g_s^{\theta\dagger}(i \pm \hat{\nu}, j)\right], \tag{7.23}$$

and the sums are over sites on the same timeslice and it should be noted that the D_s is at rest and the ϕ is the meson with spatial momentum.

With these kinematics, the general form of the matrix element reduces to

$$\frac{2i\epsilon_{\mu\nu\alpha t}}{m_{D_s}+m_\phi}\varepsilon^\mu E_{D_s} p_\phi^\nu V(q^2), \tag{7.24}$$

where the directions of the ϕ polarisation vector, the vector current and the ϕ momentum are the three spatial directions and E_{D_s} is the D_s energy. This means the momentum of the ϕ must be in the same direction as the point-splitting in the $\gamma_\mu \otimes \gamma_\mu\gamma_\nu$ vector operator.

The local vector is the operator that must be normalised for this form factor. Note that the normalisation for the charm-strange local vector current that appears here is not taken to be the same as for the local strange-strange vector used for the ϕ mesons because the quark masses are different.

The results for $V(q^2)$ – including the renormalisation factor – on ensemble 1 are shown in Figure 7.4 and the results for all ensembles in Figure 7.8 as a function of z.

7.3.5 Lattice data

For each ensemble, three values of $|\theta|$ were used: $|\theta| = 0$ which corresponds to q^2_{max}, $|\theta|$ tuned to $q^2 \simeq 0$ and an intermediate value of $|\theta|$. Only the form factor $A_1(q^2)$ contributes at q^2_{max}, but all the form factors were calculated at each finite momentum. Ensembles 2 and 3 are approximately the same physical size, so $|\theta| = 6$ was used as the intermediate value for both of them. The lattices in ensemble 1 are bigger, so the intermediate value of $|\theta| = 7$ was used. These values were chosen to be roughly in the middle of the physical range of q^2.

To tune to $q^2 = 0$, the ϕ meson should have momentum

$$|\vec{p}_\phi| = \frac{(m_\phi + m_{D_s})(m_{D_s} - m_\phi)}{2m_{D_s}}. \tag{7.25}$$

Unlike the $J/\psi \to \eta_c\gamma$ decay, where only $q^2 = 0$ was physical, the lepton-neutrino pair can have a continuous energy spectrum, so the total decay rate depends on all values of q^2 between 0 and q^2_{max}. Therefore, it is not important for the $D_s \to \phi$ decay kinematics to be tuned exactly to $q^2 = 0$.

For the coarse ensembles 1 and 2, the 3-point functions were calculated with $T = 12, 15, 18$, where both even and odd values of T are useful to understand the effects of oscillations in the fit. The values of T used on the finer ensemble 3 were $T = 16, 19, 20, 23$.

The 2-point and 3-point correlators with different T and p_ϕ were fitted simultaneously. Because the D_s 2-point data used for all the axial form factors is the same, the data for these form factors was also fitted simultaneously. The simultaneous fit takes account of the correlations between the form factors, which is used when they are combined to extract the differential decay rate. The values for q^2 corresponding to the momenta p_ϕ used in the simulations are also found from the masses and energies

in the fit.

The lattice results are taken from a fit with 6 exponentials and 5 oscillating exponentials for all the correlators. The priors for the ground state energies of the D_s and ϕ are from the correlator effective mass. The priors for the separation between successive energy levels was 600(300) MeV and the lowest oscillating state prior was 600(300) MeV above the non-oscillating ground state. The 2-point fit amplitudes, a_A, had priors of 0.01(0.5) and are shared parameters between the 2-point and 3-point correlators in the fit. The 3-point amplitudes, V_{AB}, had priors of 0.01(0.25).

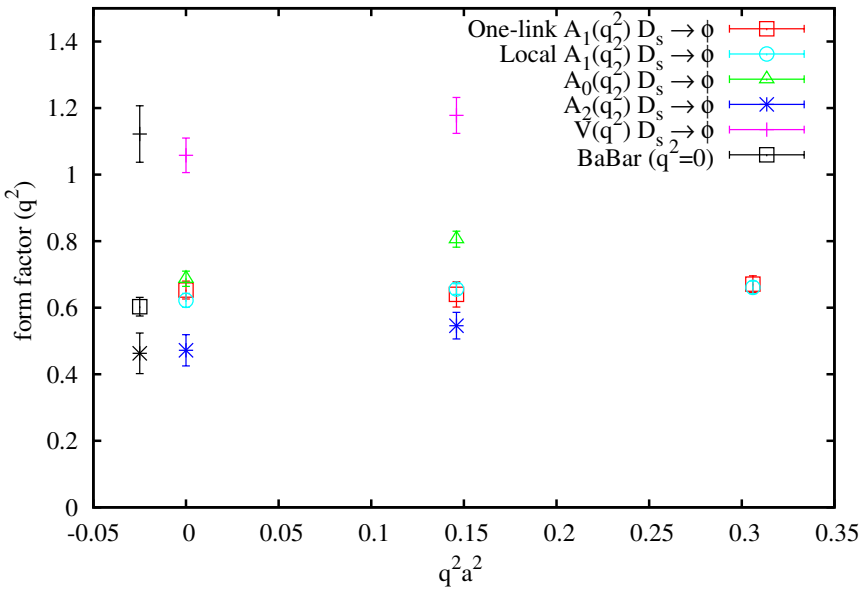

Figure 7.4: The nonperturbatively normalised form factors in q^2 space for ensemble 1. Each of the vector and axial vector form factors is plotted. Both the local and 1-link determinations of $A_1(q^2)$ are shown. The black points, slightly offset from $q^2 = 0$, are the experimental extractions of the form factors at $q^2 = 0$ from BaBar's paper [77].

Figure 7.4 shows the lattice data for all the form factors at all values of q^2 calculated on ensemble 1. These include the Z factors for each of the form factors. Only one ensemble is shown here to avoid clutter, but all the lattice data is shown in z-space in Figure 7.8.

In [77], BaBar quote the results they extract from their data for $A_1(0)$ and the ratios $r_2 = A_2(0)/A_1(0)$ and $r_V = V(0)/A_1(0)$. The black points, slightly offset from $q^2 = 0$ are BaBar's quoted $A_1(0)$ and the values of $A_2(0)$ and $V(0)$ then extracted from the ratios r_2 and r_V.

The lattice data for the form factors is given in Table 7.4. Column 2 states which form factor is given in each row and the value of that form factor (after applying the Z factor) is given in the right-most column.

Ens.	Form factor	T values	am_{D_s}	θ	aE_ϕ	$F(q^2)$
1	Local $A_1(q^2)$	12,15,18	1.1890(1)	0.0	0.6369(31)	0.679(10)
1	Local $A_1(q^2)$	12,15,18	1.1890(1)	7.0	0.7111(39)	0.658(11)
1	Local $A_1(q^2)$	12,15,18	1.1890(1)	10.18	0.7829(56)	0.632(18)
1	1-link $A_1(q^2)$	12,15,18	1.1890(1)	0.0	0.6339(50)	0.685(20)
1	1-link $A_1(q^2)$	12,15,18	1.1890(1)	7.0	0.7068(47)	0.656(20)
1	1-link $A_1(q^2)$	12,15,18	1.1890(1)	10.18	0.7832(64)	0.650(24)
1	$A_0(q^2)$	12,15,18	1.1890(1)	7.0	0.7096(34)	0.808(20)
1	$A_0(q^2)$	12,15,18	1.1890(1)	10.18	0.7781(39)	0.710(18)
1	$A_2(q^2)$	12,15,18	1.1890(1)	7.0	0.7096(34)	0.524(93)
1	$A_2(q^2)$	12,15,18	1.1890(1)	10.18	0.7781(39)	0.452(72)
1	$V(q^2)$	12,15,18	1.1909(5)	7.0	0.7121(41)	1.141(72)
1	$V(q^2)$	12,15,18	1.1909(5)	10.18	0.7853(58)	1.050(63)
2	Local $A_1(q^2)$	12,15,18	1.2015(1)	0.0	0.6550(30)	0.691(12)
2	Local $A_1(q^2)$	12,15,18	1.2015(1)	6.0	0.7192(60)	0.626(26)
2	Local $A_1(q^2)$	12,15,18	1.2015(1)	8.39	0.7768(76)	0.595(29)
2	1-link $A_1(q^2)$	12,15,18	1.2015(1)	0.0	0.6568(28)	0.684(12)
2	1-link $A_1(q^2)$	12,15,18	1.2015(1)	6.0	0.7248(50)	0.629(20)
2	1-link $A_1(q^2)$	12,15,18	1.2015(1)	8.39	0.7709(107)	0.583(43)
2	$A_0(q^2)$	12,15,18	1.2015(1)	6.0	0.7155(51)	0.796(29)
2	$A_0(q^2)$	12,15,18	1.2015(1)	8.39	0.7827(41)	0.701(20)
2	$A_2(q^2)$	12,15,18	1.2015(1)	6.0	0.7155(51)	0.436(186)
2	$A_2(q^2)$	12,15,18	1.2015(1)	8.39	0.7827(41)	0.342(112)
2	$V(q^2)$	12,15,18	1.2039(3)	6.0	0.7202(57)	1.109(76)
2	$V(q^2)$	12,15,18	1.2039(3)	8.39	0.7739(80)	1.014(155)
3	Local $A_1(q^2)$	16,19,20,23	0.8460(2)	0.0	0.4594(16)	0.703(8)
3	Local $A_1(q^2)$	16,19,20,23	0.8460(2)	6.0	0.5024(35)	0.630(13)
3	Local $A_1(q^2)$	16,19,20,23	0.8460(2)	8.39	0.5499(48)	0.596(15)
3	1-link $A_1(q^2)$	16,19,20,23	0.8460(2)	0.0	0.4565(29)	0.701(9)
3	1-link $A_1(q^2)$	16,19,20,23	0.8460(2)	6.0	0.4990(47)	0.653(14)
3	1-link $A_1(q^2)$	16,19,20,23	0.8460(2)	8.39	0.5464(53)	0.653(19)
3	$A_0(q^2)$	16,19,20,23	0.8460(2)	6.0	0.4960(50)	0.814(35)
3	$A_0(q^2)$	16,19,20,23	0.8460(2)	8.39	0.5504(30)	0.683(13)
3	$A_2(q^2)$	16,19,20,23	0.8460(2)	6.0	0.4960(50)	0.408(61)
3	$A_2(q^2)$	16,19,20,23	0.8460(2)	8.39	0.5504(30)	0.445(36)
3	$V(q^2)$	16,19,20,23	0.8465(4)	6.0	0.5063(39)	1.076(135)
3	$V(q^2)$	16,19,20,23	0.8465(4)	8.39	0.5451(64)	1.140(116)

Table 7.4: The form factor data for $D_s \to \phi$ for all the form factors on each ensemble at all values of q^2 calculated. Column 2 states which form factor the data is for and the value is in column 7. The axial form factors are fitted simultaneously so the D_s mass is the same for all of them on the same ensemble. The vector form factor $V(q^2)$ is calculated using the non-Goldstone D_s. Columns 5 and 6 give the value of θ used to give momentum to the ϕ and the ϕ energy at this momentum.

Ensemble	$Z_{\gamma_5\gamma_\mu\otimes\gamma_5}$	$Z_{\gamma_5\gamma_\mu\otimes\gamma_5\gamma_\mu}$	$Z_{\gamma_\mu\otimes\gamma_\mu}$
1	1.065(7)	1.038(3)	1.027(3)
2	1.065(5)	1.036(4)	1.020(10)
3	1.017(5)	1.020(6)	1.009(2)

Table 7.5: The Z factors on each ensemble for the 1-link axial vector, local axial vector and local vector operators. These are the operators which are used for the weak currents in the $D_s \to \phi\ell\nu$ calculations.

7.4 Z factors for weak currents in $D_s \to \phi\ell\nu$

As discussed in the previous sections, various axial and vector operators are used for the weak currents in the form factor calculations and need to be nonperturbatively normalised. The methods used to extract the Z factors will be described in the following subsections and the resultant charm-strange vector and axial vector current renormalisation factors obtained are collected in Table 7.5.

7.4.1 1-link axial vector, $\gamma_5\gamma_\mu \otimes \gamma_5$

The charm-strange 1-link A_μ current is used in the matrix elements to extract the $A_1(q^2)$ and $A_2(q^2)$ form factors. It can be normalised by calculating

$$C_{PS\to AV}(t) = \langle\bar{\psi}(i)\gamma_5\psi(i)\ \bar{\psi}(j)\gamma_5\gamma_\mu\psi(j \pm \hat{\mu})\rangle \tag{7.26}$$

and fitting simultaneously with

$$C_{PS\to PS}(t) = \langle\bar{\psi}(i)\gamma_5\psi(i)\ \bar{\psi}(j)\gamma_5\psi(j)\rangle, \tag{7.27}$$

where $i_t - j_t = t$ and the sites i and j are summed over timeslices.

This works because $\gamma_5\gamma_\mu \otimes \gamma_5$ couples to the same pseudoscalar states as $\gamma_5 \otimes \gamma_5$, but with a different amplitude. When they are dominated by the ground state, the correlator $C_{PS\to PS}(t) = a_{PS}^2 e^{-mt}$ and $C_{PS\to AV} = a_{PS}a_{AV}e^{-mt}$.

The fit amplitudes a_{PS} and a_{AV} can be related using the PCAC relation by

$$p_\mu\langle 0|A_\mu|P_0\rangle = (m_1 + m_2)\langle 0|\gamma_5|P_0\rangle. \tag{7.28}$$

Introducing the Z factor for the lattice axial vector operator means the amplitudes are related as

$$Za_{AV} = \frac{m_1 + m_2}{m_{P_0}^2}p_\mu a_{PS}. \tag{7.29}$$

The valence quark masses are m_1 and m_2 and the pseudoscalar meson mass is m_{P_0}.

In a plot of the ratio of amplitudes against momentum, the Z factor can be extracted from the gradient. In Figure 7.5, this is plotted for pseudoscalar mesons containing charm and strange quarks on ensemble 2.

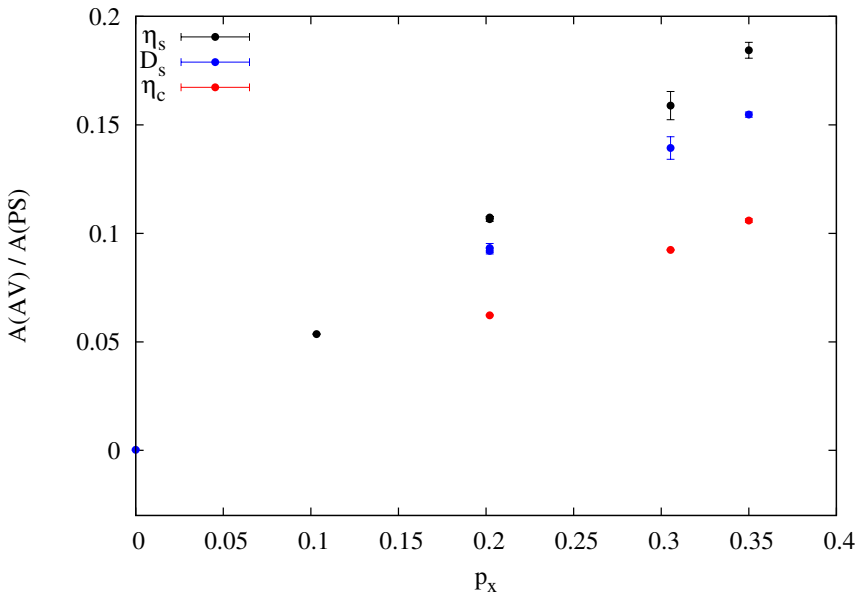

Figure 7.5: The Z factors for the 1-link axial vector operator can be extracted from the gradient of the ratio of axial vector to pseudoscalar amplitudes plotted against momentum. The D_s meson is the one created using the charm-strange axial vector current used the semileptonic decay simulation. The gradient of the ratio against momentum is $\frac{1}{Z}\frac{m_1+m_2}{m^2_{P_0}}$.

For the flavour-nonsinglet D_s, there is a difference observed in the ratio whether the momentum is carried by the charm or strange quark. The difference in the ratio comes from the axial vector amplitude, which is related to the 1-link axial operator $\gamma_5\gamma_\mu \otimes \gamma_5$. The momentum of the D_s in Figure 7.5 is carried by the strange propagator.

This effect is shown most clearly by considering D_s mesons in which both propagators carry the same momentum. This should correspond to a total meson momentum of 0 because the quark and antiquark momenta are in opposite directions. The ratio of the axial vector to pseudoscalar amplitude for D_s mesons with equal and opposite momentum in each propagator is shown in Figure 7.6. As the D_s meson is at rest, it is expected that the ratio should be zero, but it is proportional to θ_μ, the momentum carried by each quark. The blue squares are calculated on the coarse ensemble 2 and the red circle on ensemble 3.

These ensembles have the same physical size, so equal θ on these ensembles correspond to approximately the same physical momentum. From the points on each ensemble with $\theta_x \simeq 6$, it can be seen that the ratio is further from the expected zero on the coarse ensemble than on the fine. This suggests that the discrepancy is a discretisation effect. The ratio for these points with the same physical momentum is plotted against a^2 in Figure 7.7, which shows the difference of the axial vector amplitude from zero vanishes as $a^2 \to 0$, as it should for a discretisation effect.

The 1-link axial vector Z is calculated with the momentum in the strange quark

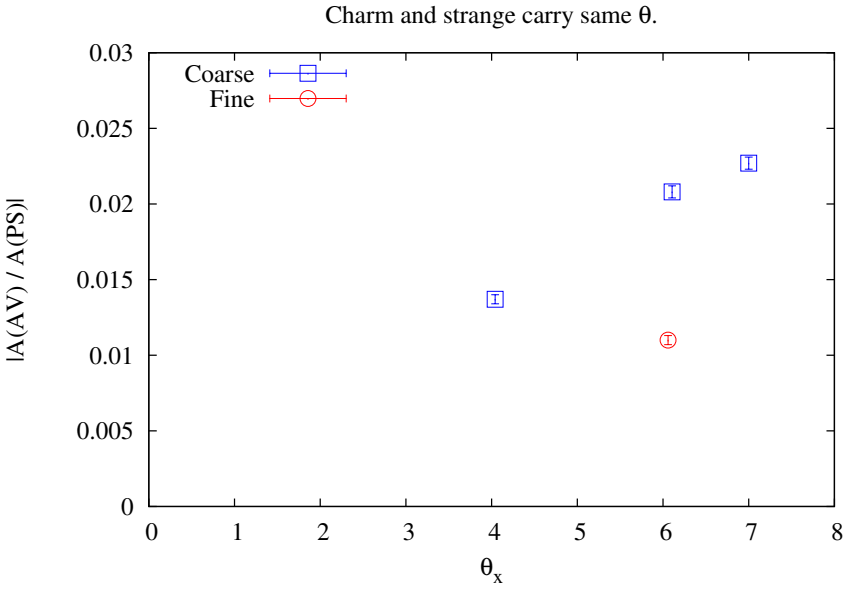

Figure 7.6: The ratio of amplitudes for D_s mesons in which both the charm and strange quarks carry the same momentum. In this case, the axial vector amplitude is expected to be zero. For the coarse data, the difference from zero is proportional to p_μ. The difference is less on the fine ensemble.

Ensemble	$am_{D_s}(\gamma_5 \otimes \gamma_5)$	$am_{D_s}(\gamma_5\gamma_t \otimes \gamma_5\gamma_t)$
1	1.1891(2)	1.1913(4)
2	1.2015(1)	1.2041(1)
3	0.8466(1)	0.8470(2)

Table 7.6: The masses of the Goldstone and non-Goldstone D_s mesons. The taste splitting is less than 4 MeV for all ensembles.

propagator. This matches the appearance of these currents in the form factor calculations, where the momentum is carried by the strange quark. The Z factors are given in Table 7.5.

7.4.2 Local axial vector, $\gamma_5\gamma_\mu \otimes \gamma_5\gamma_\mu$

The temporal component of the local axial vector can be normalised by comparing Goldstone and non-Goldstone pseudoscalar mesons. Non-Goldstone pseudoscalar mesons are created by the operator $\bar{\psi}(i)\gamma_5\gamma_t\psi(i)$, which has the same J^{PC} as the Goldstone. For D_s mesons containing the necessary charm and strange quarks, the amplitudes of the Goldstone and non-Goldstone 2-point functions are related by

$$ZE_{D_s}a_{NG} = (m_c + m_s)a_G, \tag{7.30}$$

where a Z factor is included for the local axial operator. The Z factor for this operator is given in Table 7.5.

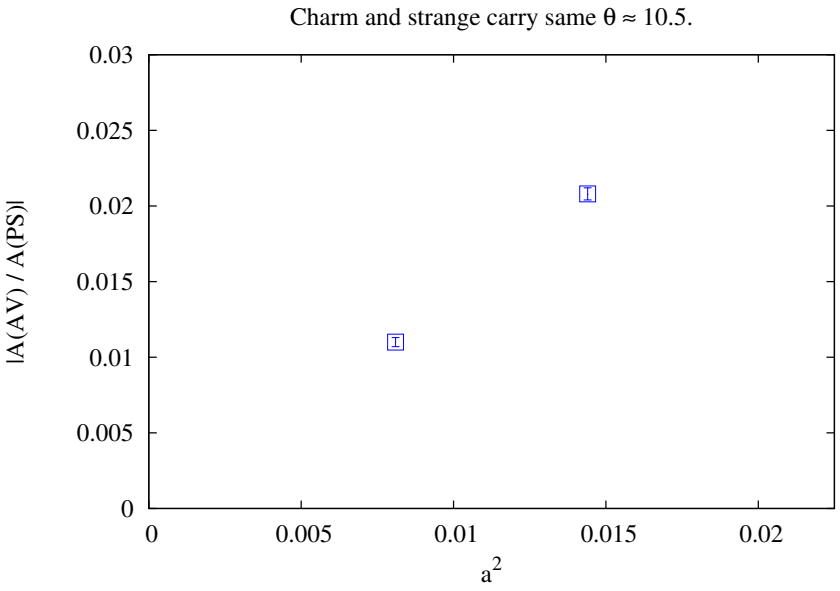

Figure 7.7: The ratio of amplitudes for D_s mesons in which both the charm and strange quarks carry the same momentum on the coarse and fine ensembles. The same value of θ on these ensembles corresponds to the same physical momentum because the lattices have the same physical size. The size of this ratio (which is expected to be zero) decreases linearly with a^2, which shows it is a discretisation effect.

Table 7.6 gives the masses of Goldstone and non-Goldstone D_s mesons on the ensembles used in these calculations. The taste-splitting is less than 4 MeV on all ensembles. This means that either taste of pseudoscalar meson can be used for the D_s in simulations.

7.4.3 Local vector, $\gamma_\mu \otimes \gamma_\mu$

The taste-singlet vector operator, $\gamma_\mu \otimes 1$ was normalised by comparing it to the scalar current normalised by Jonna Koponen [83]. The local vector can be normalised using a non-Goldstone $D_s \to \eta_s$ 3-point correlator and comparing to the Goldstone $D_s \to \eta_s$ 3-point correlator with a known current normalisation. The Goldstone $D_s \to \eta_s$ calculation uses the taste-singlet vector current, whilst the non-Goldstone $D_s \to \eta_s$ uses the local (temporal) vector current. Replacing the Goldstone D_s with the non-Goldstone in the correlator is possible because the taste-splitting is so small.

The comparison is possible at all available values of q^2, but $q^2 = q^2_{max}$ – when both mesons are at rest – is used to extract Z, which is given in Table 7.5.

7.5 Physical extrapolation with the z-expansion

To get the form factors in the physical limit, they must be extrapolated to the continuum and to the physical light quark masses. The z-expansion is a convenient method for the extrapolating semileptonic form factors [84, 85, 86]. The z-expansion has been

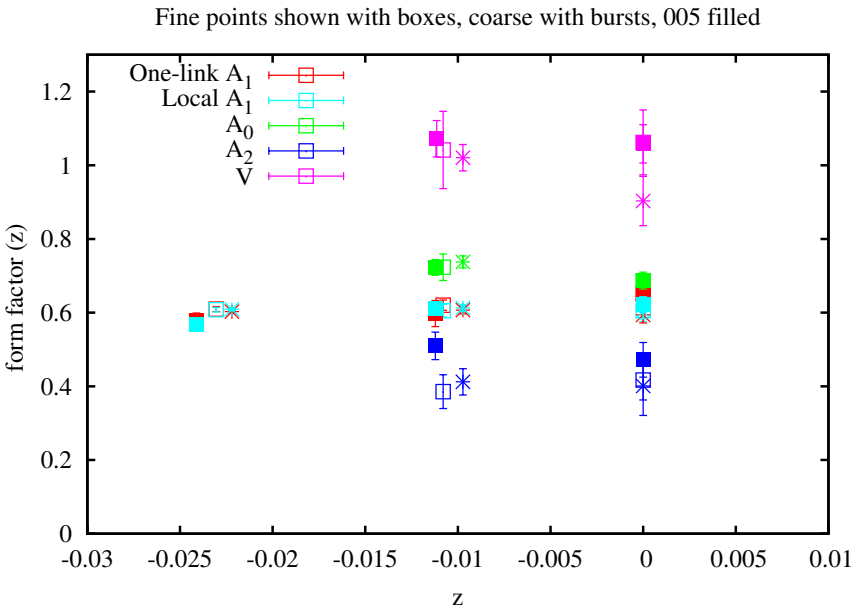

Figure 7.8: The form factors plotted in z space for all 3 ensembles. Both the local and 1-link determinations of $A_1(q^2)$ are shown in this plot. The lattice data for ensemble 1 is shown with filled squares, the data for ensemble 2 with bursts and the data for ensemble 3 with open squares.

used to simply extrapolate lattice QCD calculations of semileptonic form factors to the physical limit [87, 83].

The poles are removed from the form factor data as the q^2 dependence of the form factor is expected to be dominated by the pole [88]:

$$A_i(q^2) \to \left(1 - \frac{q^2}{m^2_{D_{s1}}}\right) A_i(q^2) \text{ and } V(q^2) \to \left(1 - \frac{q^2}{m^2_{D_s^*}}\right) V(q^2). \tag{7.31}$$

The pole masses are $m_{D_s^*} = 2112$ MeV for the vector and $m_{D_{s1}} = 2459$ MeV for the axial vector [5].

The data is converted to z-space using the transformation

$$z(q^2) = \frac{\sqrt{t_+ - q^2} - \sqrt{t_+}}{\sqrt{t_+ - q^2} + \sqrt{t_+}} \tag{7.32}$$

where $t_+ = (m_{D_s} + m_\phi)^2$. In the literature, there is often a t_0 term that can be chosen to shift the origin in z-space, but it does not appear in Equation 7.32 because it has been taken to be 0. This choice means that the point $q^2 = 0$ corresponds to $z = 0$.

The z-expansion is useful because it means the physical extrapolation can be done using a simple fit and high powers of z can be truncated because z is small for the physical range. For each of the form factors, here generically called $F(z)$, the fit

function is:

$$F(z) = F(0)\left\{1 + C_0^a\left(\frac{a}{r_1}\right)^2 + C_0^{a^2}\left(\frac{a}{r_1}\right)^4 + C_0^{ml}\left(\frac{m_l}{m_s} - \frac{m_l^{phys}}{m_s^{phys}}\right)\right\} + \sum_{A=1}^{3} C_A^z\left\{1 + C_A^a\left(\frac{a}{r_1}\right)^2 + C_A^{a^2}\left(\frac{a}{r_1}\right)^4 + C_A^{ml}\left(\frac{m_l}{m_s} - \frac{m_l^{phys}}{m_s^{phys}}\right)\right\} z^A \tag{7.33}$$

The continuum extrapolation is done with even powers of a/r_1 and the chiral dependence is fitted using the difference between the light to strange sea quark mass ratio on the lattice and in the continuum. The physical ratio used in the fit is $\frac{m_l^{phys}}{m_s^{phys}} = 0.0365$ [35]. The prior widths of the fits terms C_A^z are 2.0 and the widths for C_A^a, $C_A^{a^2}$ and C_A^{ml} are 1.0. These priors widths are around central prior values of zero. Each of the form factors – $A_1(q^2)$, $A_2(q^2)$ and $V(q^2)$ – is extrapolated together and the covariance matrix obtained from the simultaneous fit to the lattice data is included in the extrapolation.

7.5.1 Form factors in q^2 space

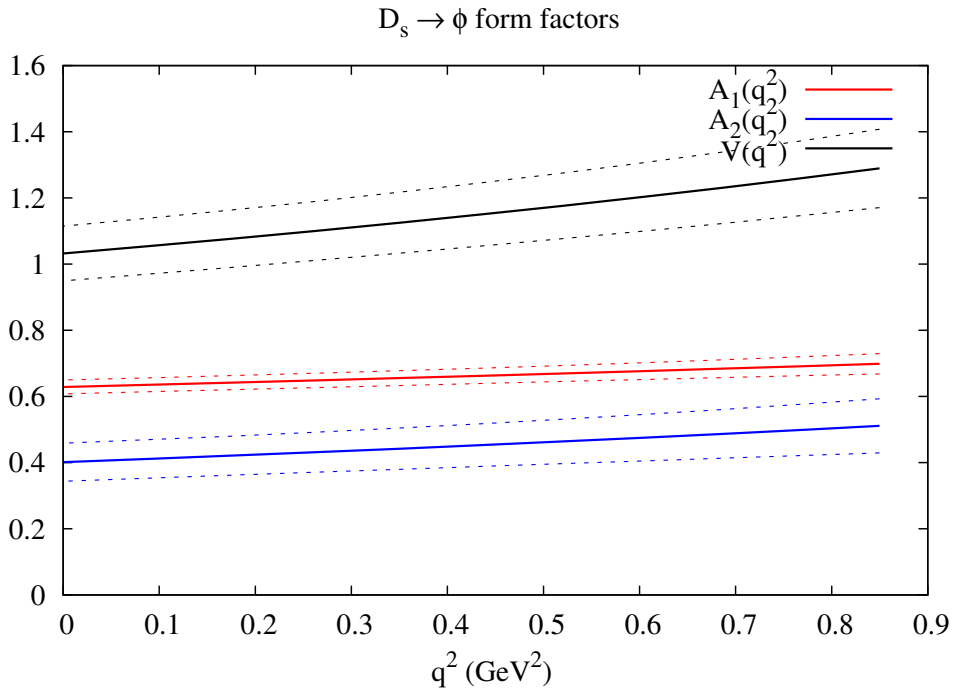

Figure 7.9: The physical form factors $A_1(q^2)$, $A_2(q^2)$ and $V(q^2)$ which contribute to the measured semileptonic decay after being transformed back to q^2 space. The central values are shown with solid lines and the uncertainties indicated by dashed lines.

After the extrapolations, the form factor are converted back to q^2 space using

$$q^2(z) = \frac{-4zt_+}{(1-z)^2} \tag{7.34}$$

and the poles are put back in.

The continuum form factors which result are plotted in Figure 7.9, where the range in q^2 goes from 0 to q^2_{max}. The form factors $A_1(q^2)$, $A_2(q^2)$ and $V(q^2)$ shown in Figure 7.9 are the ones which appear in the differential decay rate.

Over the range of q^2 for which they contribute, the form factors are consistent with the expectation that their behaviour is dominated by pole mass [88], but the range is too small to make a detailed comparison.

7.6 Comparison with experiment to extract V_{cs}

The observed final state for $D_s \to \phi\ell\nu$ is a lepton and a pair of kaons coming from the decay of the ϕ. The branching fraction for $\phi \to K^+K^-$ is 49.7% [5]. In [77], BaBar's measurements have a final state where ϕ has decayed to K^+K^- and the observed charged lepton is an electron.

7.6.1 Helicity amplitudes

The differential decay rate is given by [80]

$$\begin{aligned}\frac{d\Gamma(D_s \to \phi\ell\nu, \phi \to K^+K^-)}{dq^2 d\cos\theta_V d\cos\theta_\ell d\chi} &= \frac{3}{8(4\pi)^4} G_F^2 |V_{cs}|^2 \frac{p_\phi q^2}{m_{D_s}^2} \mathcal{B}(\phi \to K^+K^-) \\ &\times \{(1+\cos\theta_\ell)^2 \sin^2\theta_V |H_+(q^2)|^2 \\ &+ (1-\cos\theta_\ell)^2 \sin^2\theta_V |H_-(q^2)|^2 \\ &+ 4\sin^2\theta_\ell \cos^2\theta_V |H_0(q^2)|^2 \\ &+ 4\sin\theta_\ell(1+\cos\theta_\ell)\sin\theta_V \cos\theta_V \cos\chi H_+(q^2)H_0(q^2) \\ &- 4\sin\theta_\ell(1-\cos\theta_\ell)\sin\theta_V \cos\theta_V \cos\chi H_-(q^2)H_0(q^2) \\ &- 2\sin^2\theta_\ell \sin^2\theta_V cos2\chi H_+(q^2)H_-(q^2)\}.\end{aligned} \tag{7.35}$$

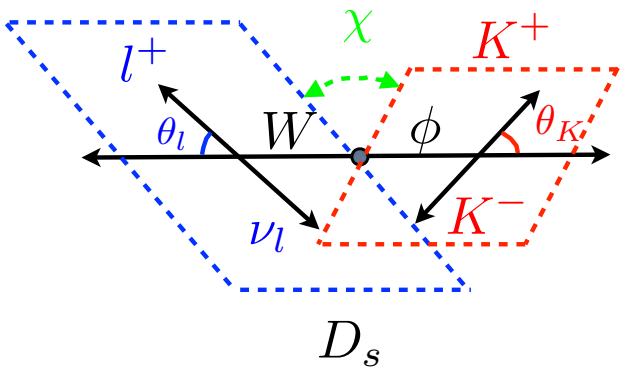

Figure 7.10: A picture of the angles in the definition of the differential decay rate. The definition of these angles is given in the text.

The experimental angles are shown in Figure 7.10. The angle θ_ℓ is defined as the angle between the momentum of the charged lepton and the momentum of the centre

of mass of the lepton-neutrino pair. The momentum of the centre of mass of the lepton-neutrino pair is the same as the $W^{\pm}$ boson's momentum before it decays. θ_V is defined as the angle between the momentum of one of the kaons (the K^+ for a D_s^+ decay, the K^- for a D_s^- decay) and the centre of mass momentum of the kaon pair. The angle χ is the angle between the planes defined by the K^+K^- pair and the lepton pair.

The differential decay rate includes the branching ratio $\mathcal{B}(\phi \to K^+K^-)$ for the ϕ meson decaying to charged kaons.

The helicity amplitudes are defined as

$$H_0(q^2) = \frac{1}{2m_\phi\sqrt{q^2}}[(m_{D_s}^2 - m_\phi^2 - q^2)(m_{D_s} + m_\phi)A_1(q^2) - 4\frac{m_{D_s}^2 p_\phi^2}{m_{D_s} + m_\phi}A_2(q^2)] \quad (7.36)$$

and

$$H_\pm(q^2) = (m_{D_s} + m_\phi)A_1(q^2) \mp \frac{2m_{D_s}p_\phi}{m_{D_s} + m_\phi}V(q^2). \quad (7.37)$$

Note that there is a factor of $p_\phi q^2$ in the phase space, so $H_0(q^2)$ does not diverge at $q^2 = 0$. All of the helicity amplitudes, and therefore the entire decay rate, are dominated by $A_1(q^2)$. The angular integrations in Equation 7.35 are straightforward and can be done analytically. The cross terms containing products of two helicity amplitude all have oscillatory χ dependence. When the differential decay rate is integrated over χ, they all vanish.

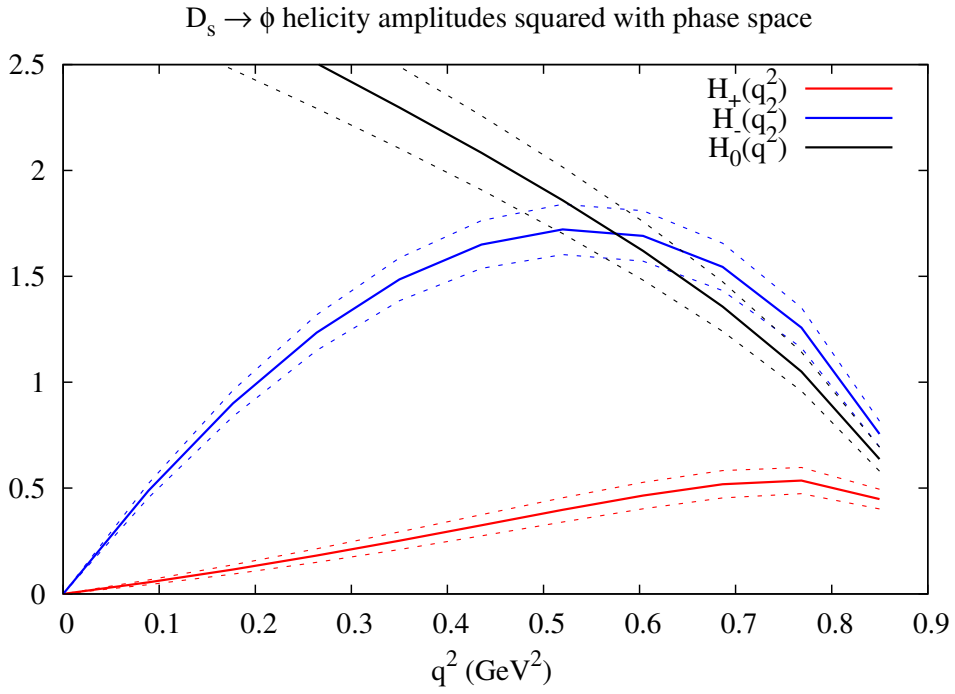

Figure 7.11: The helicity amplitudes plotted as $|H_i(q^2)|^2 p_\phi q^2$, so with the phase space measure included. The central values are shown with solid lines and the uncertainties indicated by dashed lines.

The helicity amplitudes can be constructed as combinations of the physical extrapolated form factors. They are plotted in Figure 7.11 as $|H_i(q^2)|^2 p_\phi q^2$, which is how they appear in the decay rate. At q^2_{max}, $p_\phi = 0$, so the helicity amplitudes go to zero at the $q^2 = q^2_{max}$ end of Figure 7.11 due to the phase space. The helicity amplitudes $H_\pm(q^2)$ vanish at $q^2 = 0$ too, also because of the phase space, but $H_0(q^2)$ does not due to the factor of q^{-2} in the definition of $|H_0(q^2)|^2$.

7.6.2 Decay distributions

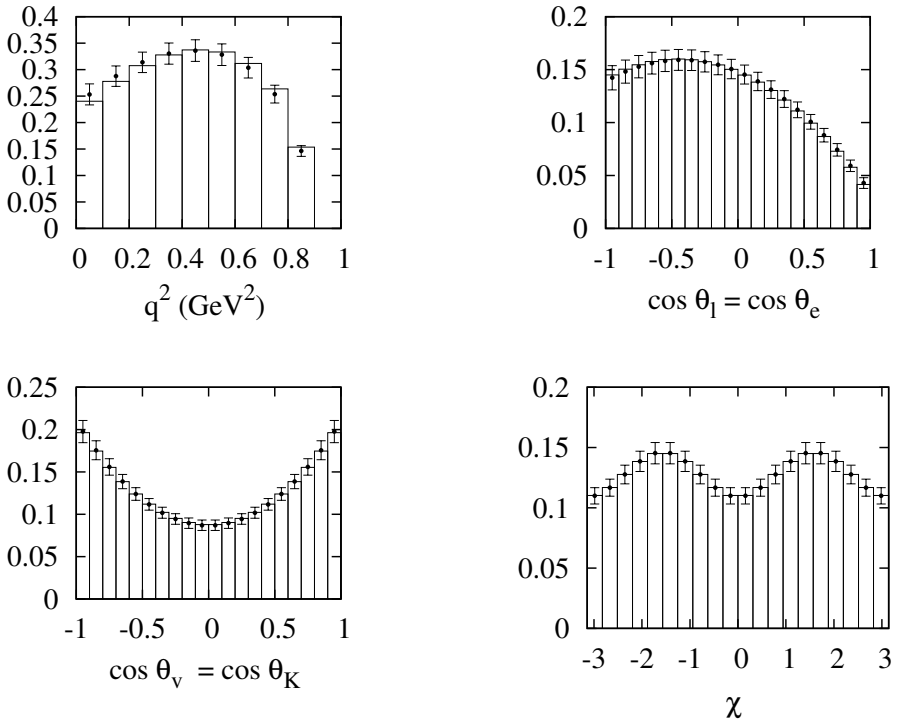

Figure 7.12: The decay rate plotted in bins of q^2 and the angles $\sin\theta_V$, $\sin\theta_\ell$ and χ. The points with error bars are from the lattice calculation and the bars are from the experimental measurements [77].

The differential decay rate is a function of q^2 and the three experimental angles. The decay distributions as a function of one of these variables can be found by integrating over the other three. The angular integrations can be done analytically and the integration over q^2 is done numerically. The decay rate distributions are shown in Figure 7.12, where the data points (with error bars) are the results of the lattice simulation and the bars are from experiment. Note that the experimental data is not the same as shown in [77]. This is because the distributions in [77] show the experimental data after applying cuts to the data (in particular, there is a cut of 500 MeV on the $e^\pm$ momentum). Instead, the bins show the decay rate reconstructed from BaBar's quoted fit parameters.

Apart from comparing the distributions, BaBar quote results for the ratios of form factors at $q^2 = 0$, $r_2 = A_2(0)/A_1(0) = 0.763(71)(65)$ and $r_V = V(0)/A_1(0) =$

1.849(60)(95). Using the physically extracted form factor plotted in Figure 7.9, my lattice results for the ratios are $r_2 = 0.77(9)$ and $r_V = 1.75(13)$, which are in agreement with experiment.

7.6.3 Extraction of the CKM element V_{cs}

The total decay rate (integrated over all the variables) calculated from the lattice simulation differs from experiment by the factor of $|V_{cs}|^2$ that is not included. Thus the total experimental decay rate given in [77] can be used to extract $|V_{cs}|$ using

$$\Gamma^{lattice} = |V_{cs}|^2 \Gamma^{experiment}, \tag{7.38}$$

which gives $|V_{cs}| = 0.975(48)$. The value of $|V_{cs}|$ extracted from the $D_s \to \phi\ell\nu$ decay

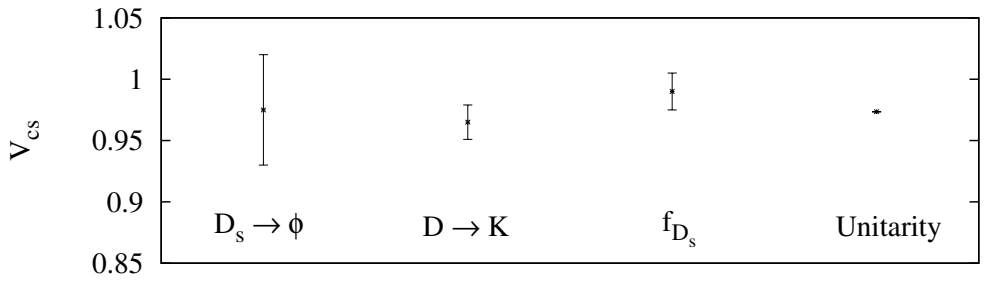

Figure 7.13: A comparisons of the value of $|V_{cs}|$ from the $D_s \to \ell\nu$ calculation with other determinations of $|V_{cs}|$. It can be extracted from comparing lattice calculations of the $D \to K\ell\nu$ decay rate to experimental measurements [83]. The D_s leptonic decay constant is compared to the $D_s \to \tau\nu$ decay rate in [63] and the value of $|V_{cs}|$ from unitarity of the CKM matrix is from the PDG [5].

is compared to other extractions in Figure 7.13. It is obtained from the pseudoscalar to pseudoscalar $D \to K\ell\nu$ [83] by comparing the decay rate calculated on the lattice to experimental data. The D_s meson decay constant f_{D_s} can be used to find $|V_{cs}|$ by comparing it to the measurement decay rate $\Gamma(D_s \to \tau\nu)$ [63]. The value of $|V_{cs}|$ extracted by requiring that the CKM matrix is unitary is from the PDG [5].

The pseudoscalar to vector determination of $|V_{cs}|$ agrees well with unitarity and with the value extracted from pseudoscalar to pseudoscalar decays. The errors are not as good as for $D \to K\ell\nu$, but this is not surprising because the vector ϕ is more difficult to simulate in lattice QCD because there is more noise.

No error is included in the 3-point amplitudes from the ϕ decay constant being too high. The meson transition matrix element contains a weak $c \to s$ decay, so is less likely than the ϕ decay constant to be affected by coupling to $K\bar{K}$.

Chapter 8

Conclusions

Lattice QCD is a useful theoretical tool that can be used to make accurate calculations of QCD form factors relevant for flavour physics. In this thesis, I have discussed calculations of radiative and weak decays using lattice QCD.

My flavour physics calculations used improved staggered fermions. Concerns have been raised over the rooting procedure used to reduce the four tastes in gauge configurations generated with staggered sea quarks. This criticism has been addressed by studies of the low-lying eigenvalues of $\not{D}_{stag}$. I added to these studies, as described in Chapter 3, by looking at the corresponding eigenvectors. I checked that the eigenvectors corresponding to the four staggered tastes combine in such a way that the correlation functions with staggered quarks do not contain divergent contributions in the $m_q \to 0$ limit. Provided taste-singlet staggered meson operators are used, which is required for the disconnected piece of the correlator, I found that the behaviour was as expected.

In Chapters 5, 6 and 7, I used improved staggered quarks to calculate the nonperturbative QCD form factors for the radiative decays $J/\psi \to \eta_c\gamma$, $\eta_c \to 2\gamma$ and the weak semileptonic decay $D_s \to \phi\ell\nu$. The radiative decay calculations serve as checks of QCD and the semileptonic decay allowed me to extract a value for the CKM matrix element V_{cs}. My calculations of each of these decays were the first in lattice QCD with sea quarks included.

As part of my calculations, I developed several methods for nonperturbatively normalising staggered operators. These normalisations were used for the staggered vector and axial vector operators used for the electromagnetic and weak currents in the decays.

In my calculation of the $J/\psi \to \eta_c\gamma$ electromagnetic form factor, the errors are 4% on the form factor at the physical kinematics $V(q^2 = 0)$. My calculation of the decay rate using the vector and axial vector form factors in the semileptonic $D_s \to \phi\ell\nu$ decay was compared to experimental measurements to obtain a value for the CKM matrix element V_{cs} with errors of 5%. The result for V_{cs} is in agreement with other lattice QCD calculations of charm to strange decays using pseudoscalar to pseudoscalar meson decays, such as $D \to K\ell\nu$ [83].

The same techniques for the radiative decay can be applied to other vector to

pseudoscalar radiative meson transitions, such as $D_s^* \to D_s\gamma$. By combining with measurements of the branching fraction, the decay rate for $D_s^* \to D_s\gamma$ calculated using lattice QCD can be used to find the D_s^* width. The same method as for $\eta_c \to 2\gamma$ can be applied to $\pi^0 \to 2\gamma$ using light quarks instead of charm quarks [89]. This decay is well studied and can provide a good test of QCD. The HISQ action can be used to simulate heavier quarks than charm and extrapolate towards relativistic b quarks [74]. The methods I used for $D_s \to \phi\ell\nu$ can be extended to $B_{(s)} \to D^*_{(s)}\ell\nu$ to obtain lattice QCD results for the CKM matrix element V_{cb}.

Bibliography

[1] Abdus Salam. Weak and Electromagnetic Interactions. *Conf.Proc.*, C680519:367–377, 1968.

[2] Steven Weinberg. A Model of Leptons. *Phys.Rev.Lett.*, 19:1264–1266, 1967.

[3] Murray Gell-Mann. A Schematic Model of Baryons and Mesons. *Phys.Lett.*, 8:214–215, 1964.

[4] G. Zweig. An SU(3) model for strong interaction symmetry and its breaking. 1964.

[5] J Beringer et al. Review of particle physics. *Phys. Rev. D*, 86:010001, 2012.

[6] Nicola Cabibbo. Unitary Symmetry and Leptonic Decays. *Phys.Rev.Lett.*, 10:531–533, 1963.

[7] Makoto Kobayashi and Toshihide Maskawa. CP Violation in the Renormalizable Theory of Weak Interaction. *Prog.Theor.Phys.*, 49:652–657, 1973.

[8] D.J. Gross and Frank Wilczek. Ultraviolet Behavior of Nonabelian Gauge Theories. *Phys.Rev.Lett.*, 30:1343–1346, 1973.

[9] H. David Politzer. Reliable Perturbative Results for Strong Interactions? *Phys.Rev.Lett.*, 30:1346–1349, 1973.

[10] M. Kaku. *Quantum field theory: A Modern introduction*. Oxford University Press, 1993.

[11] Lewis H. Ryder. *Quantum Field Theory*. Cambridge University Press, 1985.

[12] F. Mandl and G. Shaw. *Quantum Field Theory*. Wiley, 1993.

[13] R. P. Feynman and A. R. Hibbs. *Quantum Mechanics and Path Integrals*. McGraw-Hill, 1965.

[14] Kenneth G. Wilson. Confinement of Quarks. *Phys.Rev.*, D10:2445–2459, 1974.

[15] Steven A. Gottlieb, W. Liu, D. Toussaint, R.L. Renken, and R.L. Sugar. Hybrid Molecular Dynamics Algorithms for the Numerical Simulation of Quantum Chromodynamics. *Phys.Rev.*, D35:2531–2542, 1987.

[16] M.A. Clark and A.D. Kennedy. Accelerating Staggered Fermion Dynamics with the Rational Hybrid Monte Carlo (RHMC) Algorithm. *Phys.Rev.*, D75:011502, 2007.

[17] M.A. Clark and A.D. Kennedy. Accelerating dynamical fermion computations using the rational hybrid Monte Carlo (RHMC) algorithm with multiple pseudofermion fields. *Phys.Rev.Lett.*, 98:051601, 2007.

[18] G.P. Lepage. Lattice QCD for novices. pages 49–90, 1998.

[19] I. Montvay and G. Munster. *Quantum fields on a Lattice*. Cambridge, 1994.

[20] K. Symanzik. Continuum Limit and Improved Action in Lattice Theories. 2. O(N) Nonlinear Sigma Model in Perturbation Theory. *Nucl.Phys.*, B226:205, 1983.

[21] R. Frezzotti and G.C. Rossi. Chirally improving Wilson fermions. 1. O(a) improvement. *JHEP*, 0408:007, 2004.

[22] Thomas DeGrand and Carleton DeTar. *Lattice methods for Quantum Chromodynamics*. World Scientific Publishing, 2006.

[23] Leonard Susskind. Lattice Fermions. *Phys.Rev.*, D16:3031–3039, 1977.

[24] J.F. Lagae and D.K. Sinclair. Improved staggered quark actions with reduced flavor symmetry violations for lattice QCD. *Phys.Rev.*, D59:014511, 1999.

[25] Kostas Orginos and Doug Toussaint. Testing improved actions for dynamical Kogut-Susskind quarks. *Phys.Rev.*, D59:014501, 1999.

[26] Peter Lepage. Perturbative improvement for lattice QCD: An Update. *Nucl.Phys.Proc.Suppl.*, 60A:267–278, 1998.

[27] G. Peter Lepage. Flavor symmetry restoration and Symanzik improvement for staggered quarks. *Phys.Rev.*, D59:074502, 1999.

[28] Satchidananda Naik. On-shell improved lattice action for QCD with Susskind fermions and asymptotic freedom scale. *Nucl.Phys.*, B316:238, 1989.

[29] E. Follana et al. Highly improved staggered quarks on the lattice, with applications to charm physics. *Phys.Rev.*, D75:054502, 2007.

[30] Heinz J. Rothe. *Lattice gauge theories: An Introduction*. World Scientific Lecture Notes on Physics, 1997.

[31] S. Aoki et al. Light hadron spectrum and quark masses from quenched lattice QCD. *Phys.Rev.*, D67:034503, 2003.

[32] A. Bazavov, C. Bernard, C. DeTar, J. Foley, W. Freeman, et al. Leptonic decay-constant ratio f_{K^+}/f_{pi^+} from lattice QCD with physical light quarks. 2013.

[33] Y. Namekawa et al. Charm quark system at the physical point of 2+1 flavor lattice QCD. *Phys.Rev.*, D84:074505, 2011.

[34] S. Durr, Z. Fodor, C. Hoelbling, S.D. Katz, S. Krieg, et al. Lattice QCD at the physical point: Simulation and analysis details. *JHEP*, 1108:148, 2011.

[35] A. Bazavov, D. Toussaint, C. Bernard, J. Laiho, C. DeTar, et al. Nonperturbative QCD simulations with 2+1 flavors of improved staggered quarks. *Rev.Mod.Phys.*, 82:1349–1417, 2010.

[36] A. Bazavov et al. Scaling studies of QCD with the dynamical HISQ action. *Phys.Rev.*, D82:074501, 2010.

[37] Michael Creutz. Why rooting fails. *PoS*, LAT2007:007, 2007.

[38] Stephen R. Sharpe. Rooted staggered fermions: Good, bad or ugly? *PoS*, LAT2006:022, 2006.

[39] Andreas S. Kronfeld. Lattice gauge theory with staggered fermions: How, where, and why (not). *PoS*, LAT2007:016, 2007.

[40] Gordon C. Donald, Christine T.H. Davies, Eduardo Follana, and Andreas S. Kronfeld. Staggered fermions, zero modes, and flavor-singlet mesons. *Phys.Rev.*, D84:054504, 2011.

[41] E. Follana, A. Hart, and C.T.H. Davies. The Index theorem and universality properties of the low-lying eigenvalues of improved staggered quarks. *Phys.Rev.Lett.*, 93:241601, 2004.

[42] E. Follana, A. Hart, C.T.H. Davies, and Q. Mason. The Low-lying Dirac spectrum of staggered quarks. *Phys.Rev.*, D72:054501, 2005.

[43] Stephan Durr, Christian Hoelbling, and Urs Wenger. Staggered eigenvalue mimicry. *Phys.Rev.*, D70:094502, 2004.

[44] Kit Yan Wong and R.M. Woloshyn. Systematics of staggered fermion spectral properties and topology. *Phys.Rev.*, D71:094508, 2005.

[45] M.F. Atiyah and I.M. Singer. The index of elliptic operators on compact manifolds. *Bull.Am.Math.Soc.*, 69:422–433, 1969.

[46] Jeroen C. Vink. Flavor symmetry breaking and zero mode shift for staggered fermions. *Phys.Lett.*, B210:211, 1988.

[47] Gerard 't Hooft. Computation of the Quantum Effects Due to a Four-Dimensional Pseudoparticle. *Phys.Rev.*, D14:3432–3450, 1976.

[48] Eric B. Gregory, Alan C. Irving, Christopher M. Richards, and Craig McNeile. A study of the eta and eta' mesons with improved staggered fermions. *Phys.Rev.*, D86:014504, 2012.

[49] Stephan Durr. Physics of η' with rooted staggered quarks. *Phys.Rev.*, D85:114503, 2012.

[50] G. Peter Lepage. On the Absence of O(a) Errors in Staggered-Quark Discretizations. 2011.

[51] G.P. Lepage, B. Clark, C.T.H. Davies, K. Hornbostel, P.B. Mackenzie, et al. Constrained curve fitting. *Nucl.Phys.Proc.Suppl.*, 106:12–20, 2002.

[52] Paulo F. Bedaque. Aharonov-Bohm effect and nucleon nucleon phase shifts on the lattice. *Phys.Lett.*, B593:82–88, 2004.

[53] D. Guadagnoli, F. Mescia, and S. Simula. Lattice study of semileptonic form-factors with twisted boundary conditions. *Phys.Rev.*, D73:114504, 2006.

[54] G.M. de Divitiis, R. Petronzio, and N. Tantalo. On the discretization of physical momenta in lattice QCD. *Phys.Lett.*, B595:408–413, 2004.

[55] G.C. Donald, C.T.H. Davies, R.J. Dowdall, E. Follana, K. Hornbostel, et al. Precision tests of the J/ψ from full lattice QCD: mass, leptonic width and radiative decay rate to η_c. *Phys.Rev.*, D86:094501, 2012.

[56] Jonna Koponen et al. The D to K and D to pi semileptonic decay form factors from Lattice QCD. *PoS*, LATTICE2011:286, 2011.

[57] Gordon Donald, Christine Davies, and Jonna Koponen. Axial vector form factors in $D_s \to \phi$ semileptonic decays from lattice QCD. *PoS*, LATTICE2011:278, 2011.

[58] C. Aubin and C. Bernard. Pion and kaon masses in staggered chiral perturbation theory. *Phys.Rev.*, D68:034014, 2003.

[59] A. Bazavov et al. B- and D-meson decay constants from three-flavor lattice QCD. *Phys.Rev.*, D85:114506, 2012.

[60] R.J. Dowdall et al. The Upsilon spectrum and the determination of the lattice spacing from lattice QCD including charm quarks in the sea. *Phys.Rev.*, D85:054509, 2012.

[61] Eric B. Gregory, Christine T.H. Davies, Iain D. Kendall, Jonna Koponen, Kit Wong, et al. Precise B, B_s and B_c meson spectroscopy from full lattice QCD. *Phys.Rev.*, D83:014506, 2011.

[62] R.E. Mitchell et al. J/psi and psi(2S) Radiative Decays to eta(c). *Phys.Rev.Lett.*, 102:011801, 2009.

[63] C.T.H. Davies, C. McNeile, E. Follana, G.P. Lepage, H. Na, et al. Update: Precision D_s decay constant from full lattice QCD using very fine lattices. *Phys.Rev.*, D82:114504, 2010.

[64] Damir Becirevic and Francesco Sanfilippo. Lattice QCD study of the radiative decays $J/\psi \to \eta_c\gamma$ and $h_c \to \eta_c\gamma$. *JHEP*, 1301:028, 2013.

[65] Jozef J. Dudek, Robert Edwards, and Christopher E. Thomas. Exotic and excited-state radiative transitions in charmonium from lattice QCD. *Phys.Rev.*, D79:094504, 2009.

[66] Ying Chen, De-Chuan Du, Bao-Zhong Guo, Ning Li, Chuan Liu, et al. Radiative transitions in charmonium from $N_f = 2$ twisted mass lattice QCD. *Phys.Rev.*, D84:034503, 2011.

[67] Jozef J. Dudek, Robert G. Edwards, and David G. Richards. Radiative transitions in charmonium from lattice QCD. *Phys.Rev.*, D73:074507, 2006.

[68] Jozef J. Dudek and Robert G. Edwards. Two Photon Decays of Charmonia from Lattice QCD. *Phys.Rev.Lett.*, 97:172001, 2006.

[69] Xiangdong Ji and Chulwoo Jung. Studying hadronic structure of the photon in lattice QCD. *Phys.Rev.Lett.*, 86:208, 2001.

[70] I. Allison et al. High-Precision Charm-Quark Mass from Current-Current Correlators in Lattice and Continuum QCD. *Phys.Rev.*, D78:054513, 2008.

[71] K.G. Chetyrkin, Johann H. Kuhn, and Christian Sturm. Four-loop moments of the heavy quark vacuum polarization function in perturbative QCD. *Eur.Phys.J.*, C48:107–110, 2006.

[72] R. Boughezal, M. Czakon, and T. Schutzmeier. Charm and bottom quark masses from perturbative QCD. *Phys.Rev.*, D74:074006, 2006.

[73] Y. Kiyo, A. Maier, P. Maierhofer, and P. Marquard. Reconstruction of heavy quark current correlators at O(alpha(s)**3). *Nucl.Phys.*, B823:269–287, 2009.

[74] C. McNeile, C.T.H. Davies, E. Follana, K. Hornbostel, and G.P. Lepage. High-Precision c and b Masses, and QCD Coupling from Current-Current Correlators in Lattice and Continuum QCD. *Phys.Rev.*, D82:034512, 2010.

[75] Bernard Aubert et al. Measurements of the absolute branching fractions of $B^{\pm} \to K^{\pm}$ X($c\bar{c}$). *Phys.Rev.Lett.*, 96:052002, 2006.

[76] Chen-Cheng Kuo et al. Measurement of $\gamma\gamma \to p\bar{p}$ production at Belle. *Phys.Lett.*, B621:41–55, 2005.

[77] Bernard Aubert et al. Study of the decay $D_s^+ \to K^+K^-e^+\nu_e$. *Phys.Rev.*, D78:051101, 2008.

[78] J.M. Link et al. Measurement of the ratio of the vector to pseudoscalar charm semileptonic decay rate $\Gamma(D^+ \to \bar{K}^{*0}\mu^+\nu)/\Gamma(D^+ \to \bar{K}^0\mu^+\nu)$. *Phys.Lett.*, B598:33–41, 2004.

[79] J. Gill. Semileptonic decay of a heavy light pseudoscalar to a light vector meson. *Nucl.Phys.Proc.Suppl.*, 106:391–393, 2002.

[80] Jeffrey D. Richman and Patricia R. Burchat. Leptonic and semileptonic decays of charm and bottom hadrons. *Rev.Mod.Phys.*, 67:893–976, 1995.

[81] E. Follana, C.T.H. Davies, G.P. Lepage, and J. Shigemitsu. High Precision determination of the pi, K, D and D(s) decay constants from lattice QCD. *Phys.Rev.Lett.*, 100:062002, 2008.

[82] B. Blossier et al. Pseudoscalar decay constants of kaon and D-mesons from $N_f = 2$ twisted mass Lattice QCD. *JHEP*, 0907:043, 2009.

[83] J. Koponen, C.T.H. Davies, and G. Donald. D to K and D to pi semileptonic form factors from Lattice QCD. 2012.

[84] M. Christian Arnesen, Benjamin Grinstein, Ira Z. Rothstein, and Iain W. Stewart. A Precision model independent determination of $|V(ub)|$ from $B \to \pi e\nu$. *Phys.Rev.Lett.*, 95:071802, 2005.

[85] Richard J. Hill. Update on semileptonic charm decays. *eConf*, C070805:22, 2007.

[86] Claude Bourrely, Irinel Caprini, and Laurent Lellouch. Model-independent description of $B \to \pi l\nu$ decays and a determination of $|V(ub)|$. *Phys.Rev.*, D79:013008, 2009.

[87] Heechang Na, Christine T.H. Davies, Eduardo Follana, G. Peter Lepage, and Junko Shigemitsu. The $D \to K, l\nu$ Semileptonic Decay Scalar Form Factor and $|V_{cs}|$ from Lattice QCD. *Phys.Rev.*, D82:114506, 2010.

[88] M. Wirbel, B. Stech, and Manfred Bauer. Exclusive Semileptonic Decays of Heavy Mesons. *Z.Phys.*, C29:637, 1985.

[89] Xu Feng, Sinya Aoki, Hidenori Fukaya, Shoji Hashimoto, Takashi Kaneko, et al. Two-photon decay of the neutral pion in lattice QCD. *Phys.Rev.Lett.*, 109:182001, 2012.